Technische Universität München
TUM School of Natural Sciences

# Surface Modification of 0D and 2D Silicon Nanomaterials: Towards Anisotropic Materials and Application in Optoelectronics

Elisabeth Groß

Vollständiger Abdruck der von der TUM School of Natural Sciences der Technischen Universität München zur Erlangung einer

Doktorin der Naturwissenschaften (Dr. rer. nat.)

genehmigten Dissertation.

Vorsitz: Prof. Dr. Klaus Köhler

Prüfer*innen der Dissertation:

1. Prof. Dr. Dr. h.c. Bernhard Rieger
2. Prof. Dr. Jonathan G.C. Veinot

Die Dissertation wurde am 12.04.2023 bei der Technischen Universität München eingereicht und durch die TUM School of Natural Sciences am 29.04.2023 angenommen.

*“A scientist in his laboratory is not a mere technician: he is also a child confronting natural phenomena that impress him as though they were fairy tales.”*

Marie Curie

# Danksagung

Zuallererst möchte ich mich bei meinem Doktorvater *Prof. Dr. Dr. h.c. Bernhard Rieger* bedanken für die herzliche Aufnahme an seinem Lehrstuhl und die Möglichkeit meine Doktorarbeit anzufertigen. Es war großartig, am Wacker-Lehrstuhl für makromolekulare Chemie mit so guter Ausstattung zu arbeiten und im Rahmen von ATUMS neue Materialien zu erforschen. Vielen Dank für die wertvollen Diskussionen.

Also, I want to thank *Prof. Dr. Jonathan G.C. Veinot* for welcoming me into his group, sharing his expertise in the field of nano-scaled silicon, and the funny gathering events beyond work.

Vielen Dank dem Leitungs-Team des Wacker Lehrstuhls: *Dr. Carsten Troll* für seine unermüdliche Hilfe beim Reparieren von Geräten, *Dr. Sergei Vagin* für die umfassende Organisation rund um ATUMS, *Katia Rodewald* für die REM-Messungen und Bestellungen sowie *Frau Bauer* für die Hilfe bei der Bürokratie.

Mein Dank gilt auch meinen Masterarbeitsbetreuern *Dr. Marc Kloberg* und *Dr. Josef Mock,* die mir während der Promotion mit Rat und Tat zur Seite standen und nicht unerheblich zum Gelingen dieser Arbeit beitrugen.

Immer in Erinnerung wird mir die angenehme Arbeitsatmosphäre am Lehrstuhl bleiben. Besonders möchte ich meinen Kollegen *Jonas Breitsameter, Andreas Saurwein, Kerstin Halama, Paula Großmann* und *Moritz Kränzlein* danken für die nie langweiligen, meist witzigen Stunden im Labor und den Ausgleich dazu beim Laufen, Schwimmen oder Bouldern.

Ein besonderer Dank gilt meiner Laborpartnerin *Amelie Mühlbach* für die wertvollen Diskussionen, die angenehme Zusammenarbeit und die wundervolle Zeit in Kanada.

Die Hüttenwochenenden, Grillabende oder Lehrstuhlausflüge haben eine Abwechslung zur Laborarbeit geschaffen. Daher danke ich allen ehemaligen und derzeitigen Kollegen der Makro Süd, der Makro Nord und dem Si-Institut.

*Annabelle Degg, Dr. Christoph Wallach und Sabrina Artmeier* möchte ich die kurzweilige und aufregende Zeit in Kanada danken. Neben der interessanten Laborzeit werden mir die zahlreichen Unternehmungen in Erinnerung bleiben.

I want to thank the students of Prof. Veinot‘s group for welcoming me. Special thanks go to *I Teng (Emily) Cheong* for the productive cooperation and the exciting time on gatherings and excursions together in Germany and Canada.

Danken möchte ich auch meinen Studenten *Sipeng Liu*, *Victoria Brandt* und *Aylin Yilmaz*, deren Arbeit zum Gelingen meiner Doktorarbeit beigetragen hat.

Außerdem danke ich allen, die mich privat und an der TUM im letzten Jahrzehnt begleitet haben. Meiner Mama, meiner Schwester und meinem Vater möchte ich besonders für ihre fortwährende Unterstützung während meiner Promotion, meines Studiums und den nicht unbedeutenderen Jahren davor danken.

Vielen Dank an Max, der mir immer an meiner Seite stand und den Rücken gestärkt hat. Ohne dich wäre die Arbeit nicht in dieser Form möglich gewesen.

# Table of Contents

## List of publications

1. M. J. Kloberg, H. Yu, E. Groß, F. Eckmann, T. M. F. Restle, T. F. Fässler, J. G. C. Veinot, B. Rieger, *Adv. Mater.* **2021**, 2100288.
2. J. Mock†, E. Groß†, M. J. Kloberg, B. Rieger, M. Becherer, *Adv. Photonics Res.* **2021**, 2100083. † these authors contributed equally
3. J. Mock, M. Kallergi, E. Groß, M. Golibrzuch, B. Rieger, M. Becherer, *IEEE Photonics J.* **2022**, *14*, DOI 10.1109/JPHOT.2022.3184401.
4. T. Cheong, J. Mock, M. Kallergi, E. Groß, A. Meldrum, B. Rieger, M. Becherer, J. G. C. Veinot, I. T. Cheong, J. G. C. Veinot, *Adv. Opt. Mater.* **2022**, 2201834.

## Abstract

Silicon is used in microelectronic applications due to its semiconducting character. By shrinking bulk silicon to the nanoscale, luminescent nanomaterials appear. This thesis covers research on surface functionalization toward the synthesis of anisotropic materials and the application of silicon nanocrystals and silicon nanosheets.

New surface functionalization methods, a crucial research field, are investigated because nanomaterials possess a high surface-to-volume ratio. Surface functionalization protects the silicon nanomaterials from oxidation and enhances their solubility, thus, their processability. Organic surface groups tune the optical properties of silicon nanomaterials besides size-dependent quantum confinement. However, facile and precise surface functionalization methods for silicon nanomaterials are required to adjust the luminescence color and solubility, which are necessary to improve the application in optoelectronic devices or bioimaging.

Herein, new concepts of surface functionalization are investigated to insert unique groups. Research on Lewis acid-induced dehydrogenative coupling with silanes aims to enlarge the semiconducting system by interconnecting silicon nanosheets at the edges. However, the method failed due to insufficient polarization of Si-H bonds. Another technique utilizes trityl salts as initiators for capping nucleophiles to silicon nanocrystals. Interesting observations occur by activation with trityl tetrafluoroborate or trityl hexafluorophosphate in the absence of nucleophiles. The silicon nanocrystal surface is fluorinated and the typical luminescence diminishes. Furthermore, alkyl lithium reagents with different chain lengths and sulfides are compared as two different surface functionalizations. Silicon nanocrystals capped with the respective molecules are applied as a luminescent layer in light-emitting diodes. Defects are obtained when sulfide-capped silicon nanocrystals are applied as films, causing a low performance in optoelectronic devices. Using organolithium reagents for surface groups instead, bright and efficient diodes are built with alkyl chain lengths of six or eight carbon atoms.

Organolithium reagents are also used to synthesize surface-anisotropic silicon nanocrystals. At first, silicon nanocrystals are liberated from a silicon nanosheet mask. Anisotropic functionalization subsequently yields so-called Janus silicon nanocrystals. The concept widens the scope of substrates by including conjugated groups and offers size-independent synthesis, thus leading to a redshifted emission color. Another anisotropic material involves silicon nanosheets decorated only on one side with palladium nanoparticles. This design enables fast and directed moving nanomotors. Thereby, surrounding hydrogen peroxide is used as fuel and decomposes.

These nanomaterials contribute as a non-toxic and abundant alternative to heavy metal quantum dots to the potential application in biomedicine and optoelectronics.

## Kurzzusammenfassung

Silicium wird aufgrund seines halbleitenden Charakters in mikroelektronischen Anwendungen eingesetzt. Durch die Verkleinerung von Silicium auf Nanoebene entstehen lumineszierende Nanomaterialien. Diese Arbeit befasst sich mit der Forschung zur Oberflächenfunktionalisierung für die Synthese von anisotropen Materialien und die Anwendung von Silicium-Nanokristallen und Silicium-Nanoblättern.

Da Nanomaterialien ein hohes Verhältnis von Oberfläche zu Volumen aufweisen, werden neue Methoden der Oberflächenfunktionalisierung untersucht, die ein wichtiges Forschungsgebiet darstellen. Die Oberflächenfunktionalisierung schützt die Silicium-Nanomaterialien vor Oxidation und verbessert ihre Löslichkeit und damit ihre Verarbeitbarkeit. Organische Oberflächengruppen beeinflussen neben dem größenabhängigen Potentialtopf auch die optischen Eigenschaften von Silicium-Nanomaterialien. Es sind jedoch einfache und präzise Oberflächenfunktionalisierungsmethoden für Silicium-Nanomaterialien erforderlich, um die Lumineszenzfarbe und die Löslichkeit einzustellen, was für eine bessere Anwendung in optoelektronischen Geräten oder in der biologischen Bildgebung notwendig ist.

In dieser Arbeit werden neue Konzepte der Oberflächenfunktionalisierung untersucht, um einzigartige Gruppen einzufügen. Forschungen zur Lewis-Säure-induzierten, dehydrierenden Kopplung mit Silanen zielen darauf ab, das halbleitende System zu vergrößern, indem Silicium-Nanoblätter an den Kanten miteinander verbunden werden. Die Methode scheiterte jedoch an der unzureichenden Polarisierung der Si-H-Bindungen. Eine andere Technik nutzt Tritylsalze als Initiatoren, um Nukleophile an Silicium-Nanokristalle anzubringen. Interessante Beobachtungen ergeben sich bei der Aktivierung mit Trityltetrafluoroborat oder Tritylhexafluorophosphat in Abwesenheit von Nukleophilen. Die Oberfläche der Silicium-Nanokristalle wird fluoriert und die typische Lumineszenz verschwindet. Außerdem werden Alkyllithiumreagenzien mit unterschiedlichen Kettenlängen und Sulfide als zwei verschiedene Oberflächenfunktionalisierungen verglichen. Silicium-Nanokristalle, die mit den jeweiligen Molekülen bedeckt sind, werden als aktive Schicht in Leuchtdioden eingesetzt. Werden mit Sulfiden funcktionalisierte Silicium-Nanokristalle als Filme aufgebracht, kommt es zu Defekten, die eine geringere Leistung in optoelektronischen Geräten verursachen. Werden stattdessen Organolithium-Reagenzien für Oberflächengruppen verwendet, lassen sich helle und effiziente Dioden mit Alkylkettenlängen von sechs oder acht Kohlenstoffatomen herstellen.

Organolithium-Reagenzien werden auch zur Synthese von oberflächenanisotropen Silicium-Nanokristallen verwendet. Zunächst werden Silicium-Nanokristalle aus einer Maske aus Silicium-Nanoblättern getrennt. Die anisotrope Funktionalisierung führt dann zu sogenannten Janus-Silicium-Nanokristallen. Das Konzept erweitert die Bandbreite der Substrate durch die Einbeziehung konjugierter Gruppen und bietet eine größenunabhängige Synthese, die zu einer rotverschobenen Emissionsfarbe führt. Ein weiteres anisotropes

Material sind Silicium-Nanoblätter, die nur auf einer Seite mit Palladium-Nanopartikeln besetzt sind. Dieses Design ermöglicht sich schnell und gezielt bewegende Nanomotoren. Dabei wird das umgebende Wasserstoffperoxid als Brennstoff verwendet und zersetzt sich.

Diese Nanomaterialien tragen als ungiftige und vorhandene Alternative zu Schwermetall-Quantenpunkten zur möglichen Anwendung in der Biomedizin und Optoelektronik bei.

# List of Acronyms

## Chemicals and Materials

| | |
|---|---|
| AIBN | azobisisobutyronitrile |
| BIP | bis(4-tert-butyl-phenyl)iodonium hexafluorophosphate |
| BuLi | n-butyllithium |
| DBPO | dibenzoyl peroxide |
| DCB | 1,2-dichlorobenzene |
| DCM | dichloromethane |
| 4-DDB | 4-decyldiazobenzene tetrafluoroborate |
| DI | deionized |
| DodecLi | dodecyl lithium |
| DodecSH | dodecanethiol |
| $Et_2O$ | diethyl ether |
| HexLi | hexyl lithium |
| HF | hydrofluoric acid |
| HMDS | hexamethyldisilazane |
| HSQ | hydrogen silsesquioxane |
| LA | Lewis acid |
| MEH-PPV | poly[2-methoxy-5(2′-ethylhexyl-oxy)1,4-phenylene-vinylene] |
| MeLi | methyl lithium |
| OctLi | octyl lithium |
| PEDOT:PSS | poly(3,4-ethylene dioxythiophene)-poly(styrenesulfonate) |
| PhAcLi | lithium phenylacetylide |
| PolyTPD | poly[N,N′-bis(4-butylphenyl)-N,N′-bisphenylbenzidine] |
| SiNC | silicon nanocrystal |
| SiNS | silicon nanosheet |
| SiQD | silicon quantum dot |
| SRO | silicon-rich-oxides |

| | |
|---|---|
| t-BuLi | tert-butyllithium |
| tBuMA | tert-butyl methacrylate |
| TMVS | trimethoxy(vinyl) silane |
| TrBCF | trityl tetrakis(pentaflourophenyl)borate |
| TrBF4 | trityl tetrafluoroborate |
| TrPF6 | trityl hexafluorophosphate |
| VTMS | (vinyl)trimethyl silane |

## Analytical Techniques

| | |
|---|---|
| ATR | attenuated total reflectance |
| CP/MAS | cross-polarization/magic angle spinning |
| DLS | dynamic light scattering |
| EDS | energy-dispersive X-ray spectroscopy |
| FT-IR | Fourier transform infrared spectrometer |
| hpdec | high power decoupling |
| INEPT | insensitive nuclei enhanced by polarization transfer |
| JLV | current-luminance-voltage-characterization |
| MRI | magnetic resonance imaging |
| NMR | nuclear magnetic resonance spectroscopy |
| SEM | scanning electron microscopy |
| SMU | source measuring unit |
| TEM | transmission electron microscopy |
| TGA | thermogravimetric analysis |
| UV/Vis | ultraviolet/visible |

## Units

| | | |
|---|---|---|
| $\vartheta$ | temperature | °C |
| $\lambda$ | wavelength | nm |

| | | |
|---|---|---|
| δ | chemical shift | ppm |
| v | wave number | $cm^{-1}$ |
| ω | rotational speed | rpm |
| c | concentration | mol/L |
| $E_e$ | irradiance | $W/m^2$ |
| f | frequency | Hz |
| J | current | A |
| M | molar mass | g/mol |
| m | mass | g |
| r | deposition rate | Å/s |
| SC | surface coverage | % |
| t | time | h, min, s |
| T | temperature | K |
| U | voltage | V |
| V | volume | L |
| x | molar amount | mol |

**Other**

| | |
|---|---|
| CB | conduction band |
| CV | capacitance-voltage |
| DHC | dehydrogenative coupling |
| DOS | density of states |
| EBL | electron blocking layer |
| e.g. | exempli gratia (lat. for example) |
| EGFET | electrolyte-gated field-effect transistor |
| EL | electroluminescence |

| | |
|---|---|
| eq. | equivalents |
| et al. | *et alii* (lat. and others) |
| ETL | electron transport layer |
| FWHM | full width at half maximum |
| HBL | hole blocking layer |
| Het | heteroatom |
| HTL | hole transport layer |
| HS | hydrosilylation |
| i.a. | *inter alia* (lat. among other things) |
| i.e. | *id est* (lat. that is) |
| IR | infrared |
| LCST | lower critical solution temperature |
| LED | light-emitting diode |
| OLED | organic light-emitting devices |
| NLO | non-linear optics |
| PL | photoluminescence |
| Ref | reference |
| RoHS | restriction of certain hazardous substances |
| SCLC | space-charge limited current |
| QD-LED | quantum dot light-emitting diode |
| QY | quantum yield |
| QD | quantum dot |
| VB | valence band |

# 1. Introduction

Nanotechnology describes the manipulation of matter at the atomic and molecular scale with dimensions from 1 to 100 nm. It roots in the work of scientists and researchers from various fields, including physics, chemistry, and biology. The term "nanotechnology" was first coined by physicist and Nobel laureate Richard Feynman in a talk he gave in 1959. He discussed the possibility of manipulating and controlling individual atoms and molecules.[1] A significant milestone in the field of nanotechnology was the invention of the scanning tunneling microscope in 1981, which allowed scientists to image individual atoms. Researchers can also move atoms and molecules across the surface by applying a voltage to the tip.[2] As the field continues to grow and evolve, the potential for nanotechnology to revolutionize many aspects of our lives is increasingly becoming a reality. The market volume of nanotechnologies amounted USD 5.2 billion in 2021 and is proposed to increase to USD 60.86 billion by 2029.[3] Nanoparticles, which are necessary for nanotechnology, were found in 1856. Faraday discovered ruby gold, including the optical properties known as the Faraday-Tyndall effect.[4,5] 150 years later, colloidal gold nanoparticles are applied, i.a., in rapid tests for COVID antigens.[6]

The quantum confinement effect, discovered in 1963 independently by Alferov and Kroemer, is the most famous property of nanomaterials.[7,8] By shrinking semiconducting nanoparticles below the Bohr radius, they become luminescent so-called quantum dots (QD). In a QD, excitons (electron-hole pairs) are confined in all three spatial dimensions. Quantum dots are applied to optoelectronics, e.g., in developing new light-emitting diodes (LEDs). Luminescent quantum dots are utilized as an active layer in LEDs constructed for displays. By varying the QD size, the emission color of the LED is varied. In contrast to conventional OLEDs, QD-LED displays exhibit color purity, solution processability, and long-term stability.[9]

Nanomaterials occur in countless structures and shapes, e.g., such as sheets, particles, wires, tubes, stars, or spheres.

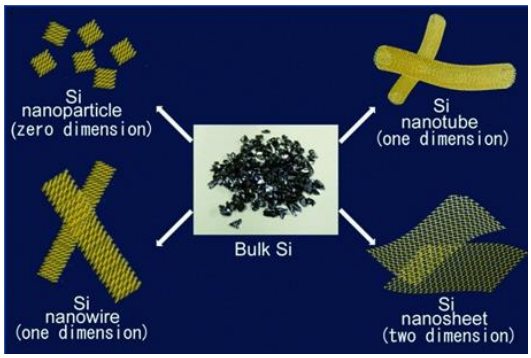


Figure 1: Schemes of different shapes and dimensions of silicon nanomaterials. Reprinted with permission from Ref.[10].

Nanomaterials are classified by the number of dimensions that exceed the nanometer regime (> 100 nm) for a facilitated description. For instance, 0D describes nano-scaled spherical or cubic particles, 1D materials are nanowires with fiber diameter in the nanometer regime, and 2D materials are flat or buckled structured sheets with a thickness of nm magnitude. Some examples for silicon are shown in Figure 1.

Silicon is indispensable for the electronic and information industry because of its semiconducting properties. A region in California, the center of innovating information technology, from mid of the last century, is named Silicon Valley after the abundant element in the earth's crust. Silicon will still play an essential role in future technologies; it is unknown in which structure and function.

# 2. Theoretical Background - State of the Art

## 2.1. Silicon Nanocrystals

### 2.1.1. Synthesis Routes

The predecessor of freestanding SiNCs, porous silicon, was discovered by electrochemical etching of silicon wafers.[11] Since then, many synthesis routes for SiNCs have been developed and categorized into either bottom-up or top-down approaches. Desired conditions for SiNC synthesis are a narrow size distribution, high outputs, and reproducibility. For fundamental research on this material, a low-cost setup and SiNCs with tuneable optical emissions are ideal.

Top-down synthesis is based on destroying the bulk precursor that already contains the nanomaterial structure; for example, exfoliation from carbon layers of graphite can result in graphene.[12] The bulk precursors for SiNCs are silicon wafers, silicon powder, and oxidized silicon matrix. Heintz *et al*. achieved blue-emitting particles (d < 4 nm) by ball-milling silicon wafers.[13] A significant advantage of this method is the simultaneous surface functionalization with a low-cost setup. However, the free-standing nanoparticles from this synthesis had broad size distribution and low yield.

Besides mechanical grinding, Si wafers can be etched under vacuum with a laser beam. The helium carrier gas cools the produced silicon plasma and nanoclusters are size-selected by time-of-flight.[14] When the synthesis is conducted in a liquid phase instead under vacuum, SiNCs are directly obtained in a colloidal solution.[15] The laser ablation method yet had poor size selection and low yields. Besides getting free-standing nanoparticles, ion implantation of luminescent SiNCs in silicon oxides was explored for LEDs. In this method, silicon ions are bombarded on a host material, e.g., $SiO_2$.[16,17] In contrast to the previous methods, the significant advantage is instant protection from oxidation by the matrix. On the other side, the setup is very costly.

In conclusion, top-down approaches offer a facile opportunity to discover new materials through different bulk materials. The purity and quality of the resulting nanomaterial depend on the grade of the bulk material, making top-down approaches quite costly. The lack of shape and size control also presents difficulties in tuning and optimizing reproducible batches of SiNCs. Bottom-up approaches can avoid these drawbacks due to a different synthesis concept and offer the potential to upscaled SiNC production.

From a molecular view, bottom-up approaches obtain silicon nanomaterials by assembling molecular silicon precursors. These methods are subdivided according to the physical state into gaseous phase, solution, and solid-state synthesis. At gas-phase production of SiNCs, silane is decomposed by an energy source (e.g., laser, heat, or plasma). Brus *et al.* synthesized SiNCs with a 1-2 nm diameter and a relative quantum yield (QY) of 5% by

pyrolysis of disilane in a high-temperature aerosol reaction.[18] Li *et al.* utilized for the same principle a $CO_2$ laser which achieved a SiNC throughput of 200 mg/h. After etching with $HF/HNO_3$, the SiNCs were luminescent with a QY between 2-15%.[19] An alternative aerosol approach uses argon carrier gas with (chloro)-silane passing through a non-thermal plasma unit. Under the energy impact of hot electrons (plasma), the silicon precursor decomposes and then forms nanocrystals. This method generates a negatively charged SiNC surface, which prevents particle agglomeration.[20] Highly reactive species at low temperatures result from collisions of the molecular precursor with electron plasma and avoid growing SiNCs to large particles due to the lack of chemical equilibrium. Kortshagen *et al.* obtained 2-8 nm SiNCs with a PL maximum of around 700-900 nm.[21] Size control was conducted by adjusting the argon flow rate to reach polydispersities of 12-17%. The all-aerosol reactor achieved the fastest SiNC synthesis and functionalization combination within 100 ms.[22] However, gas-phase synthesis requires expensive and precise lab equipment. Special safety technology is also necessary to treat harmful (chloro)-silanes at high temperatures.

Solution-based synthesis routes of SiNCs have the reduction of silane precursors in common. Nowadays, the SiNCs are synthesized in an average lab with bench-top chemical equipment, unlike early strategies of thermal reaction of $SiCl_4$ at 385 °C at high pressures in a bomb reactor.[23] SiNC synthesis and surface functionalization are performed in the solution phase in one-pot reaction. These established methods require a silicon (halide) precursor, a reducing agent, and a capping agent (Scheme 1).[24]

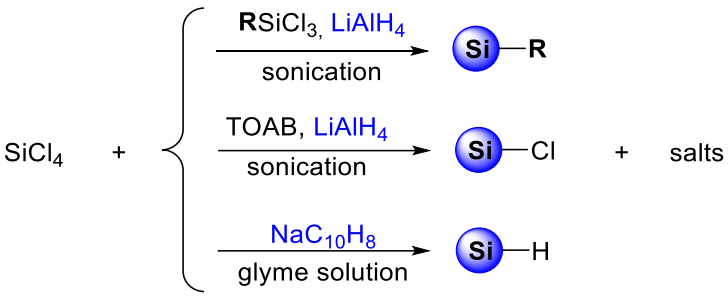


Scheme 1: Examples of solution-based SiNC synthesis routes. Adapted from Ref.[24] with permission from the Royal Society of Chemistry.

Wilcoxon *et al*. yielded hydride-terminated SiNCs from inverse micelles containing $SiCl_4$ with tetraoctylammonium bromide (TOAB) and $LiAlH_4$ as reducing and surfactant agents at room temperature. The downside of this method is the hazardous byproduct $SiH_4$. Size control was conducted by tuning the starting material ratio to achieve polydispersities from 15-25% and narrowed further by HPLC separation.[25] Reduction with sodium naphthalide was undertaken as an alternative to hydride-based reducing agents.[26] Also, halogen-capped SiNCs are obtained from reaction of metal silicide Zintl salts. Possible reducing agents are $NH_4Br$, $SiCl_4$, or bromine, as depicted in Scheme 2.

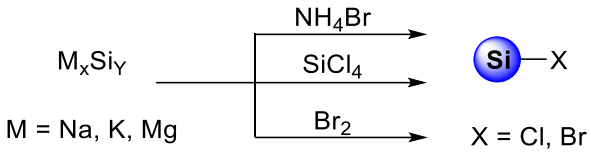


Scheme 2: Synthesis with metal silicide Zintl salts. Adapted with permission from Ref.[27].

In contrast to using $SiCl_4$ as a SiNC precursor, silicide Zintl phases are utilized as silicon sources. The first synthesis was conducted with KSi yielding high amounts of amorphous byproduct.[28] Instantaneous alkoxy capping was performed later with NaSi.[29] The formation mechanism seems complex and remains unknown. Improvement was achieved by the Kauzlarich group that used less reactive and more covalent $Mg_2Si$ with long-term stable blue PL.[30] In conclusion, solution-based synthesis of SiNCs lacks tuning the PL emission. Amine-based contaminations lead to size-independent blue luminescent SiNCs exclusively. Additionally, the separation of the surfactants is elaborate.

Solid-state synthesis approaches are based on the thermal treatment of silicon-rich oxides (SRO). The most important advantages are reproducible narrow size distribution, requiring only modest lab equipment, and avoiding harmful substances. The observed SiNC precursor is benchtop storable, and SiNCs are liberated from the matrix on demand by etching. After surface functionalization of SiNCs, the material exhibits the highest QY and increased brightness combined with colloidal stability. The first solid-state synthesis was conducted by Hayashi *et al*., who produced SiNCs embedded in $SiO_2$ from thin-film $SiO_x$ in 1993.[31] The SiNCs were liberated by etching with $HF/HNO_3$ and exhibited PL. The narrowest polydispersity of 6% was observed from 200 nm SiNCs within the SRO precursor, which is kept between the melting temperature of bulk silicon (1410 °C) and silica (~1700°C). The obtained particles exhibit no PL but Mie scattering.[32]

Hessel *et al.* utilized hydrogen silsesquioxane (HSQ), an SRO sol-gel polymer, for SiNC synthesis.[33] Upon thermal treatment of the HSQ, disproportionation is observed, resulting in SiNCs embedded in a $SiO_2$ matrix (Scheme 3).

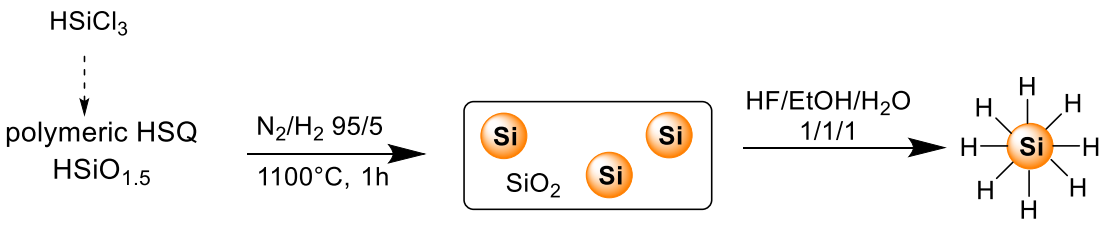


Scheme 3: Synthesis of SiNCs from HSQ with liberation with HF etching.

The detailed mechanism remains unknown. However, it is assumed that $SiH_4$ formation takes place at 250-350 °C, which also rearranges the HSQ network. At 450 °C, the dissociation of Si-H bonds leads to elemental Si moieties in the matrix.[33,34] Luminescent particles sizing from 1.1-90 nm were achieved. While varying the ceiling temperature was sufficient for preparing

SiNCs from 3-90 nm (Figure 2), smaller particles were observed at longer etching times (~2.5 h) and separated by size-selective precipitation.[35,36] Less crosslinked HSQ was obtained by the addition of methanol to trichlorosilane. It yielded larger SiNCs with red to near-IR PL.[37] Detailed advice on the SiNC synthesis from HSQ to colloidal stable, luminescent particles was described by Li *et al*.[38]

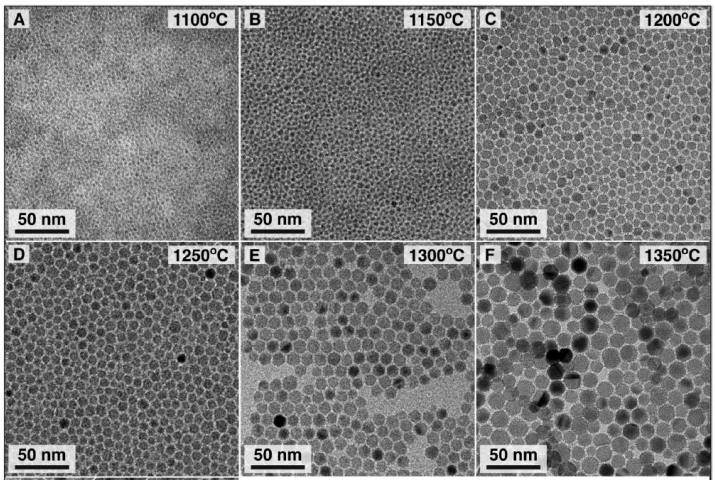


Figure 2: Transmission electron microscopy (TEM) images of SiNCs obtained from HSQ at different ceiling temperatures. Reprinted with permission from Ref.[36]

After forming SiNCs in the oxide matrix, liberating hydride-terminated SiNCs through HF-etching is necessary. This critical step cleaves the silanol and Si-O-Si bridges of the matrix by replacing Si-F bonds, as shown in Scheme 4. Due to the ionic nature of the Si-F bond, the backbone polarizes and enhances the subsequent HF insertion until $SiF_4$ is released (Scheme 4).[39]

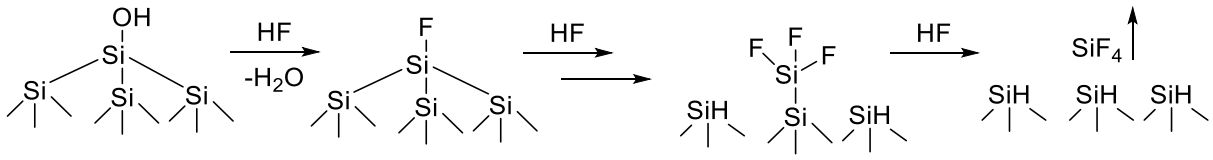


Scheme 4: Etching mechanism of silicon surfaces with HF. Adapted with permission from Ref.[39].

Computational studies investigated the mechanism and suggested how to enhance the etching rate. Steinert *et al.* revealed that acidic conditions improve the protonation of oxygen atoms.[40] In the presence of water, a concerted attack of HF and $H_2O$ increases the etching rate.[41] The addition of ethanol reduces surface tension and enhances the dispersibility of the SiNC/$SiO_2$ composite.[38] Comparing the bond strength of Si-F (576 kJ/mol) and Si-H (293 kJ/mol), fluorinated SiNC surfaces are expected to be more stable.[42] But the etching process seems to be ruled by a kinetic regime rather than thermodynamically. This circumstance is discussed in chapter 4.2.

Generally, bottom-up approaches, specifically solid-sate synthesis with HSQ, show many advantages, like control over size and shape, thus band gap dependent PL maximum.

Furthermore, the method requires modest lab equipment, so SiNCs from HSQ are utilized in this thesis. The obtained free-standing hydride-terminated SiNCs enable access to facile surface chemistry for different applications. Apart from the straightforward hydrosilylation (HS) passivation, several functionalization methods are introduced in the following chapter.

### 2.1.2. Surface Functionalization

SiNCs, like all silicon nanomaterials, are prone to oxidation because of the oxophilicity of silicon. Oxidation often leads to the loss of desired properties of SiNCs, e.g., luminescence and dispersibility in solvents. Surface passivation hence is crucial to ensure the protection of the SiNCs and enable dispersibility in different solvents. Many functionalization methods for SiNCs are inspired by capping porous silicon or Si thin-films.[43] This chapter divides the variety of functionalization routes into the SiNC surface termination. SiNCs are obtained hydride- or halogen-terminated directly after synthesis and before surface functionalization.

#### 2.1.2.1. Functionalization of Hydride-terminated SiNCs

The most common functionalization method for hydride-terminated SiNCs is hydrosilylation. To hydride-terminated SiNCs, alkene and alkyne-terminated substrates are added. Mechanistically, the Si-H bond is substituted by the Si-C surface bond. The steric abundance of the surface group hinders oxygen from reaching the silicon surface and ensures protection against decomposition. The following paragraphs introduce several initiation mechanisms of HS and consider their advantages and drawbacks.

A facile route is the thermally initiated hydrosilylation, where the SiNCs and the substrate are heated to temperatures ranging from 150 to 180 °C. Mechanistically, Si-H bonds are cleaved homolytically to yield Si surface radicals that can then react with the unsaturated C-C bonds of the ligand precursors.[44] The advantage of the reaction is that only unreacted substrate and solvent need to be separated at workup. A drawback is that oligomerization of the substrates takes place so that precise monolayers on the surface can not be formed.[45] Furthermore, the scope of suitable substrates is limited because decomposition at high temperatures is possible. A high boiling solvent is also required if the reaction is not performed under neat conditions. Due to the need for excess substrate in the thermal HS, expensive substrates are unsuitable. Nevertheless, a mixed surface of low-cost and expensive substrates can overcome the price issue. The Ceroni group, for example, functionalized SiNCs with dodecene and a porphyrin derivate and applied the material as light-harvesting antennae. The excitation of the porphyrin dyes led to sensitized emission of the SiNCs at 905 nm with a lifetime of 130 µs.[46]

Exciton-mediated HS enables surface capping under irradiation with UV light.[47] However, this method only applies to SiNCs smaller than the exciton's Bohr radius and leads to unwanted oxidation due to low surface coverage. Additionally, the reaction is incompatible with substrates containing amine and alcohol moieties since these compete against the

functionalization of the unsaturated functional group. Nevertheless, this UV-induced HS was used in the classical synthesis of Janus SiNCs from a SiNCs/SiNSs hybrid material. Irradiation of UV light liberated the SiNCs from the SiNSs masking material through the decomposition of SiNSs and enabled subsequent surface capping of SiNCs *via* HS in one reaction step.[48]

A variety of radial initiators is utilized for the HS of SiNCs. Besides classical initiators for radical polymerization like azobisisobutyronitrile (AIBN) and dibenzoyl peroxide (DBPO), other substances like diazonium salts and iodonium salts are investigated.[49–51] AIBN and DBPO require reaction temperatures of 60 or 85 °C, respectively, but the latter two initiator salts work at room temperature.[51,52] All radical initiators enable an enlarged scope of substrates at short reaction times (~3 h). An instantaneous HS was observed at initiation with $XeF_2$.[53] The fluorine radicals led to fluorination of the SiNC surface and transferred radicals to the Si-surface. HS of dodecene took place within five minutes. However, the SiNC particle size was reduced from 3 to 2.3 nm, thus leading to yellow PL originating from band gap transitions. Longer reaction times with $XeF_2$ result in a loss of SiNCs due to a reactivity of the initiator similar to HF etching. Therefore, functionalization is more reasonable for larger (>5 nm) SiNCs. Another HS initiator, $PCl_5$, works analogous to $XeF_2$ but with chlorine radicals.[54] The initiation of $PCl_5$ and $XeF_2$ reaches SiNCs with QY up to 70%, attributed to removal of dark defect states.

In contrast to solution-phase functionalization approaches, HS can also be conducted by plasma assistance.[55,56] The all-aerosol reactor of the Kortshagen group synthesized and functionalized the SiNCs with alkenes within 100 ms (Figure 3).[22] The SiNCs were not exposed to air the whole time at such plasma reactors. This method can fix low-boiling short alkynes like acetylene on the SiNC surface.[57]

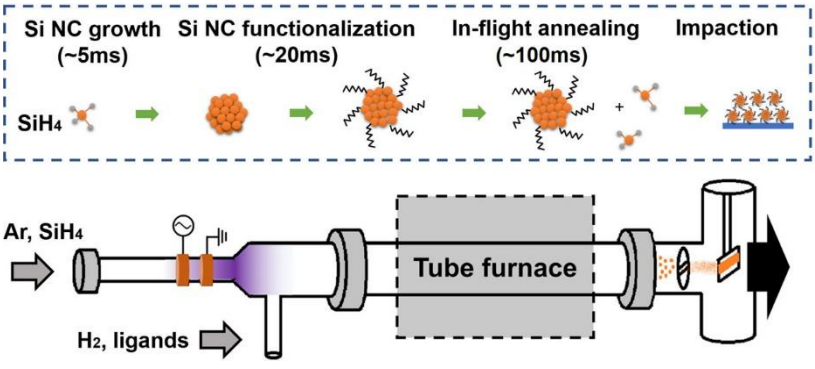


Figure 3: An all-aerosol reactor for SiNC synthesis and HS. Reprinted with permission from Ref.[22]

Catalyst-based HS of alkenes and alkynes were also explored using platinum ($H_2PtCl_6$) and Lewis acids.[58] Platinum is costly, and metal residues affect the optical properties, e.g., quenching of PL. This drawback was overcome first by Buriak *et al.* They utilized non-metallic Lewis acids as HS initiators on silicon nanomaterials.[59] The Veinot group discovered $BH_3THF$ as a versatile HS initiator at room temperature.[60] They proposed two different reaction mechanisms. A hydroboration product is formed in the first case, while in the second case, the

unsaturated substrate is activated directly. This approach of Si-H activation will be utilized in chapter 4.1.

All HS functionalizations require unsaturated substrates like 1-alkenes and 1-alkynes. Another reaction type for hydride-terminated SiNCs is the capping with Grignard or organo-lithium reagents (OLR).[61,62] This method was investigated first at porous silicon by Song *et al.*, then Höhlein *et al.* applied the OLR capping method to SiNCs.[61,63] Co-functionalization was conducted by utilizing various electrophiles at workup, e.g., bromohexane or propylene oxide. After the proton-lithium exchange during the workup in hydrochloric acid, 50% of the Si surface groups stay hydride terminated theoretically (Scheme 5).

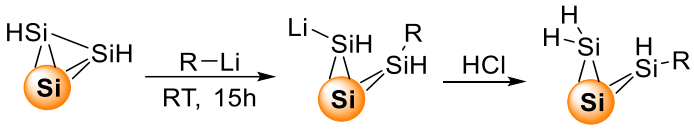


Scheme 5: Proposed reaction mechanism for capping with OLR. Adapted with permission from Ref.[64]

Due to the removal of defect states and the lower surface coverage, OLR-capped SiNCs exhibit three times higher brightness and efficiency when applied in a LED.[64] The influence of the OLR chain length on the Si-LED performance is the subject of thesis chapter 4.5.2.1.

OLR expands the scope of surface moieties compared to HS, as shown in Scheme 6. The phenylacetylene-capped SiNCs exhibited a PL redshift caused by in-gap states which will be discussed further in 2.1.3. The capping of OLR on SiNCs was utilized in a new Janus SiNCs synthesis method described in 4.3.

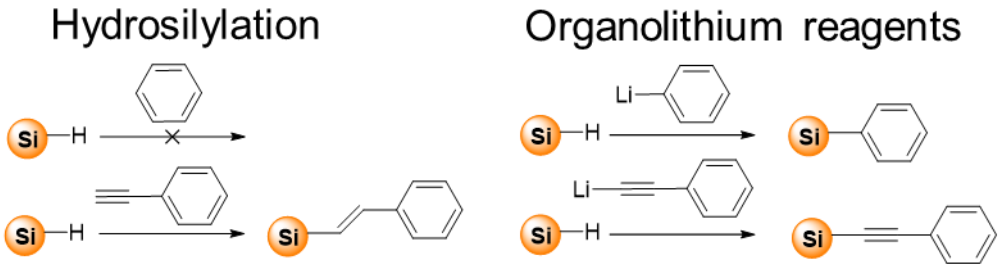


Scheme 6: Comparison of possible capping groups *via* OLR and HS. Adapted from Ref.[65].

For hydride-terminated SiNCs, many functionalization strategies can form Si-C bonds directly. Only a few methods are known for capping with other heteroatomic substrates, like thiols or amines.[66,67] This thesis offers a new functionalization route for SiNCs with several nucleophiles by activation with trityl salts in chapter 4.2.

### 2.1.2.2. Functionalization of Halogen-terminated SiNCs

Halogen-terminated SiNCs are observed upon synthesis from Zintl salts. For SiNCs derived from HSQ, reduction by halogenating agents or activation with $PCl_5$ leads to chlorine-terminated SiNCs. Compared to hydride-terminated SiNCs, these surface moieties

are very reactive toward nucleophiles. Adding Grignard and organolithium reagents leads to relatively stable Si-C bonds, and the reaction of alcohols or amines can result in special Si-Heteroatom bonds. Dasog *et al.* resulted in a blue PL emission by capping with amines.[68] However, the activation with $PCl_5$ etched the SiNCs to smaller sizes, thus lowering the yield. Another drawback is that the halogen-termination itself is rather unstable and hydrolyzes quickly.

#### 2.1.2.3. Multistep Functionalization

Halogen-terminated SiNCs are often involved in multistep functionalizations. Performing two and more steps for SiNC functionalization is necessary for expensive substrates, high stability, or co-functionalization. The group of Zuilhof investigated the thiolene-click chemistry at SiNCs synthesized from a Zintl phase. After first reacting SiNCs with allyl magnesium bromide, various thiols are added to the alkene-terminated SiNCs, and the click reaction is performed under UV light irradiation.[69]

To avoid halogen-containing SiNCs, Höhlein *et al.* functionalized SiNCs with chlorodimethyl-(vinyl)silane (ClDMVS). The SiNCs are then ready for nucleophilic attack and observed only slightly oxidized, unlike at $PCl_5$ activation. With the same first step from the ClDMVS capping, the Ceroni group subsequently introduced PEG and amine groups to the SiNC surface.[70] The obtained nanomaterial exhibited a bright red PL at 750 nm, applicable for bioimaging. A pH-dependent PL was observed for the water-soluble PEG SiNCs.[71]

Combining SiNCs with (in)-organic substrates can lead to synergistic effects with unique properties. Kehrle *et al.* fixed an yttrium containing group-transfer polymerization catalysts on the SiNC surface.[72] The thermoresponsive polymer was grafted from there, and an LCST (lower critical solution temperature) for the resulting nanomaterial was observed.

### 2.1.3. Properties

SiNCs are described by physical and biological properties. The optical PL is characteristic of SiNCs and is tuned by size and surface chemistry. Low cytotoxicity and biocompatibility are desired, especially for applying SiNCs in biomedical fields and consumer products.

#### 2.1.3.1. Physical Properties

Bulk silicon shows semiconducting characteristics, so it is applied in microelectronics as the basis of chips. In contrast to SiNCs, bulk silicon does not exhibit luminescence because of its indirect band gap structure. The energy states of the conduction band (CB) and valence band (VB) adjacent to the band gap possess different wave vectors (k-vectors) in the Brillouin zone, which describes a crystalline primitive cell in the reciprocal space.[73] Transitions within this system are only permitted by phonons, quasi-particles that describe vibrational motion at a single frequency in the crystal lattice. Radiative recombination of one electron and one hole

resulting in photon emission is necessary to achieve luminescence. At bulk silicon, electron-phonon coupling is very unlikely. To realize this transition, the electron momentum needs to be changed by lattice vibration, which is low at room temperature.[74]

Porous and nanocrystalline silicon exhibit luminescence due to a different band structure. Heisenberg's uncertainty principle broadens the exciton (electron-hole pair) wavefunction until they overlap. Hence, it enables a quasi-direct, non-phonon assisted transition, which is more often observable with smaller crystal sizes. The change from an indirect to a direct transition character is indicated by shorter radiative lifetimes. As bulk silicon exhibits PL in the milliseconds' regime, SiNCs show microsecond lifetimes.[75,76] Long-lived PL can also be observed at SiNCs, and it is assumed that emission originates from core states.[77] The overall type of radiative decay in SiNCs has not yet been identified and is a subject of further research.

Size-dependent luminescence is observed by shrinking the silicon nanomaterial below the exciton's Bohr radius. The so-called quantum dots are ruled by quantum confinement to a size-dependent emission maximum. Figure 4 depicts that continuous bands convert to discrete energy levels. The exciton becomes smaller than its radius and behaves like a particle in a box.[78] The band gap widens with smaller crystallite sizes, and the luminescent emission is blue-shifted.

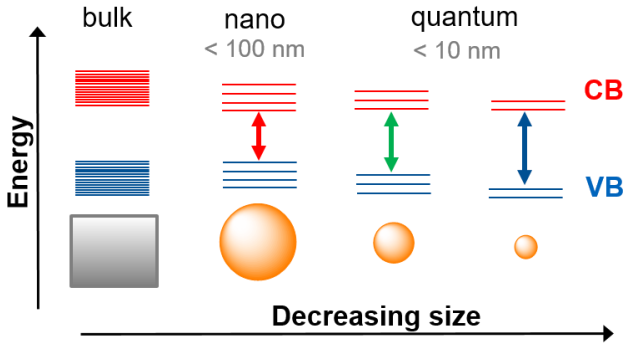


Figure 4: Shrinking material to the nanoscale leads to the discretization of energy and the widening of the band gap.

The effective mass approximation (EMA) predicts the PL emission maximum E(d) of a known semiconducting particle diameter as given by equation (1): [79]

$$E(d) = E_g + \frac{^2\pi^2}{2d^2}\left(\frac{1}{m_e^*} + \frac{1}{m_h^*}\right) - \frac{1.8e^2e}{\varepsilon_i d} \qquad (1)$$

where $E_g$ is the bulk bandgap of Si, d is the diameter of the nanocrystal, $m_e$* and $m_h$* are the effective bulk masses of electron and hole, respectively, e is the charge of the electron, $\hbar$ the reduced Planck constant and $\varepsilon_i$ is the electric permittivity of Si.

In contrast to the EMA, computational calculations of Proot *et al.* in equation (2) reveal a lower exponent of 1.39, which propose an impact of the conduction band's nature.[80]

$$E(d) = E_g + \frac{3.73}{d^{1.39}} \quad (2)$$

Figure 5 shows that the correlation between PL emission and crystallite size deviates from the model and the results of various groups.

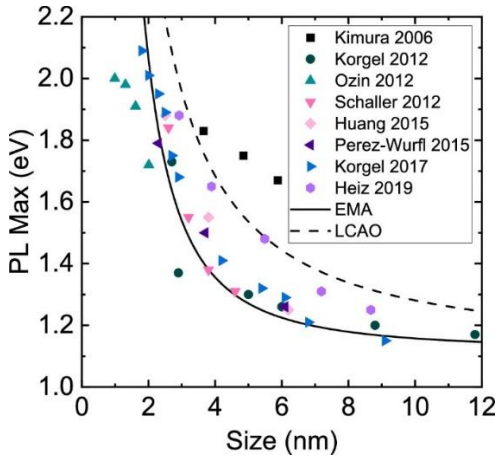


Figure 5: Size-$PL_{max}$ graph with SiNCs of different research groups. Reprinted with permission from A. N. Thiessen, *Chem. Mater.* **2020**, *32*, 6838. Copyright (2023) American Chemical Society.

Different synthesis methods are assumed to cause these deviations, but the origin remains unclear. Mastronardi *et al.* investigated PL emission maximum, lifetime, and absolute quantum yield (AQY) of SiNCs separated in sizes from 1-5 nm.[35] With decreasing SiNC sizes, AQY and lifetime decreased monotonically. It indicated that surface defects and non-radiative vibrations influence the deviations in Figure 5. Without non-radiative recombination centers (e.g., transformation into heat), the single quantum dots exhibited a QY of almost 100%.[81] These results show that the crystallite size contributes less to the SiNC PL than surface moieties like defects or passivating groups. Passivation of SiNCs with organic molecules leads to a core-shell mimicking structure that decreases the number of surface defects.[82]

The synthesis method plays a crucial role for the PL emission. At almost all solution-phase syntheses, residues of various elements like nitrogen, oxygen, or chlorine cause a blue PL with nanosecond excited state lifetimes by charge transfer processes. Additionally, oxide defects on the SiNC surface influence the luminescence. The Veinot group conducted a detailed study about temperature-dependent optical properties with 3 and 5 nm SiNCs from 377 to 37 K capped with amine or alkyl groups.[75] A third group of slightly oxidized alkyl-SiNCs is also investigated. While a band-gap related luminescence for alkyl-capped SiNCs is observed, the oxidized SiNCs exhibit a blue shift in PL and longer lifetimes. The amine-capped SiNCs show nanosecond lifetimes and only a minor sigmoidal-like temperature dependence. These results confirm surface-state dependent charge transfer processes, comparable to $Ce^{3+}$-activated lanthanide silicon oxynitrides.[83] These findings propose emission mechanisms for the three surface groups (Figure 6). Exciton splitting and trapping electrons in surface defect states explain the longer lifetimes of partially oxidized SiNCs.

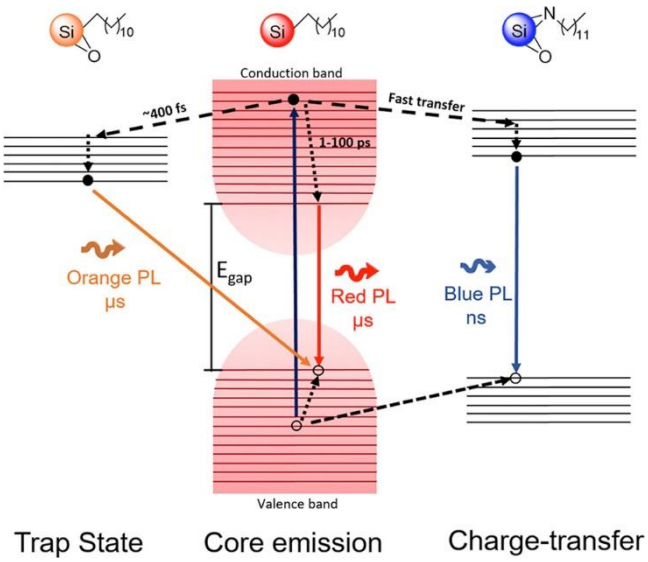


Figure 6: Relaxation types for oxide defects, alkyl-terminated and nitrogen-capped SiNCs. Reprinted with permission from R. Sinelnikov, *ACS Photonics* **2017**, *4*, 1920. Copyright (2023) American Chemical Society.

At the same time, Angı *et al.* investigated in-gap states formed by the functionalization of the SiNCs with alkynylaryls.[84]

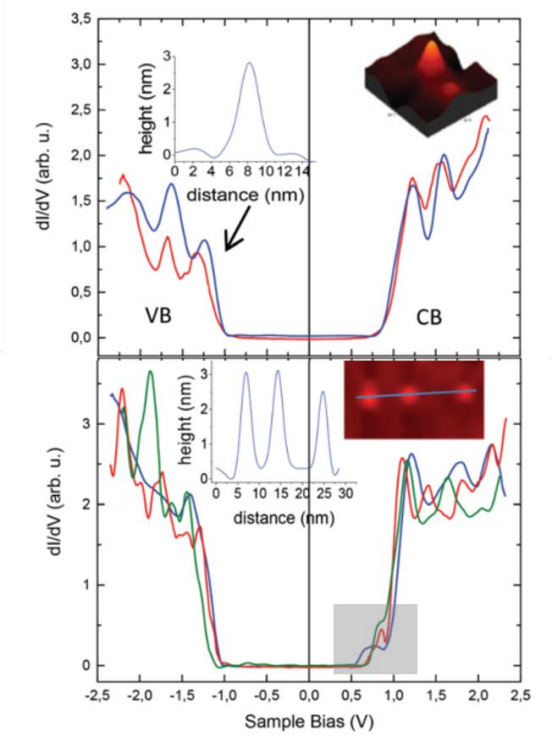


Figure 7: STS spectra of SiNCs capped with hexyl lithium or lithium phenylacteylide. Insets show SiNCs and the respective cross-section. The grey area highlights the in-gap states. Adapted with permission from Ref.[84].

These particles show a PL red-shift from 680 to 730 nm (about 50 nm) compared to alkyl-functionalized ones. This optical phenomenon is caused by in-gap states, confirmed by combined scanning tunneling microscopy and optical spectroscopy (STM/STS). While STM gives insight into the structure and size of SiNCs, STS determines the electronic density of states (DOS) *via* mapping CB and VB. The band gap of 2.2 eV is similar for both functionalization, but Figure 7b in-gap states are displayed near the conduction band edge.

Other than surface groups, the structure of SiNCs also significantly impacts their optical properties. Thiessen, Ha *et al.* determined with solid-state NMR that SiNCs contain core, subsurface, and surface parts identified by different silicon species.[85] The authors investigated SiNCs from 3 to 64 nm and found that SiNCs smaller than 9 nm have diminishing core species and dominating surface species.

The same authors also “overetched” a 9 nm SiNC composite by extended HF etching.[86] 6 nm SiNCs with a red-shifted PL maximum compared to normal etched 6 nm SiNCs were obtained. The scientists measured the crystallite size of both types of SiNCs, determined by an integral breadth method[87] with XRD, and the particle dimension of SiNCs *via* TEM.[86] The different optical properties are due to the smaller crystallite size of the normal etched SiNCs resulting in a thicker amorphous surface layer. Generally, HSQ-derived SiNCs with a thin amorphous layer fit well to EMA size-PL estimations.

In conclusion, luminescence, as the most important physical property of SiNCs, is tuned by size and surface chemistry. It enables the replacement of heavy metal quantum dots in optoelectronic applications. Although much research is performed on electronic relaxation pathways and the influence of surface moieties, the origin of SiNC luminescence has not been derived to date.

#### 2.1.3.2. Biological Properties

Studies concerning cytotoxicity and biocompatibility of SiNCs were performed *in vitro* as well as *in vivo.* Bulk silicon is known to be non-toxic, but nanomaterials exhibit different properties due to their increased surface-to-volume ratio.

The group of Zuilhof performed *in vitro* studies with SiNCs of different surface charges.[88] Cationic SiNCs capped with ammonium showed cytotoxicity, while SiNCs functionalized with carboxylic acid, PEG, or dextran did not. They also observed that higher surface areas and resulting smaller sizes revealed higher toxicity of the cationic SiNCs. Doping with manganese or iron caused only a minor impact on the toxicity.

The influence of the surface group on the cytotoxicity of SiNCs is further investigated by Shiohara *et al.*[89] Epoxide and diol groups on the SiNC surface are compared. While diols show toxicity at 448 µg/mL, the more reactive epoxide group already exhibits 112 µg/mL toxicity. An *in vitro* study with mice and monkeys revealed no toxicity at high intravenous doses of 200 mg/kg.[90] However, the degradation rate of silicon was lower than expected. Residues of silicon were detected in the liver and spleen of mice. These studies showed that SiNCs have less impact on biological species than classical II-VI and III-V nanoparticles.[91,92]

Solubility plays a crucial role in the application, no matter in bioimaging (water) or solution fabrication (org. solvents) as functional films. The biggest challenge of future research is the

long-term stabilization of SiNCs against oxidation. Innovative surface functionalization methods can prevent the loss of specifically tuned optical and solubility properties.

## 2.1.4. Applications

Besides the non-toxic character of SiNCs described in the chapter before, the semiconducting character and versatile reactivity open potential fields of usage. SiNC applications, like optoelectronics, sensors, or bioimaging, are still in a prototype state.

### 2.1.4.1. Bioimaging

Biomedical applications for SiNCs focus on bioimaging, like fluorescent imaging or magnetic resonance imaging (MRI), as an alternative to toxic heavy metal quantum dots. Li *et al.* conducted the first approach of fluorescent imaging in 2004 with polyacrylic acid grafted SiNCs.[93] The surface functionalization protected the SiNCs, conserved the red PL, and kept the particles water-soluble. The cellular uptake of luminescent SiNCs takes place *via* endocytosis. Alsharif *et al.* found that the uptake of SiNCs was faster for malignant cells than for normal primary cells dependent on certain cholesterol derivatives.[94] The most promising approach is capping SiNCs with phospholipids to form micelle-type structures.[95]

A challenging condition for *in vivo* fluorescent bioimaging is the excitation wavelength. While the tissue window ranges from 650 to 900 nm, many SiNCs are only excitable in the UV/blue region. The Kauzlarich group overcame this issue by exciting electrons with two photons.[96] These Mn-doped SiNCs are paramagnetic and potential candidates for MRI contrast agents. Another study attached Gd-chelates on the surface to achieve paramagnetic behavior.[97]

### 2.1.4.1. Sensors

SiNC luminescence can be quenched by chemicals that modify the SiNC surface. This condition is utilized to design SiNC-based sensors. While the first approaches are conducted with the related nanomaterial porous silicon,[98–100] luminescent quantum dot SiNCs are applied by different sensing mechanisms. The most common method utilizes electron transfer from the SiNCs to an acceptor molecule and *vice versa*. The transferred electrons are ruled by the HOMO/LUMO level of the molecule compared to the conduction and valence band of SiNCs. For larger distances (2-8 nm) sensing, another mechanism is performed *via* a non-radiative energy transfer.[101] This dynamic quenching method involves a donor in an excited state and an acceptor in the ground state. Sensing can also be achieved by generating a photocurrent.

SiNC-based sensors are designed for various target substances, like nitroaromatic explosives[102], metal cations[103,104], antibiotics[105], or pesticides[106]. Amine-capped SiNCs achieve to detect pH-values.[107] Despite the various prototypes, low QY and the tendency to oxidation are observed for SiNCs. Further research can improve SiNC sensing performance

by optimizing surface functionalization or developing hybrid composites of SiNCs with polymers or dyes.[108]

#### 2.1.4.1. Solar Cells

Solar cells convert solar energy into electric power; they are essential in increasing the amount of renewable energy. 90% of the solar cells contain bulk silicon because it shows a band gap of 1.1 eV and is available in high purity as single crystals.[109] Nowadays, a conversion of 26% has been reached, which is near the theoretical limit of 30% for crystalline solar cells. This so-called Shockley-Queisser limit depends on the band gap and the solar spectrum.[110,111] The role of SiNCs in solar cells is manifold. As downshifters, they increase solar cells' internal quantum efficiency (IQE) in the UV blue region.[112] As solar concentrators, SiNCs act as waveguides, which trap incoming light.[113] SiNCs extract the energy of hot carriers[114,115], split multiple excitons[116], and reduce reflection.[55]

In classical heterojunction solar cells, a thin film of silicon nanocrystals is embedded in a silicon dioxide layer and placed on top of a traditional silicon wafer. The junction between the silicon and the silicon dioxide creates a built-in electric field, improving the cell's efficiency.[117] Alternatively, SiNCs can be embedded in amorphous Si, silicon nitride, or silicon carbide.[118–120] Tandem solar cells use multiple layers of silicon nanocrystals of different sizes, each optimized to absorb different wavelengths of light. The Green group stacked layers of phosphorous-doped SiNCs on $SiO_X$ on top of each other, reaching a conversion efficiency of 10.6%.[120,121] Hybrid solar cells are the most appropriate type for SiNCs. In combination with organic or inorganic semiconductors, desirable properties of both materials are utilized. Advantages are lower cost and higher efficiency due to a broader wavelength range and improved stability.[109] Furthermore, flexible devices are possible, and in hybrid solar cells, SiNCs can be integrated better into existing stack architectures.[122]

Applying SiNCs in optoelectronics is a prominent field of research besides solar cells. Due to their semiconducting and optical properties, SiNCs can replace heavy metal quantum dots in light-emitting diodes (LEDs) or synaptic devices. The application of SiNCs as an active layer in so-called Si-LEDs is described in chapter 2.3. SiNCs in photodetectors or synaptic devices are reviewed by Ni *et al*.[123]

## 2.2. Silicon Nanosheets

Silicon nanosheets (SiNSs) are a 2D nanomaterial containing silicon. More precisely, SiNSs consist of interconnected $Si_6$ rings and are defined as silicenes and silicanes depending on their hybridization, like their carbon homologs. Silicene exhibits $sp^2$ hybridization and a flat structure. In contrast, silicane, also called hydride-terminated silicene, shows a buckled structure due to the mixed $sp^2$-$sp^3$ hybridization. Despite its unique properties, like conduction along the edges without encapsulation, silicene is highly prone to oxidation. Some publications referred to the material as hydride-terminated SiNSs, or when stacked as layered polysilanes. The following chapter focuses on the synthesis, properties, and possible applications of silicanes.

### 2.2.1. Synthesis Routes

A top-down approach from the Zintl phase $CaSi_2$ can synthesize silicane. This precursor material consists of buckled $(Si^-)_n$ layers of interconnected $Si_6$ cycles stabilized by $Ca^{2+}$ ions. The Si atoms in the rings possess a mixed $sp^2$-$sp^3$ hybridization.

In 1863, Wöhler described the first synthesis of surface oxidized silicon nanosheets, siloxenes, formally $(Si_6H_3(OH)_3)_n$, by treating the $CaSi_2$ with hydrochloric acid at 0 °C.[124] The structure was solved in 1980 by X-ray diffraction (XRD).[125] The buckled main backbone of silicon atoms contains alternating hydride and hydroxide groups.

Freestanding hydride-terminated SiNSs were obtained in 1993 by Dahn *et al.* by reacting $CaSi_2$ with concentrated hydrochloric acid at temperatures below -30°C. This reaction was improved in 1996 by Yamanaka *et al.* under an inert atmosphere.[126,127] The SiNSs were additionally rinsed with HF to remove surface oxygen.[128] However, this etching step also incorporates traces of oxygen onto the material surface (Si-OH and Si-O-Si), so no oxygen-free SiNSs synthesis is known to date.[129]

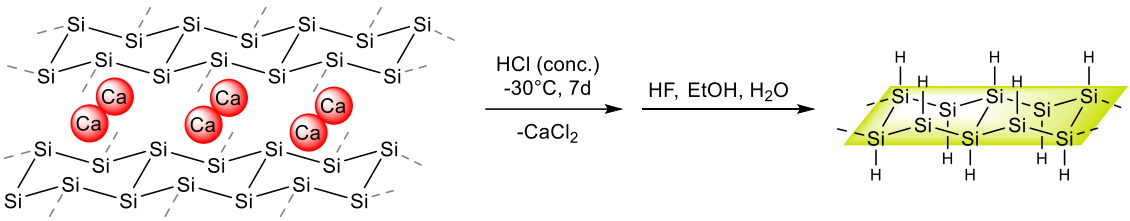


Scheme 7: Synthesis of hydride-terminated SiNSs by exfoliation from the Zintl phase $CaSi_2$ with subsequent HF etching.

Besides hydride-terminated SiNSs, halogen-terminated SiNSs can also be prepared. For the exfoliation from $CaSi_2$, HBr in an $AlBr_3$ melt was used by Schott *et al*. to yield bromine-terminated SiNSs.[130] In the presence of ICl, chlorine-terminated SiNSs are obtained.[131] However, these types of SiNSs are not well characterized. Nakano *et al.* observed that the exfoliation of $CaSi_{1.85}Mg_{0.15}$ to form Mg-doped SiNSs was facilitated by reducing the charge on

the silicon backbone.[132] Besides desired doping with elements, commercially available $CaSi_2$ possesses technical grade and is contaminated with different byphases. This $CaSi_2$ is insufficient for research on SiNSs, influencing the optical and semiconducting properties of the derived nanomaterial.

A completely different synthesis approach was conducted using chemical vapor deposition of $SiCl_4$ to yield silicane.[133] A significant advantage of this method is tuning the layer thickness by varying the growth time. However, this synthesis only applies to small scales in contrast to gram scale exfoliation out of Zintl phases.

### 2.2.2. Surface Functionalization

Silicane often exists as stacks to increase stability. Despite reduced accessible surface area due to this stacking, oxidation is not prevented entirely. One solution to overcome this disadvantage is capping the material with organic molecules, thus preserving the material properties and enhancing dispersibility. In contrast to SiNCs, only a few functionalization methods are known for SiNSs. Okamoto *et al.,* for example, capped SiNSs with different amines in chloroform at 60 °C for 12h. Thus, alkylamine-SiNSs formed stacked structures with bilayered alkyl chains between the sheets without solvent.[134] Functionalizing SiNSs with the Grignard reagent phenyl magnesium bromide led to phenyl-capped SiNS layers.[135] A film of this material exhibited a photocurrent *via* band gap transition with irradiation of 420 nm and lower.

The most common functionalization method for silicon nanomaterials, hydrosilylation (HS), is also used for SiNSs. Besides thermal initiation, several initiators like Lewis acids[136], AIBN[137], diazonium salts[138], and iodonium salts[49] were investigated. Pt-catalyzed HS of SiNSs with 1-hexene yielded stable dispersions in chloroform.[139] No information is reported about the luminescence of this material. UV-induced HS is found to be useless for SiNSs, as the material is not photostable. This fact is exploited to liberate SiNCs which were masked by SiNSs for anisotropic functionalization.

Thermally initiated HS with *t*-butyl methacrylate (tBuMA) led to unintended polymerization by forming poly(tert-butyl methacrylate).[138] The hybrid material obtained in this reaction was not characterized further. SiNSs decomposed upon exposition to UV light or basic conditions. For protection against these external influences, SiNSs were embedded in polymer matrices during functionalization.[137] Besides styrene, methyl methacrylate and acrylic acid were investigated as capping groups and monomers for the SiNSs matrix. Figure 8 shows SiNSs embedded in polystyrene. The optical properties of SiNSs were preserved under irradiation with UV light for up to 25 h. In the following study, the same authors investigated the applicability of these covalent SiNS polymer composites for photosensitive devices, which

showed a current response when illuminated with a commercially available energy-saving lamp.[140]

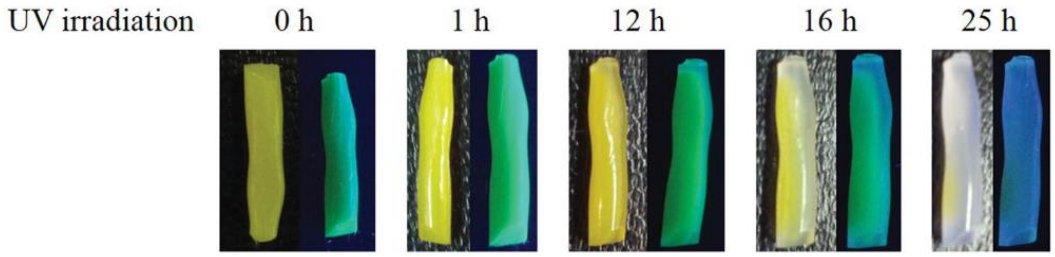


Figure 8: SiNSs embedded in polystyrene after given UV irradiation time at daylight (left) and at UV light (right). Reprinted with permission from Ref.[137].

While the previously described polymerization was induced exclusively by heat or radical initiators, diaryliodonium salts required the presence of SiNSs to induce cationic and radical polymerization.[141] Kloberg *et al.* investigated the ring-opening polymerization of heterocycles like THF with simultaneous encapsulation of SiNSs in a polymer matrix. In this case, no covalent capping of the SiNS surface was obtained. Also, co-initiation of SiNSs was observed for radical polymerization of tBuMA, methyl methacrylate, and acrylic acid, yielding SiNS polymer composites.

Generally, research lacks a surface functionalization method for SiNSs, which achieves complete surface coverage. The unfunctionalized Si-H moieties are targets for oxidation.

### 2.2.3. Properties

The properties of silicanes were investigated in various computational studies. Mainly, the electronic structure of silicanes was determined theoretically. Depending on the calculation model and conditions, the band gap was determined to vary from 2.19 eV to an almost direct band gap of 2.75 eV for hydride-terminated SiNSs. Physical strain in the 2D nanomaterial structure tuned the band gap transition type. At symmetrical tension, the indirect band gap remained, while at asymmetrical strain, the band gap turned into a more direct type.[142] In contrast to unstrained hydride terminated SiNSs, a tensile strain of 1.6% increased the electron mobility significantly from 464 to 8551 $cm^2/Vs$.[143] Hexyl-capped SiNSs rendered the most stable structure when the surface groups were uniformly distributed due to their electrostatic repulsion.[144]

To a certain degree, the optical properties of hydride-terminated SiNSs correlate with the electronic structure and depend on internal (e.g., physical strain) and external influences (e.g., electric field).[145] Therefore, experiments are necessary to investigate realistic materials and their properties. Structurally, hydride-terminated SiNSs are based on a honeycomb buckled Si(111) lattice due to $sp^3$ hybridization. In contrast to the $(Si^-)_n$ layers in the Zintl phase, where ionic interactions with the $Ca^{2+}$ rule, layered polysilane showed only weak van der Waals

interactions.[10] Ryan *et al.* compared in a comprehensive study theoretical results with experimental findings concerning the structure of SiNSs obtained from exfoliating $CaSi_2$ at cold temperatures (-30 °C).[146] Energy dispersive X-Ray spectroscopy (EDS), Raman, and FT-IR exhibited the proposed monohydride-terminated silicane with some chloride and hydroxide surface species. Simulated FT-IR, Raman, and solid-state NMR spectra with density functional theory fit well with the experimental results. (Partially) oxidized moieties were not considered in the computation and caused deviation from the experimental results. The calculations were based on the monohydride-terminated buckled SiNS layer model.

The electronic structure is related to the optical absorption behavior. In SiNSs, it originates from $\sigma \rightarrow \sigma^*$ transitions in the σ-conjugated system, derived by diffuse scattering.[147] The surface group influences the absorption maximum. While hydride-terminated SiNSs exhibited an absorption maximum of 2.4 eV, hexyl-capping absorbed mostly at 4.2 eV.[127,139]

As another essential property of SiNSs with regard to applications, PL emission is characterized by fluorescence spectroscopy. Size-dependent excitonic recombination of electron holes and electrons and surface-dependent trapping of charge carriers influence optical emission. As an example of the size dependency, Kim *et al.* synthesized SiNSs by chemical vapor deposition of $SiCl_4$ with different thicknesses from 1-13 nm tuned by growth time.[133] The PL emission varied from 385 to 765 nm within the visible spectrum. Surface functionalization also impacts PL emission. While hydride-terminated SiNSs exhibited an emission around 500 nm, Mg-doped SiNSs were reported to emit at 435 nm.[132,146] Aryl-capped SiNSs obtained from phenylmagnesium bromide showed PL at 415 nm. Irrespective of the alkyl chain length, SiNSs functionalized with different n-alkylamines exhibited an emission at 438 nm.[134] Generally, surface functionalization of SiNSs is ineffective in avoiding oxidation and resulting defect states. Despite some methods of tuning the band gap, most SiNS emit in the blue to the green spectral range.

SiNSs show PL only under UV light but degrade at the same time upon long-term irradiation. That behavior resembles the Staebler-Wronski effect observed in amorphous silicon thin-films, where photoconductivity diminishes under prolonged irradiation.[148] Their σ-conjugative character explains the photodegradation of SiNSs. Irradiation enhances electron transitions from σ to σ*, thus weakening the Si-Si bonds. The framework degrades by inserting oxygen traces on the system's surface.[149] This property was utilized to synthesize anisotropic Janus SiNC, which became liberated from the SiNS mask by UV light.[48] A more detailed description is found in 4.3.

Besides linear optical properties, the Z scan technique investigated the non-linear optics (NLO) of SiNSs. By excitation with laser pulses, the SiNS response deviates from the linear model of Lambert-Beer law when the sample is moved along the z-axis in and out of the laser beam

focus. The group of Prof. Stelios Couris investigated that dodecyl-functionalized SiNSs exhibit a very high NLO absorption, twice as high as hydride-terminated SiNSs.[150] These results demonstrate the potential of functionalized SiNSs for sensor or laser applications.

Experimental literature lacks reporting size distributions of the observed SiNSs. It also remains unclear whether the size of the SiNSs increases the electron mobility like observed at large area graphene.[151] A method for interconnecting SiNSs at the edges with silanes is investigated in chapter 4.1.

The surface Si-H moieties show a reductive potential that enables reducing metal salts to elemental metal nanoparticles, which decorate the 2D silicon nanomaterial. The resulting hybrid materials with noble metal nanoparticles are used as catalysts for $CO_2$ reduction or decomposition of formic acid.[152,153] In chapter 4.4. the catalytic activity of a hybrid material containing SiNSs and palladium nanoparticles generates movement.

### 2.2.4. Applications

Similar to SiNCs, applications of SiNSs are in the prototype state. SiNSs capped with organic ligands show good dispersibility in organic solvents enabling spin-coating and ink-printing. These solution fabrication techniques are employed for devices in energy storage[154], optoelectronics[133], catalysis[152], and bioapplications[155].

Due to its high affinity to lithium, silicon is a promising candidate as an anode material in lithium-ion batteries. In contrast to employed carbon materials, the theoretical capacity lies one magnitude higher at 3579 mAh/g for $Li_{15}Si_4$.[156] Silicane was investigated as an anode material for energy storage by Nakano and coworkers.[154] The material remained amorphous during the lithium charge-discharge cycle, thus leading to a lower volume expansion in contrast to silicon powder anodes.

In the field of biosensors, SiNSs are a promising candidate due to their semiconducting properties. Electrolyte-gated field-effect transistors (EGFETs) from a composite material of SiNSs hydrosilylated with ethynylaryls and the conjugative polymer poly(3-hexylthiophene) were built by Lyuleeva *et al*.[155] The sensor setup contained a thin film of the SiNS composite material, and DI (deionized) water was used as an analyte. The composition of the SiNS hybrid film enabled charge transfer doping due to the π-π stacking of the conjugated system. The sensor showed the best ON/OFF ratio of $8.3 \times 10^2$ compared to polymeric silanes or SiNCs.

As mentioned in 2.2.3, Kim *et al.* performed dendritic growth of SiNSs from $SiCl_4$ vapors, tuning the resulting SiNS size by the growth time.[133] The luminescent SiNSs were employed as an active layer in white and blue OLEDs. No information was provided about the OLED efficiency. Application of SiNS in optoelectronics is a challenging task due to a higher tendency toward oxidation, thus decreasing long-term stability under ambient conditions. Also, the optical

emission is less efficient and less tunable than SiNCs. More research on silicon nanomaterial-based OLEDs is conducted with SiNCs, which is described in the next chapter.

## 2.3. SiNC Based Light-Emitting Diodes

Since the invention of the light bulb by Edison in the year 1879 to replace candlelight, the development of luminescent devices has been an ongoing field of research. After the mass production of inorganic LEDs in the 1960s, the first organic LED (OLED) was designed by Tang *et al*. in 1987.[157] OLEDs differ from conventional inorganic LEDs because they exhibit two differently doped semiconductor regions, forming a p-n-junction. OLEDs use a layered approach with different materials, where one transparent electrode is required to achieve light extraction. The overall principle is based on the recombination of electrons and holes in the active layer leading to light emission. Interlayers between the electrodes and the luminescent layer enhance charge carrier transportation. Gas-phase and liquid processing methods apply up to ten different layers containing small molecules like triphenylamine or conductive polymers.[158] OLEDs exhibit advantages like good viewing angles and high contrast. However, lifetime and color purity are low. QD-LEDs combine the benefit of both inorganic emission stability and organic solution processability. Compared to conventional OLEDs, QD-LEDs show more narrow emission lines, leading to a better recording of colors and no risk of burn-in.

Colvin *et al.* invented the first QD-LED in 1994 containing CdSe nanoparticles.[159] This material belongs to group II–VI and III–V quantum dots like CdS or ZnSe, which have been applied in commercially available displays since 2009.[160] The heavy metals employed in the QDs are toxic and rarely abundant. The European directive restrictive of certain hazardous substances (RoHS) wanted to restrict cadmium and other toxic substances from electric devices until 2017. In the case of missing alternatives, the materials can be used exceptionally.[161]

SiNCs are promising candidates for a non-toxic and a more sustainable alternative for optoelectronic devices because they are luminescent under irradiation of UV light as well as by applying voltage. In 2010 Cheng *et al.* built the first OLED with SiNCs as an emissive layer, the so-called Si-LED.[162] Objective criteria for high-performing QD-LEDs, specifically Si-LEDs, are a high external quantum efficiency (EQE), low turn-on voltage, and high brightness. In the case of Cheng *et al.,* the follow-up Si-LEDs in 2011 with a peak EQE of 8% emitted in the IR spectral range, invisible to the human eye.[163] Higher current densities were obtained in the visible region, decreasing the EQE below 1%.

The EQE is calculated by the ratio of photons emitted into free space $N_{\mathrm{photon}}$ compared to the injected electrons into the LED $N_{\mathrm{electron}}$:[164]

$$EQE = \frac{N_{\mathrm{photon}}}{N_{\mathrm{electron}}} \tag{3}$$

After the adoption of equation (3) to the specific measurement setup with an integrating sphere, the EQE is calculated following:

$$EQE = \frac{A \cdot e}{h \cdot c \cdot I} \int_0^{\infty} E_{e,\lambda} \cdot \lambda \; d\lambda \tag{4}$$

where $A$ is the LED area, $e$ is the elementary charge, $h$ is the Planck constant, $c$ is the speed of light, $I$ is the injected current, $E_{e,\lambda}$ is the spectral irradiance, and λ is the wavelength.

To increase the EQE, additional interlayers in the device stack are necessary, decreasing the energy steps between the layer materials and enhancing the charge transport to the emissive layer. The different layers of an exemplary Si-LED stack and the general working principle are depicted in Figure 9. While the cathode injects electrons, holes are injected in the anode. Both charge carriers move to the emissive layer, where recombination and photon emission occur. The stack is built on a glass substrate with a pre-fixed transparent ITO electrode. Due to its high conductivity and low work function, it is an ideal anode material for Si-LEDs. The PEDOT:PSS acts as a hole injection layer, lowering the potential barrier between the anode and emissive layer. PolyTPD is the electron blocking layer (EBL), preventing leakage currents from the active layer to the anode. However, PolyTPD can disturb the electroluminescence because it is a blue-emitting polymer, but the blue emission is eliminated with the correct charge carrier confinement. ZnO is applied as a hole-blocking layer to confine the charges in the active layer.

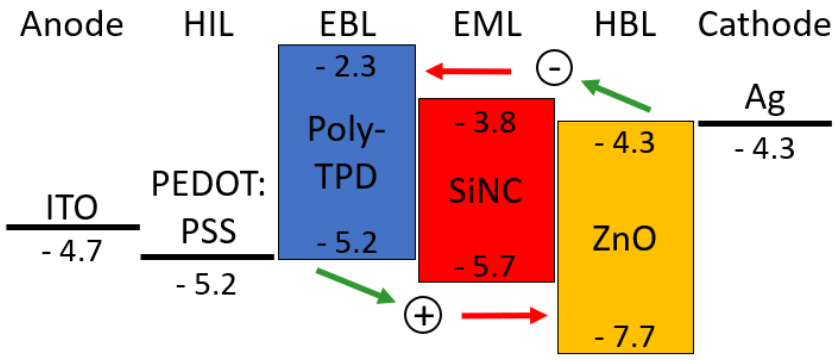


Figure 9: Working principle of a Si-LED. The values show the work function energies.

Also, inverted OLED stacks are known for Si-LEDs, where the ITO layer injects the electrons, and the metal electrode serves as the anode.[165] This configuration leads to a more stable device because the organic layers are better protected from air and moisture when less sensitive inorganic layers are at the top. Ghosh *et al.* fabricated flexible devices by an inverted stack architecture with a longer lifetime compared to conventional structures.[166]

Tuning the EQE and emission color of the Si-LEDs can be further achieved by particle size. Due to quantum confinement, the emission maximum of the Si-LEDs can be adjusted by the

SiNC size. However, luminescence is observed mainly in the orange to IR regime.[35] Maier-Flaig *et al.* investigated allylbenzene-capped SiNCs with 1.3, 1.6, and 1.8 nm particle sizes observed by size separation.[167] The built Si-LEDs of the three sizes exhibit emission maxima from 625 nm to 680 nm and a reduced full-width half maximum (FWHM) of ~100 nm. Yamada *et al.* built Si-LEDs with SiNCs passivated with 1-decene and sizes ranging from 1.3 to 2.7 nm in five groups. They found for decreasing particle size a decreasing QY, which in turn resulted in a decreasing EQE for reduced particle size.

Besides the SiNC size, the SiNC surface functionalization influences the Si-LED performance. The difference between aromatic and aliphatic surface groups for SiNCs in Si-LEDs was investigated by Liu *et al.*[168] They functionalized SiNCs with phenylpropyl (PhPr) and octyl substituents by the common hydrosilylation (HS) method. Employed in Si-LEDs, the PhPr-capped SiNCs exhibited a higher optical power density of 0.64 mW/cm$^2$ compared to SiNCs with octyl groups (0.34 mW/cm$^2$). However, the peak EQE was 1.1% and, therefore, lower than the octyl-SiNCs (6.2% in the near IR emission) because the PhPr-SiNCs showed more oxidation and fewer defects. Recently, Xu *et al.* presented capped SiNCs *via* thermal hydrosilylation in neat decene tuning the surface coverage by reaction time from 10 min up to 9 h.[169] The varied surface coverage did not affect the optical properties concerning PL emission maximum and quantum yield. Employed in LEDs, SiNCs hydrosilylated for only 10 min reached a surface coverage of 20% and the best EQE of 1.8%. SiNCs with more than 50% coverage of Si-O and decyl groups reduced the LED performance. In conclusion, a lower surface coverage leads to more efficient Si-LEDs. These results confirm the findings of Loch *et al.* comparing SiNCs functionalized by hexene *via* HS or hexyl lithium (HexLi) *via* OLR.[170] Due to the mechanistically lower surface coverage of the HexLi-capped SiNCs, less serial resistance in the devices is observed (see 2.1.2.1). As a result, three times higher EQE of $1.8 \times 10^{-2}$% and brightness was observed for SiNCs.

These studies reveal that SiNCs are a reasonable alternative for heavy metal QD-LEDs. Still, further research and optimization are necessary when Si-LEDs shall find a way to commercial Si-LED displays.

# 3. Aim and Guideline of the Thesis

0D and 2D silicon nanomaterials are established in our group, and many researchers optimize the synthesis. Both materials are promising candidates for applications. At SiNCs, the emission color can be tuned by size and surface group. Moreover, capped SiNCs are dispersible in organic solvents and are applicable by spin-, spray- or ink-coating. SiNSs, as the graphene homolog, exhibit semiconducting properties in two dimensions. Enlarging this system by connecting nanosheets increases the attractivity for application.

Silicon nanomaterials are prone to oxidation in the ambient atmosphere due to the high Si-O bond strength. Surface functionalization is crucial to protect from oxidation and enhance solubility. Using HS for silicon nanomaterial surface capping has been established over decades, and various initiation mechanisms and agents have been developed. But this method can insert only Si-C bonds and lacks tuning optical properties by introducing heteroatoms on the silicon nanomaterial's surface. This thesis offers mechanistic insights and widens the scope and functionalization mechanism with the versatile reactivity of silicon surface atoms.

The overall aim is to broaden the knowledge about silicon nanomaterials' reactivity and properties and find possible applications. Silicon is a non-toxic and abundant material, thus a promising candidate for several fields of applications, e.g., optoelectronics, biomedicine, bioimaging, and energy storage. This thesis covers the development of SiNSs to self-propelling systems and the replacement of heavy metal QDs in optoelectronic devices.

Due to the broad range of surface functionalization and possible applications, the thesis is subdivided into five research projects. Each chapter contains an introduction, results, and discussion section on the respective topic. Finally, the research findings are concluded and an outlook on possible research is given. The experimental details are summarized at the end of the thesis.

At first, the development of surface functionalization to improve the structure (*dehydrogenative coupling with silanes*) and optical properties (*trityl-induced activation*) of silicon nanomaterials. The third chapter deals with an enhanced synthesis route of *Janus SiNC via organolithium reagents*. The last two projects cover the application of silicon nanomaterials. Pioneering studies utilized SiNSs decorated with metal nanoparticles as *nanomotors*. In the last project, advanced investigations were performed on surface-capped *SiNCs as a luminescent layer in Si-LEDs*.

# 4. Projects

## 4.1. Homonuclear Dehydrogenative Coupling

### 4.1.1. Introduction

Dehydrogenative coupling (DHC) describes a reaction of X-X bond formation under hydrogen evolution. The most prominent reactants are molecules with light group IV elements, like silanes and germanes. Representative reactants for this reaction type are hydrosilanes and hydrogermanes.

While heteronuclear DHC occurs between two sorts of hydrogenated elements under the formation of X-Y bonds, homonuclear coupling needs just one kind and forms X-X bonds (Scheme 8).

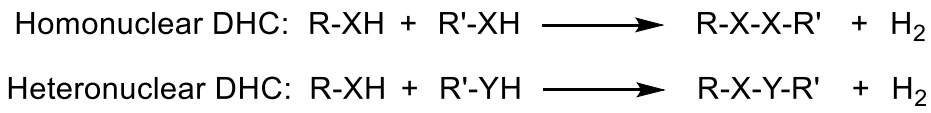


Scheme 8: General reaction equation for homo- and heteronuclear DHC.

Homonuclear coupling of molecular silanes to oligo- or polysilane requires catalysts. Veinot *et al.* applied this reaction type to SiNCs. They performed the DHC at SiNCs using Wilkinson's catalyst with different primary and tertiary silanes. Upon reaction, the functionalized SiNCs lost their photoluminescence.[171]

Sailor *et al.* invented the thermally induced homonuclear DHC of silanes on porous silicon.[172] The silane functionalization protected the surface from further etching during exposure to HF. Also, heteronuclear DHC is already investigated on group IV nanomaterials. Yu *et al.* showed the synthesis of a hybrid material containing germanium nanosheets decorated with silicon nanocrystals.[173]

Regardless of germanium or silicon nanosheets, an interesting aim of research on 2D-nanomaterials is to enlarge the dimensions in the x and y directions. Especially for SiNSs, the linkage between the edges of the nanosheets is required to enhance the electrical and optical properties. The focus should also lie on fixing structural defects in the nanomaterial. Thus, homonuclear DHC between SiNSs and silanes might be key to achieving these research aims. Unforeseen and enhanced properties could be reached by forming Si-Si bonds on the surface of silicon nanosheets, as the semiconducting system will be enlarged out of the plane.

Surface functionalization of silicon nanomaterials requires activation of the surface moieties, which is performed mainly by thermal or radical initiation. HS reactions, the most common method for surface modification of silicon nanomaterials, are initiated by light or Lewis acids (LAs).[47,60,136] With boron-containing LAs, hydroboration products are assumed as intermediates. Direct activation of the added unsaturated surface substrate is also considered.

Vinylsilanes, for example, stabilize the generated positive charge on the SiNS surface according to *Helbich et al.*, so for such moieties higher reactivity for addition is needed.[136] Activation of the Si-H bond is crucial for the success of DHC because the desired Si-Si bonds exhibit a dissociation energy of 300 kJ/mol that is slightly lower than for Si-H bonds (320 kJ/mol) (Scheme 9). Si-H activation mechanisms are based on the polarization of the respective bond. Therefore, several approaches use metals for oxidative addition or bond metathesis.[174,175]

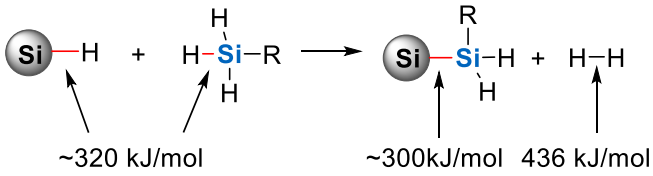


Scheme 9: General reaction scheme of DHC with dissociation energies assigned to involved bonds.[176]

In this chapter, DHC with various initiator mechanisms is used for coupling SiNSs and SiNCs with primary and tertiary silanes. After some preliminary experiments, it is focused on LA-induced approaches.

## 4.1.2. Results and Discussion

### 4.1.2.1. First DHC Reactions with Silicon Nanosheets

Silicon nanosheets are functionalized with tertiary silanes and different initiators to investigate various methods of Si-H bond activation (Scheme 10). Three initiation mechanisms are tested: thermal, catalytic, and radical DHC.

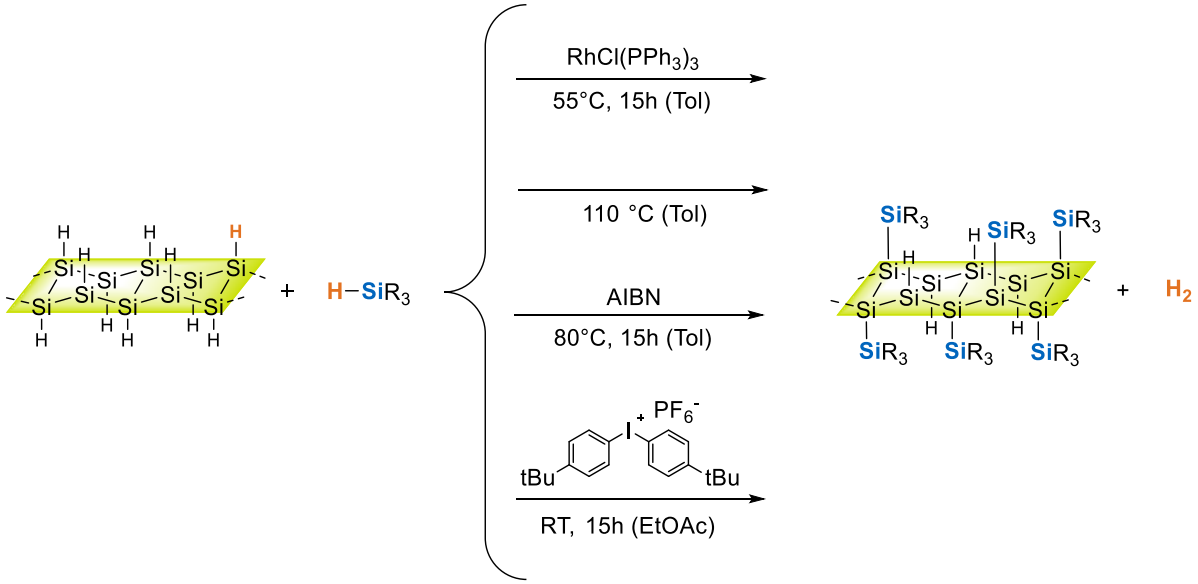


Scheme 10: Reaction scheme of DHC of SiNSs with different initiation mechanisms (from top to bottom): catalytic, thermal, radical with AIBN and bis(4-*tert*-butyl-phenyl)iodonium hexafluorophosphate (BIP). R= octyl, ethyl.

Thermal initiation takes place without any catalyst. SiNSs and silane are diluted in toluene in a Schlenk tube and heated to the maximum applicable temperature of 110°C. Above this

temperature, the DHC of the SiNSs with itself is observed.[177] Catalytic DHC with Wilkinson's catalyst is utilized for SiNS functionalization under similar conditions as used by Veinot *et al.*[2] For radical-induced DHC, two different initiators are investigated. Functionalization with commonly used AIBN occurs at 80 °C, while the initiation with iodonium salt BIP is performed at room temperature. Figure 10 shows the FT-IR spectra of the obtained DHC products and compares the different initiation processes.

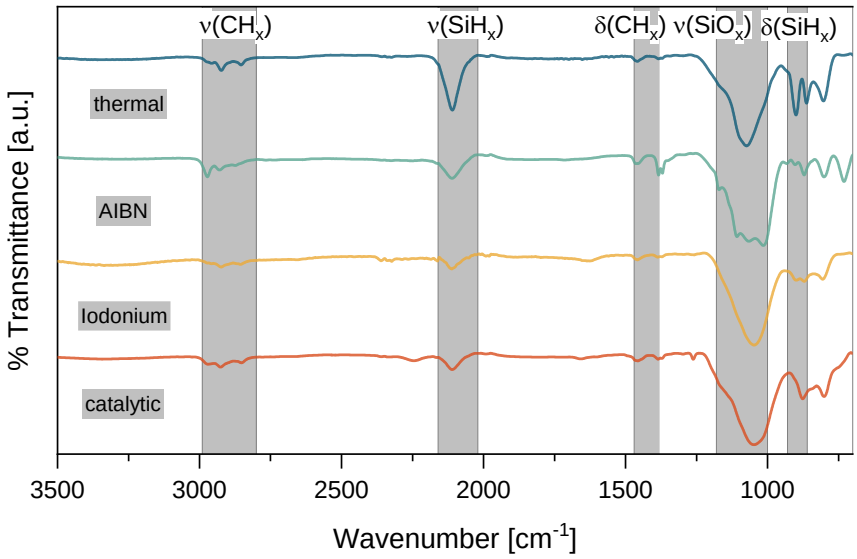


Figure 10: FT-IR spectra of the preliminary experiments with different initiation mechanisms.

All FT-IR spectra show the $SiO_x$ stretching signal at 1050 $cm^{-1}$ besides a weak $SiH_x$- stretching vibration band at 2100 $cm^{-1}$. An unexpected low signal is observed in the region for aliphatic $CH_x$ stretching. The PL spectra of the obtained DHC products show only the typical PL maximum at 520 nm for thermally functionalized SiNSs (Figure 11). In the case of catalytic DHC, photoluminescence is assumed to be quenched by rhodium-containing surface adducts.[171]

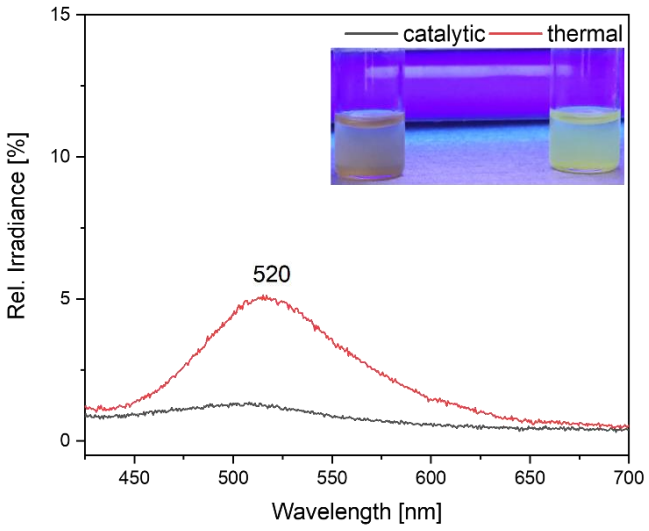


Figure 11: PL- spectra of catalytically and thermally functionalized SiNSs *via* DHC with trioctylsilane. Inset: Photo of the dispersions under UV light.

In conclusion, all the approaches described above lead to unwanted surface oxidation and unsuccessful surface functionalization. So, other methods of Si-H activation need to be considered for a successful passivation. LA-induced DHC is therefore regarded.

#### 4.1.2.2. Lewis-Acid Induced DHC with Silicon Nanocrystals

While the preliminary experiments in 4.1.2.1 are conducted with SiNSs, further investigation of DHC, especially initiation with LA, is performed with SiNCs. By utilizing SiNCs, it is easier to indicate a successful functionalization, as the reaction solution with the capped SiNCs turns clear. Furthermore, SiNCs are less prone to oxidation and more resistant to destructive conditions (e.g., UV light, basic conditions) than SiNSs. A drawback of experiments with SiNCs is the more complicated workup. The SiNCs need to be separated *via* precipitation from an unreacted substrate which exhibits similar dissolving properties as the functionalized nanomaterial. Either the yield of SiNCs is reduced during workup or residues of the substrate are removed insufficiently. Using aliphatic primary silanes instead of tertiary silanes could further enhance surface functionalization because of a lower steric hindrance at the Si atom. Boron compounds were already utilized as HS initiators.[60,136] The Si-H activation is assumed to happen *via* polarization of the respective bond. For this set of experiments, four different boron-containing Lewis acids are used to initialize the DHC, depicted in Scheme 11.

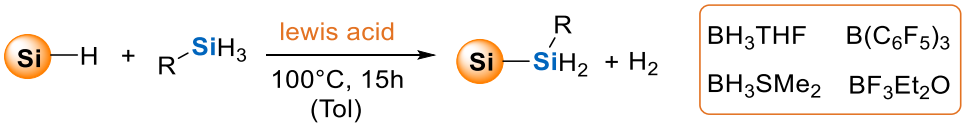


Scheme 11: Si-H activation of SiNCs and silanes with LA.

Only for $BH_3$·THF, a clear DHC reaction solution was observed with octadecylsilane after stirring at 100°C overnight (Figure 12a). Compared to the preliminary experiments of the previous chapter, the FT-IR spectra in Figure 12b show significantly lower surface oxidation as the $SiO_x$ signal at 1050 $cm^{-1}$ is weaker. Also, the aliphatic $CH_x$ stretching is enhanced, indicating higher surface functionalization. However, the $SiH_x$ stretching signal shows some unreacted Si-H moieties. With the standard workup procedure, BCF was separated incompletely because an aromatic $CH_x$ stretching signal at 1640 $cm^{-1}$ is visible.

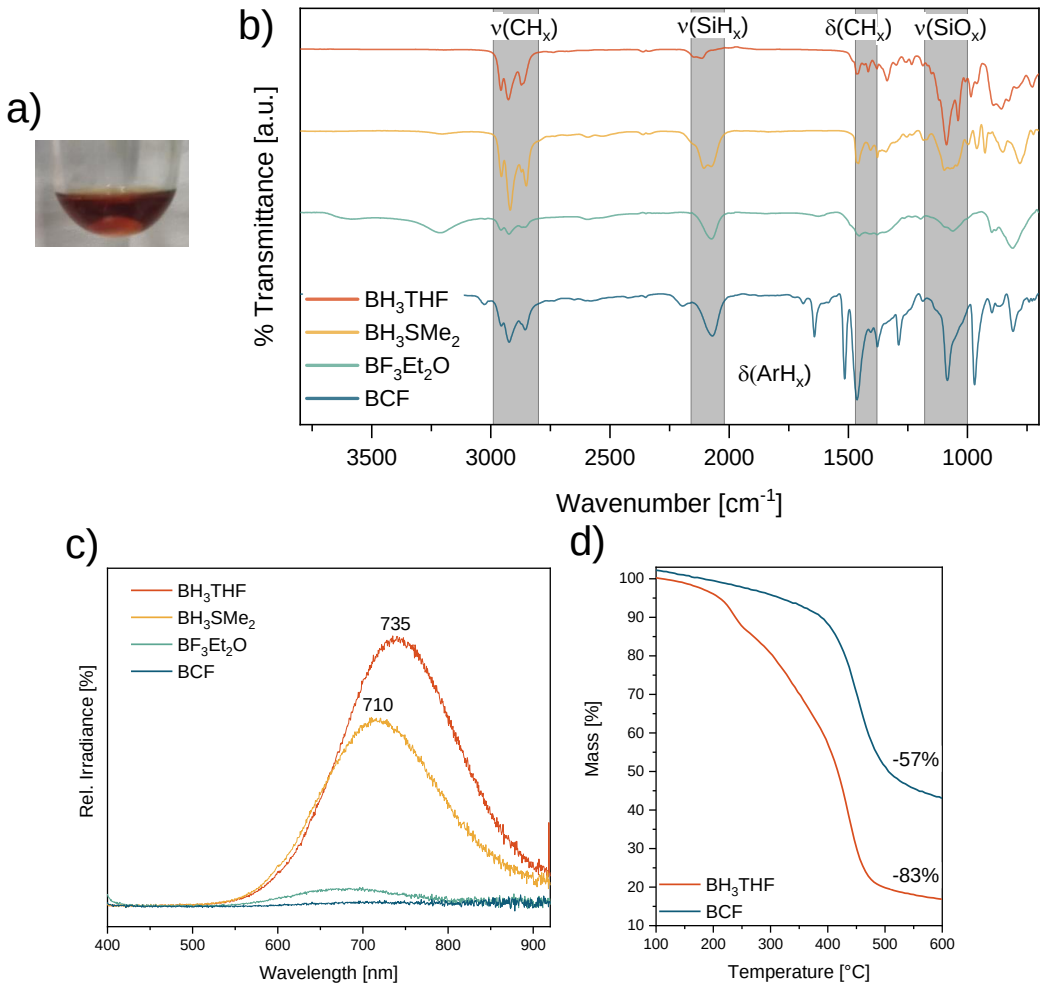


Figure 12: a) Photograph of reaction solution of SiNCs coupled with octadecylsilane under the initiation of $BH_3$·THF. b) FT-IR spectra of SiNCs functionalized *via* DHC initiated by different LAs. c) PL spectra of functionalized SiNCs initiated by different LAs. d) TGA of functionalized SiNCs initiated by $BH_3$·THF and BCF.

The PL spectra exhibit a for SiNCs typical red PL with an emission maximum of around 700 to 750 nm only for initiation with borane adducts. This confirms the results of the FT-IR measurements The SiNCs functionalized by the initiation of BCF show no PL. It is surprising that BCF, as a standard compound for catalysis of Si-H activation, failed.[5] TGA measurements detect a significantly lower surface coverage with the BCF initiator in contrast to $BH_3$·THF, consistent with FT-IR and PL analysis.

A temperature of 100 °C is crucial for successful functionalization. Experiments performed at 80 °C or room temperature remain opaque even at longer reaction times, and the FT-IR shows a high amount of oxidation. Screening the LA showed that $BH_3$·THF is the best DHC initiator for SiNCs functionalization. In the next step, the silane substrate is varied. Scheme 12 depicts the reaction scheme and scope of tested silanes. Octadecylsilane was already used for LAs experiment row.

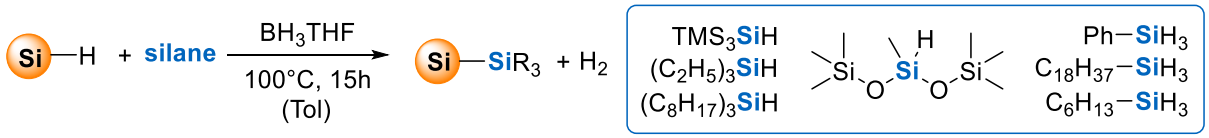


Scheme 12: Reaction scheme DHC of SiNCs with different silanes.

Besides aliphatic primary silanes, phenylsilane with its aromatic side chain is investigated. Tertiary silanes with aliphatic octyl chains or trimethylsilyl (TMS)-groups are studied. A dialkoxysilane is also used as a surface group to investigate electron-withdrawing substituents.

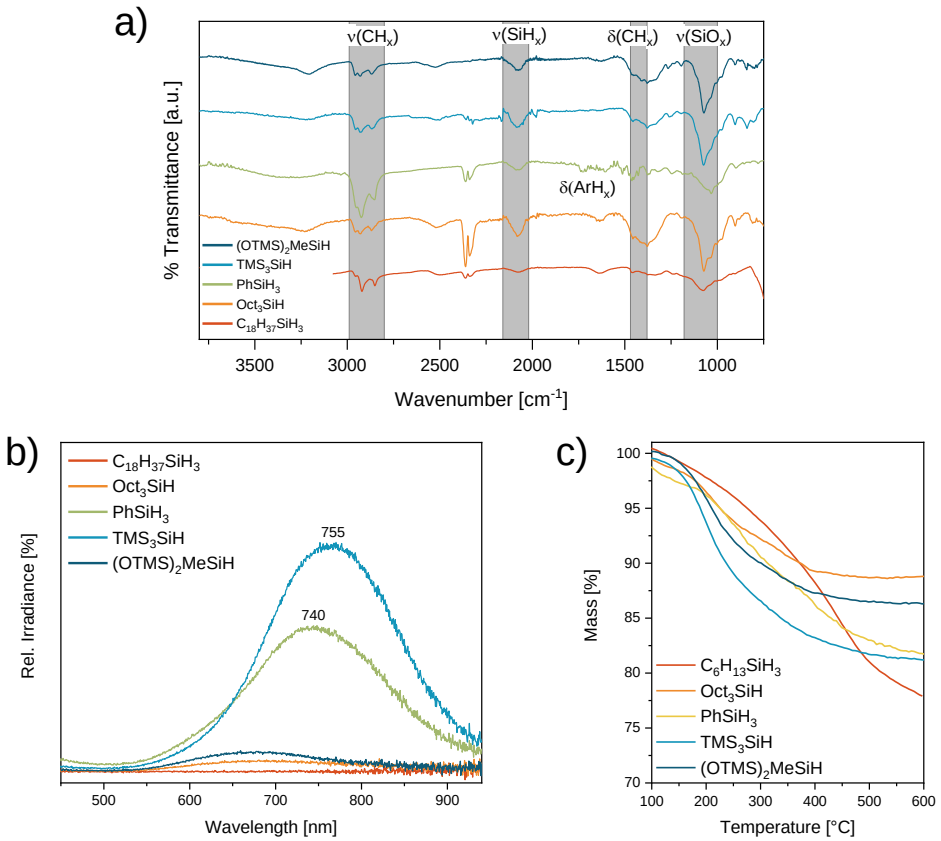


Figure 13: a) FT-IR spectra b) PL spectra c) TGA of SiNCs functionalized with different silanes *via* DHC with $BH_3$·THF.

Except for the phenyl silane and octadecyl silane-capped SiNCs, the reaction solutions remain opaque, which indicates incomplete surface functionalization. The FT-IR spectra of all samples in Figure 13a still show $SiO_x$ stretching bands revealing surface oxidation. Furthermore, aliphatic $CH_x$ stretching is observed for all SiNCs, as no such signal is expected for the phenylsilane-capped SiNCs. Residues of washing solvents like methanol probably cause these bands in the specific FT-IR spectrum.

Mass losses between 11 and 22% are determined by TGA for the different silanes (Figure 13c). Table 1 depicts the corresponding surface coverage calculated from the mass losses. Significant PL emissions are only observed for TMS-silane and phenylsilane (Figure 13b). The other samples are hardly dispersible in any organic solvent and settle fast why PL

measurements are hard to perform. Solubility of the SiNCs generally depends on the surface coverage and the electronic structure of the corresponding ligand. An undefined side reaction of silane and borane adduct could be responsible for the transparent and dark solutions. They are observed in blind reactions without silicon nanomaterials and will be investigated by NMR spectroscopy in the next chapter.

Table 1: Mass losses obtained by TGA and calculated surface coverages.

| silane | mass loss [%] | surface coverage [%] |
|---|---|---|
| $TMS_3SiH$ | 19 | 10 |
| $PhSiH_3$ | 19 | 22 |
| $Oct_3SiH$ | 11 | 3 |
| $OTMS_2MeSiH$ | 14 | 7 |
| $HexSiH_3$ | 22 | 25 |

#### 4.1.2.3. Lewis Acid Induced DHC with Silicon Nanosheets

To gain deeper insight into the capping mechanism during homonuclear DHC $^{1}H$ and $^{29}Si$-NMR experiments with SiNSs and hexyl silane are performed. Therefore, reactions of a) silane + LA, b) silane + LA + SiNSs, and c) SiNSs + silane are investigated. The two insets in Figure 14 show the respective reaction dispersion. The yellow suspension in the upper picture has turned brown after $BH_3$·THF is added. In contrast, the solution in the lower image is initiated thermally and stays yellow.

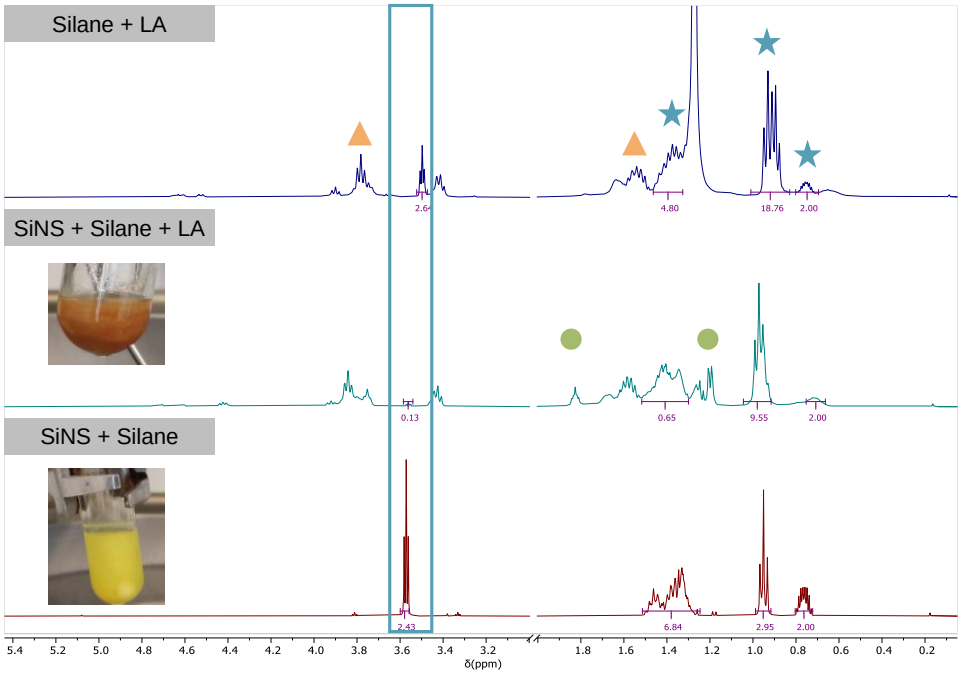


Figure 14: $^{1}H$-NMR spectra of test reactions with hexyl silane, SiNSs, and $BH_3$·THF. All experiments were performed at 100 °C. The blue stars mark the aliphatic backbone of the silane. Red triangles mark the signals of $BH_3$·THF, and green circles mark the new unidentified species.

According to the $^{1}H$-NMR spectrum in Figure 14, no silane is consumed upon thermal initiation without $BH_3$·THF. The blue box frames the proton signals of the silane group. The hexyl

backbone peaks (blue stars) integrals between 0.7 and 1.5 ppm are normalized to the two methylene protons in α-position to the silicon atom. The triplet signal at 3.6 ppm with an integral of 3 and *J* of 3.9 Hz is assigned to the silane protons. When $BH_3$·THF (red triangle) and pure silane are heated, the silane signal slightly shifts to lower fields (upper spectrum). Such a downfield shift is also observed in borosilylation products in literature.[178] It indicates that the borane activates the silane. Only mixing all three compounds decrease drastically the silane integral. However, unidentified signals of side products occur (green circles).

Experiments with $^{29}$Si-insensitive nuclei enhanced by polarization transfer (INEPT)-NMR spectroscopy in Figure 15 confirm the results of $^{1}$H-NMR. The peak of the hexyl silane remains unchanged after thermal initiation and lies at -60 ppm which is in accordance to literature.[179] In the presence of the LA and the SiNSs, three signals at -15, -17, and -21 ppm occur, while the original silane signal at -60 ppm diminished. The results indicate that only with LA and SiNSs an activation of the silane takes place.

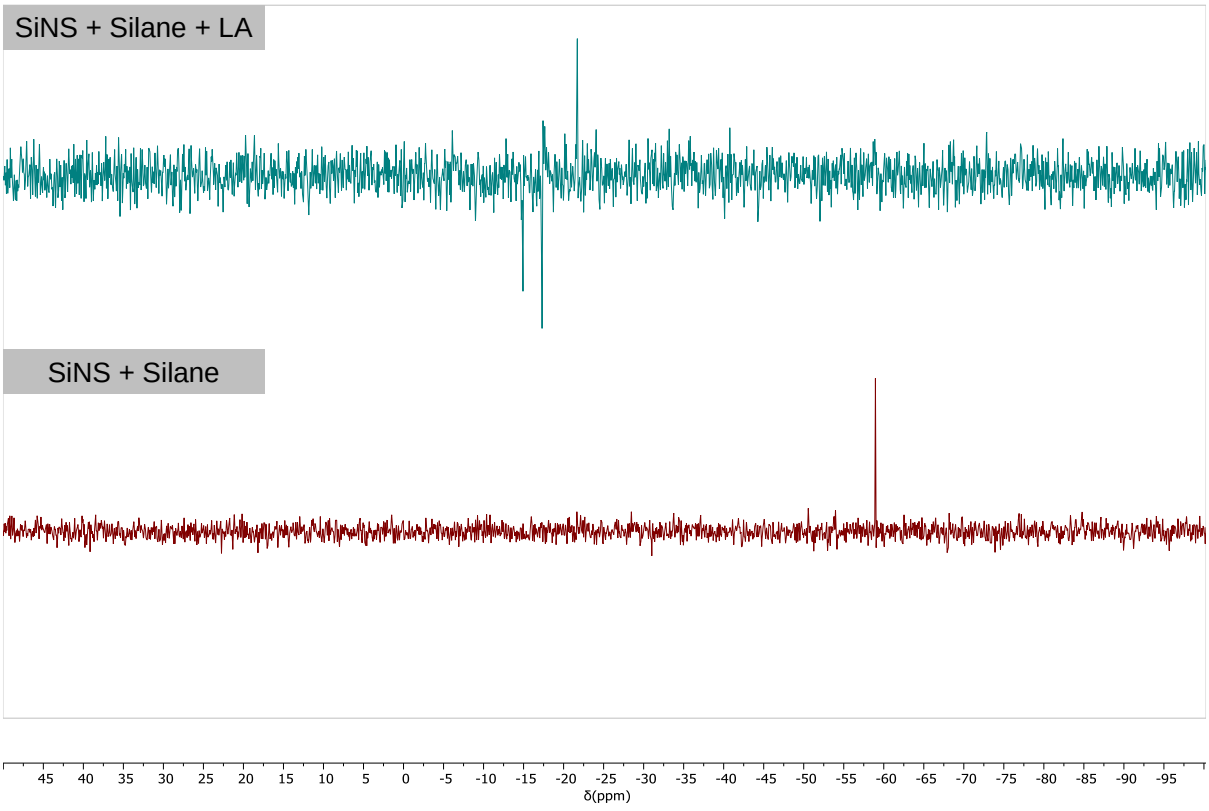


Figure 15: $^{29}$Si-INEPT-NMR spectra of the test reactions with SiNSs and silane.

The FT-IR spectra in Figure 16 indicate that both SiNSs DHC reactions investigated by NMR are not completely functionalized due to the high degree of oxidation shown by very intense bands assigned to $SiO_x$ stretching vibrations at 1100 $cm^{-1}$. Nonetheless, the LA-activated sample exhibits a higher amount of aliphatic group due to the $CH_x$ stretching vibration around 2900 $cm^{-1}$. That means, with LA-activated DHC, more capped silanes on the SiNS surface are observed.

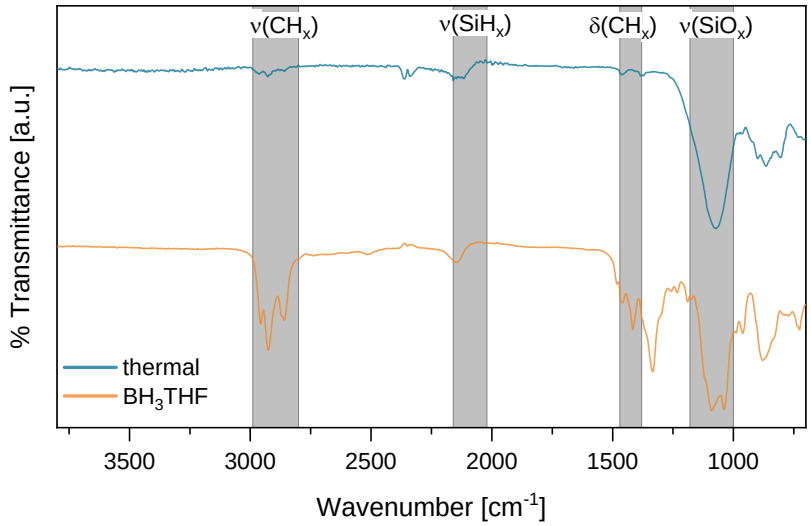


Figure 16: FT-IR spectra of DHC of SiNSs with hexyl silane induced thermally and by $BH_3$·THF.

### 4.1.3. Summary and Conclusion

In this project, SiNSs and SiNCs were coupled with silanes *via* DHC, aiming to enlarge the silicon nanomaterials' semiconducting system and investigate the impact on optical properties. The surface functionalization was incomplete with thermal and radical initiation, leading to oxidation. DHC reaction with Wilkinson's catalyst resulted in a loss of PL emission. In a new method, it was tried to induce DHC with different boron Lewis acids (LA).

The first screening of boron initiators found $BH_3$·THF as beneficial, while BCF did not activate DHC at all. TGA revealed that primary silanes reach a higher surface coverage compared to tertiary silanes. NMR spectroscopy with SiNSs and silane exhibited that reaction activation occurs only in the presence of LA. However, the activation of the Si-H bonds limited the homonuclear DHC of silanes with silicon nanomaterials. In conclusion, it resulted in vast material oxidation instead of surface passivation. A possible reason is that the activation with LAs did not polarize the Si-H bond sufficiently; consequently, the Si-Si bond formation failed.

In the literature, $BH_3$·THF seems efficient for activating silicon nanomaterials for surface functionalization *via* HS. DHC does not involve alkenes, unlike HS. The first activation of unsaturated substrates as a proposed mechanism was impossible for DHC. Future approaches to Si-H activation for a successful DHC may focus on frustrated Lewis pairs.[174]

## 4.2. Trityl-Induced Functionalization

### 4.2.1. Introduction

Surface functionalization of SiNCs with nucleophiles offers the possibility to obtain various silicon heteroatom bonds. Depending on the nucleophilic heteroatom, various properties of the functionalized SiNCs are expected. Apart from the particles' size, the PL emission is tuned additionally by surface groups. While hydrosilylation only results in Si-C bonds, nucleophilic attack offers a variety of silicon heteroatom bonds. Nucleophilic substrates are the key to form Si-Heteroatom bonds on the surface and tune PL emission through the visible spectrum.

Dasog *et al.* utilized ferrocenium oxidants to functionalize SiNCs with several nucleophiles, like amines, alcohols, carbon acids, thiols, and phosphines.[67] While the amine-capped nanoparticles emit blue light by charge transfer, SiNCs with Si-O and Si-S bonds lead to red PL due to suboxide defect states.[180,181] The high sensitivity of the oxidant requires the complete exclusion of water and oxygen, which renders surface functionalization of SiNCs a rather challenging task.

Here, a new functionalization method is described that activates freshly etched hydride-terminated SiNCs for nucleophilic attacks. Trityl salts abstract hydrides from the SiNCs leading to electrophilic silylium ions. Hence, the opportunity is offered to introduce new surface functionalities by subsequent application of appropriate nucleophiles. Therefore, it is a promising alternative when radical or thermal insertion of surface groups fail.

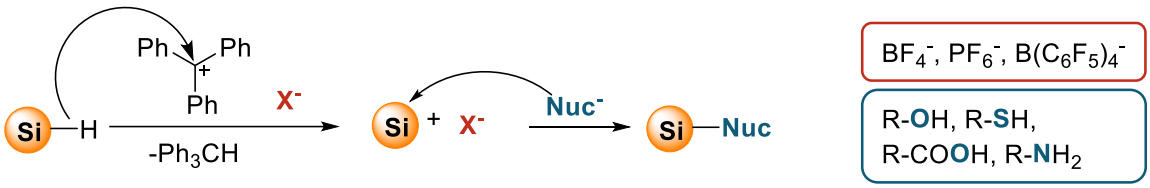


Scheme 13: Trityl-induced hydride abstraction from silicon nanocrystals.

Silylium cations are excellent electrophilic centers. In molecular silicon compounds, they are obtained through hydride abstraction by trityl salts. This so-called Bartlett-Condon-Schneider reaction is a silicon-to-carbon hydride transfer, first introduced in 1944.[182] Apart from the silylium ion, triphenylmethane is obtained as a byproduct. The highly reactive silylium ion causes several side reactions, like chloride abstraction or coordination, with solvents. Weakly coordinating and sterically demanding counterions are necessary to prevent reactions with solvents. Trityl salts were already used in catalytic amounts in the hydrosilylation of porous silicon combined with terminal alkenes and alkynes by Buriak *et al.* Therein, they only act initially as the reaction propagates by the carbocation in the *β*-silyl position.

Former approaches utilized halogenated SiNCs to couple nucleophiles on the silicon surface. Hazardous substances like $PCl_5$ or $Cl_2$ gas are necessary for this surface halogenation.[183,184]

Höhlein *et al.* bypassed the direct halogenation by hydrosilylation with chlorodimethyl-(vinyl)silane.[185] The subsequent reaction with alcohols and silanols led to the passivation of the surface groups. However, this procedure was rather tedious due to the two-step process of functionalization, which afforded time-consuming purification after every step.

This chapter describes a facile method for introducing various Si-Het bonds initiated by trityl salts to improve existing applications of silicon nanomaterials. The initial experiments exhibit the scope of possible substrates for alcohols and thiols. Later, the optimization of reaction parameters is described. Finally, the reaction mechanism is investigated, and fluorination of the SiNCs from the trityl salt anion is investigated.

## 4.2.2. Results and Discussion

### 4.2.2.1. Substrate screening

For initial experiments, different substrates with nucleophilic functional groups are applied. Figure 17a displays the FT-IR spectra of SiNCs capped with butanol, dodecanethiol, hexanoic acid, and octylamine under activation with triphenylmethyl hexafluorophosphate ($TrPF_6$).

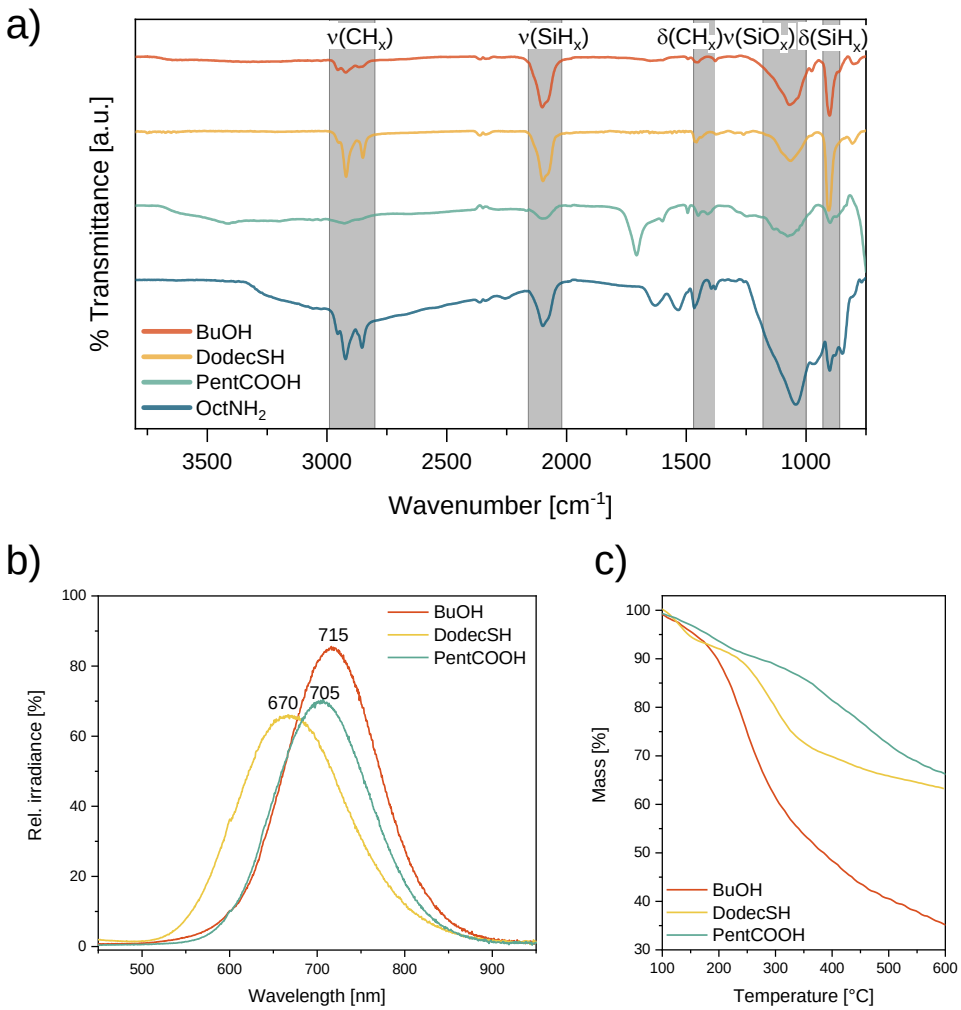


Figure 17: a) FT-IR b) PL c) TGA characterization of the SiNCs capped with butanol, dodecanethiol, hexanoic acid, and octylamine under activation with $TrPF_6$.

The $SiO_x$ stretching signal at 1050 $cm^{-1}$, $SiH_x$ stretching at 2100 $cm^{-1}$, and aliphatic $CH_x$ stretching around 2900 $cm^{-1}$ are visible. The butanol and dodecanethiol-capped SiNCs exhibit signals according to literature, and -OH or -SH signals are absent.[66,186] The hexanoic acid-capped SiNCs show a very weak aliphatic $CH_x$ stretching, and at 1700 $cm^{-1}$, the C=O stretching of the carbonyl group is observed.

The functionalization with octylamine failed due to a high amount of oxidation, identified by the strong $SiO_x$ stretching signal at 1050 $cm^{-1}$ and the brighter color of the treated SiNCs. The octylamine-capped SiNCs were not luminescent, but the other samples' PL emission spectra were recorded (Figure 17b). Butanol and hexanoic acid-capped SiNCs show an emission maximum of 715 nm and 705 nm. In comparison, the dodecanethiol-capped SiNCs are slightly blue-shifted to 670 nm since another etching batch was used.

The surface coverage is determined by TGA analysis, shown in Figure 17c. The hexanoic acid-capped SiNCs exhibit the lowest mass loss, consistent with the weak aliphatic signal in the FT-IR. Both results indicate that capping with carboxylic acids was not efficient. The second sample, the dodecanethiol-capped SiNCs, decomposes in two steps. While the first mass loss occurs at ~150 °C, the second and main mass loss takes place at ~300 °C. The highest mass loss is observed for the SiNCs covered with butanol, which is not surprising since the driving force is the formation of the strong Si-O bond on the SiNC surface.

Besides these substrates, also $KSiTMS_3$ is tested to obtain an alternative route for DHC (Figure 18c). Trityl salts activation, in combination with organolithium reagents (OLR) and carbon nucleophiles, is anticipated to enhance surface coverage. The conventional approach theoretically achieves a maximum surface coverage of 50%, whereas the trityl-induced functionalization enables the capping of each surface Si atom with a nucleophile.

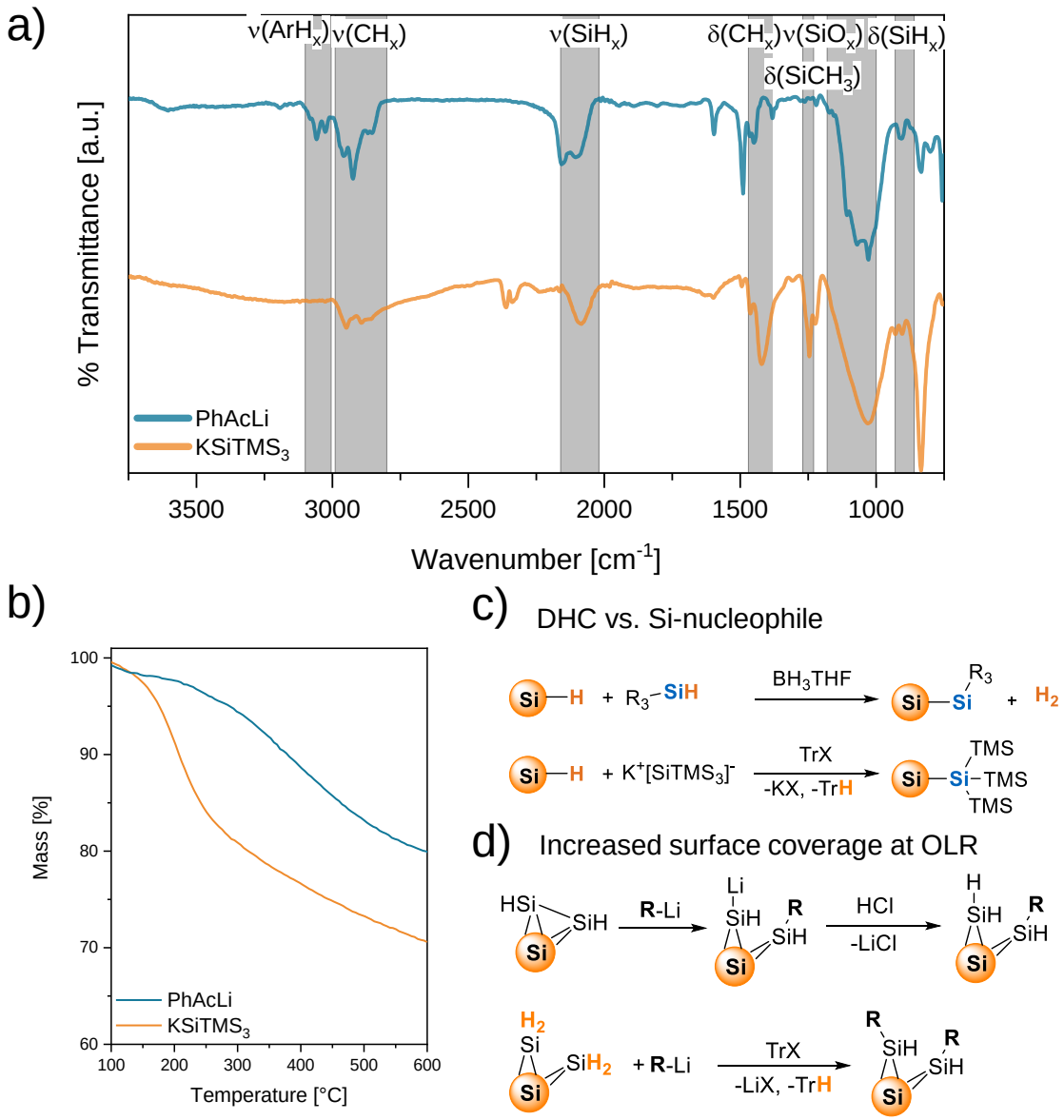


Figure 18: Group IV elements as nucleophiles. a) FT-IR spectra b) TGA of SiNCs capped with a substrate. c) Scheme of alternative reaction routes.

The FT-IR spectrum in Figure 18a shows the expected signals for the PhAcLi -capped SiNCs. Besides the aromatic $CH_x$ stretching for the phenyl group at 3100 $cm^{-1}$, some aliphatic solvent residues at 2900 $cm^{-1}$ are present. TGA analysis of OLR-capped SiNCs reveals a relative mass loss of 20%. Although lower than the theoretical value of 50%, the result is higher than the literature values obtained without trityl activation.[187] The result indicates that the trityl activation increases the surface coverage but not to the expected extent. The capping with $KSiTMS_3$ shows the Si-$CH_3$ stretching of the TMS groups in the FT-IR spectrum at 1250 $cm^{-1}$. The surface coverage of 17% determined by TGA analysis is comparable to the DHC silane samples. Both samples exhibit a strong $SiO_x$ signal in the FT-IR at 1050 $cm^{-1}$, indicating the oxidation of the SiNCs consistent with the observation that the SiNC solutions are not luminescent. In conclusion, these Si- and C-nucleophiles are unsuitable for trityl-induced functionalization. Furthermore, as already explained in the previous section, carboxylic acid

derivatives to low surface coverages. The first capping experiments with amines lead to a high amount of oxidation. A small amount of silicon oxide and silicon oxynitride moieties is known for reaction of SiNCs with nitrogen containing compounds, which is claimed to cause a blue photoluminescence.[188] It remains an interesting surface group because of its unique optical properties.[181] Therefore, the following experiments will only focus on alcohols and thiols as nucleophiles.

#### 4.2.2.2. Optimization of parameters

The previous chapter explored the first possibilities of this functionalization method. Now, optimization of the reaction parameters is necessary to achieve the best properties of the functionalized SiNCs. Figure 19 shows the characterization of SiNCs capped with alcohols of different chain lengths under activation with TrBCF. All FT-IR spectra exhibit $SiH_x$ stretching at 2100 $cm^{-1}$ and $SiO_x$ stretching around 1100 $cm^{-1}$. The latter signal band includes the Si-O-C stretching from the alcohol surface group.[189]

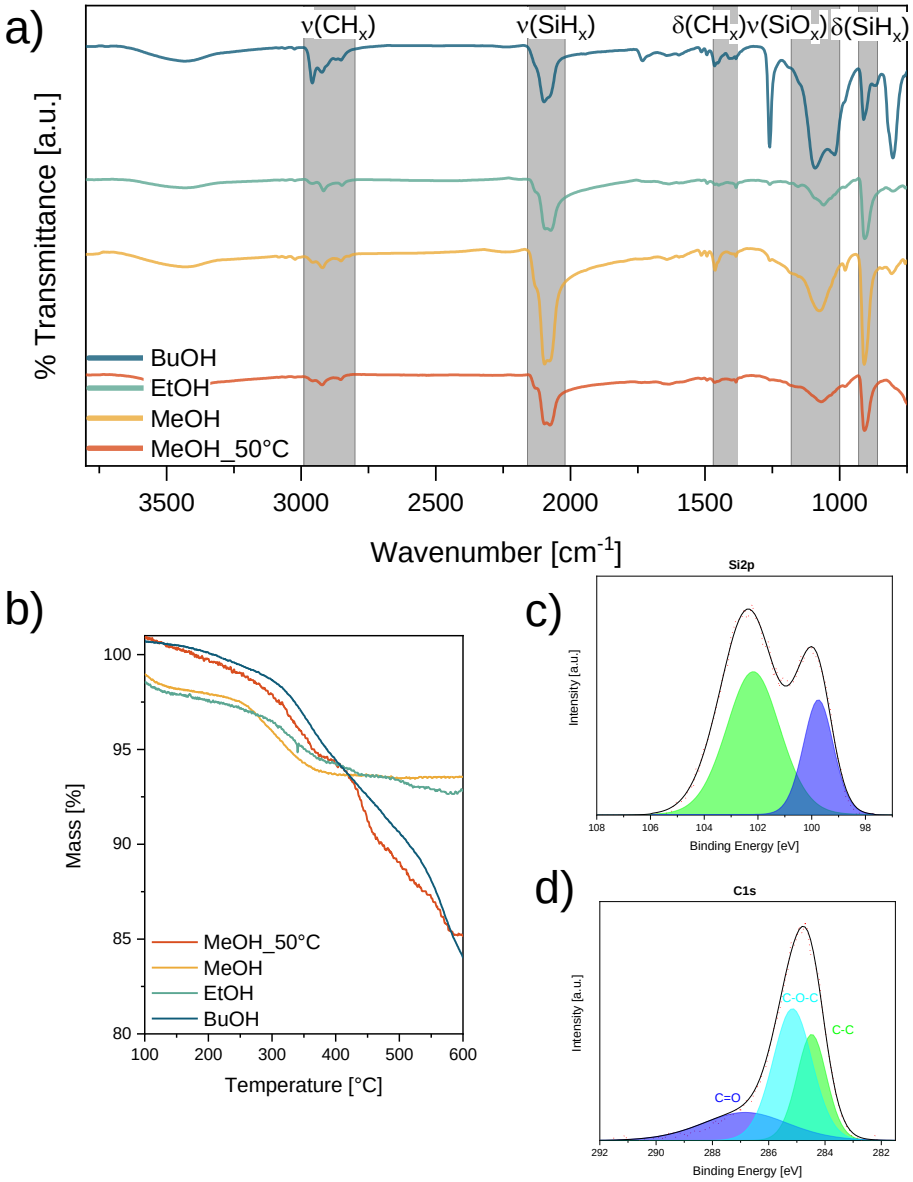


Figure 19: a) FT-IR spectra b) TGA of SiNCs capped with alcohols of different chain lengths. The reaction temperature is varied for methanol. XP spectrum of c) Si2p and d) C1s of butanol-capped SiNCs.

TGA analysis reveals that the highest surface coverage of 54% is achieved by capping with MeOH at 50°C. Functionalization with alcohols at room temperature leads to significantly decreased surface coverages of around 20%. XPS analysis of the butanol-capped SiNCs exhibited that the SiNCs contain Si(0) besides higher oxidation states indicating that the SiNCs are not completely oxidized. The high-resolution C1s spectrum in Figure 19d shows that the sample includes C-C and C-O bonds from the capped alcohol. Generally, the trityl-induced capping with alcohols works well. With increasing side chain length, enhanced solubility in organic solvents is observed. The results also show that higher reaction temperatures achieve higher surface coverages.

Although the first capping experiment with amines led to oxidation, one secondary ($Oct_2NH$) and primary ($PrNH_2$) amine were compared in their capping ability. 9 nm SiNCs were used because they are less prone to oxidation than smaller SiNCs. The capping with propylamine

worked successfully according to the XP spectrum in Figure 20a. Surprisingly, the more nucleophilic $Oct_2NH$ could not be attached to the SiNC surface, as the XP spectrum in Figure 20b depicts only the baseline. Hence, it is most likely explained by the higher steric demand of the secondary amine substrate than the primary amine.

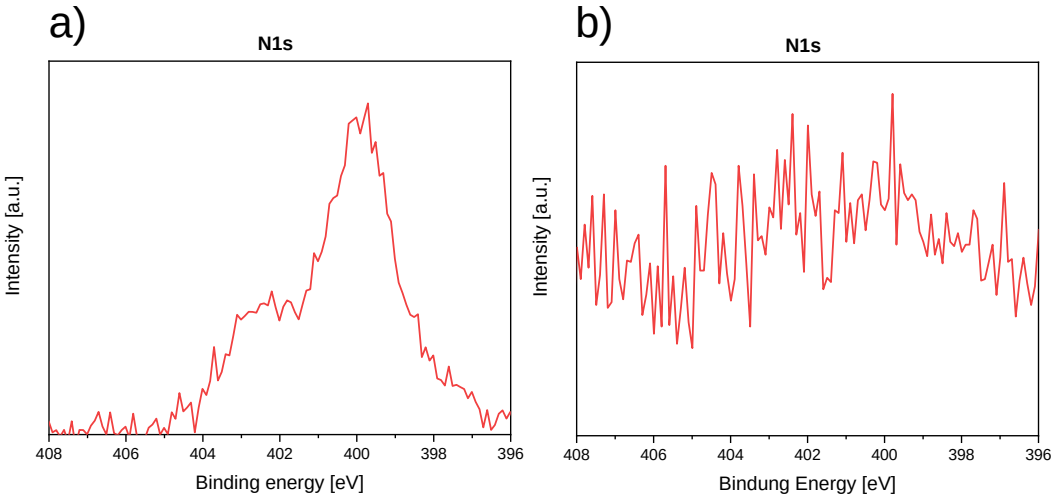


Figure 20: XP spectra of 9 nm SiNCs after capping with a) $PrNH_2$ b) $Oct_2NH$ under activation with TrBCF.

The variation of the trityl salt anions at functionalization with DodecSH shows quite significant differences. Two commercially available trityl salts, TrBF4 and TrPF6, were used for comparison. Further, the synthesized TrBCF with the sterically demanding and weakly coordinating $B(C_6F_5)_3$-anion was tested. Figure 21a depicts the different FT-IR spectra. The poor solubility of $TrPF_6$ in acetonitrile caused residues of the trityl salt in the sample after workup visible in the FT-IR around 3100 $cm^{-1}$.

All experiments are performed in DCM, where all three trityl salts are soluble, but $TrPF_6$ is the least. The solubility of $TrPF_6$ also causes a lower reactivity in the functionalization process in the reaction solvent. TGA indicates with the high mass loss at relatively low temperatures in (Figure 21b) that adsorption of thiol on the surface but no covalent functionalization took place. The least intense $SiH_x$ stretching signal is observed under activation with $TrBF_4$, consistent with the high and late mass loss in the TGA, thus indicating a successful covalent surface capping. The TGA onset point lies significantly over the boiling point of 275 °C, and adsorption of dodecanethiol can be excluded.[190] The activation results with TrBCF lie between the two commercially available trityl salts. The $SiO_x$ stretching signal in the FT-IR is very weak because the commercial trityl salts can contain impurities of TrOH, which oxidizes the SiNCs. Finally, activation with $TrBF_4$ leads to the highest surface coverage, while TrBCF causes the lowest surface oxidation. One could assume that fluorination of the SiNC surface with $TrBF_4$ is the reason, discussed in chapter 4.2.2.3.

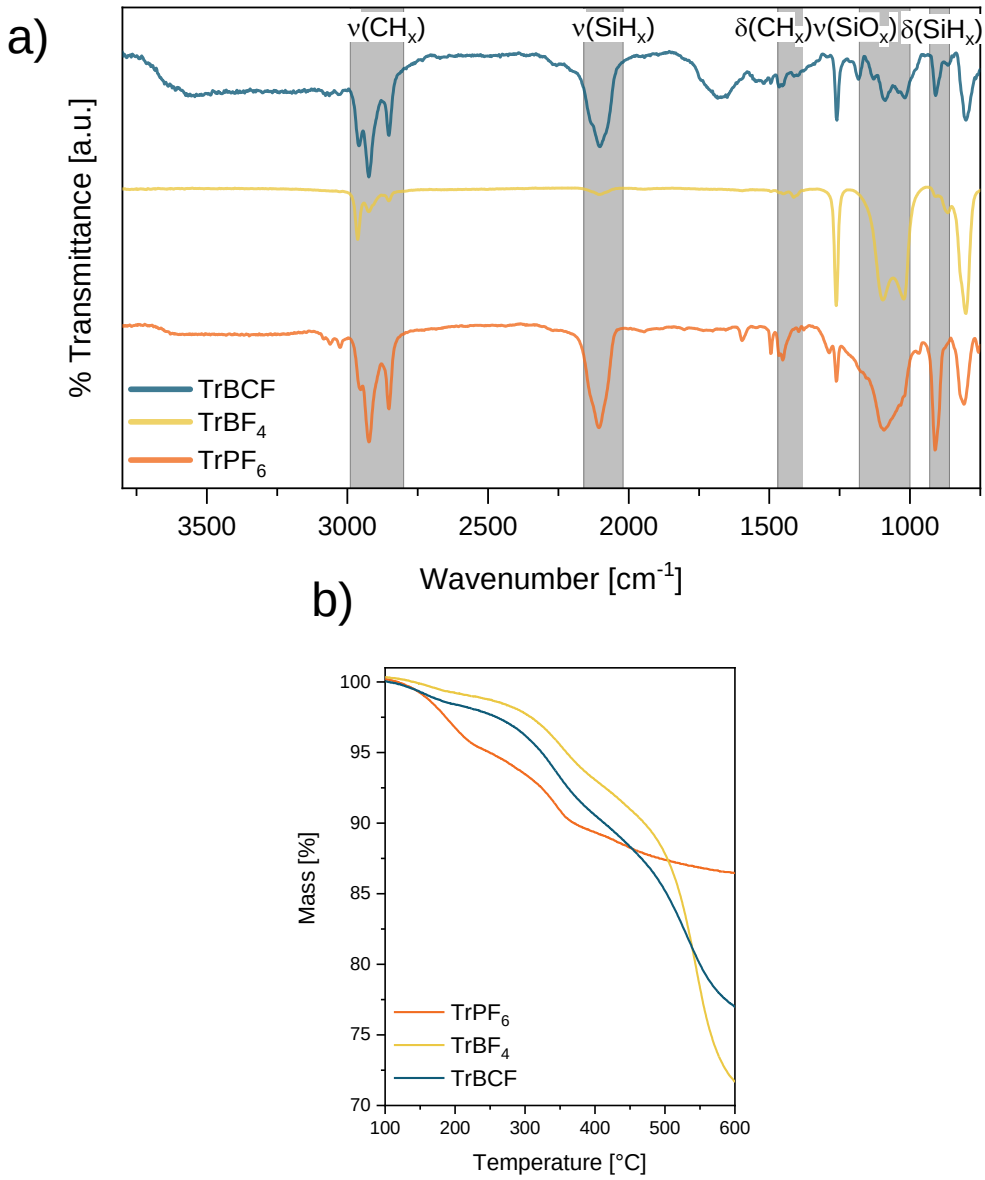


Figure 21: a) FT-IR b) TGA of 9 nm SiNCs capped with DodecSH under activation of TrBCF, $TrBF_4$, and $TrPF_6$.

NMR experiments are conducted with dispersible 3 nm SiNCs capped with DodecSH and different trityl salts. Figure 22 shows the NMR spectra of pure DodecSH and the capped SiNCs after activation with $TrBF_4$ and $TrPF_6$, as well as a control experiment without adding trityl salts to the reaction mixture. The integrals are normalized to the terminal methyl group of DodecSH (t, 0.88 ppm, 3H). The methylene group in α-position to the thiol group (q, 1.60 ppm, 2H) gets shifted and split into three signals in combination with SiNCs. This shift and the splitting of the C$H_2$SH protons at 2.5 ppm reveal that the surrounding of the thiol proton changes or even deprotonation takes place. The blind reaction exhibits the highest integral of the original C$H_2$SH signal, which indicates that the functionalization is less efficient without trityl activation.

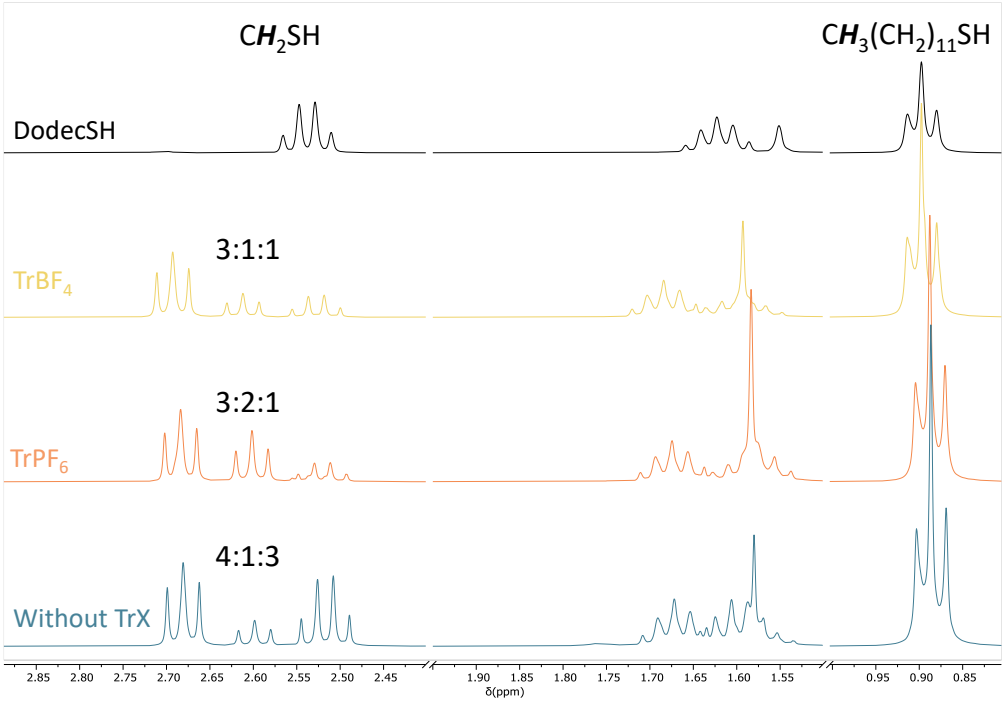


Figure 22: $^{1}$H-NMR spectra of DodecSH and DodecSH capped SiNCs initiated by different trityl salts and the blind reaction.

After varying the trityl salt anion, the reaction solvent is chosen based on the solubility of the initiators. $TrBF_4$ and TrBCF are soluble in polar solvents like acetonitrile, dichloromethane, and chloroform. Additionally, TrBCF dissolves in aromatic non-polar solvents like benzene or toluene, where it forms two phases because of a π-complex. Since both trityl salts are soluble in in the low boiling dichloromethane, this is further used as functionalization solvent.

In THF, cationic ring-opening polymerization takes place when trityl salts are present. Also, Helbich *et al.* investigated the ROP of THF in a combination of SiNSs with iodonium salts in the dark.[49] Figure 23a shows a photo of the crude solutions according to the entries in the table. While the pure silicon nanomaterials in THF do not polymerize, with the trityl salts TrBCF and $TrPF_6$, a dark and slightly viscous solution is observed. A highly viscous material is formed in combination with etched SiNCs and TrBCF (entry 6). However, with $TrBF_4$, no polymerization with and without SiNCs took place. The presence of polyTHF in the other experiments is confirmed by $^{1}$H-NMR in Figure 23b, which depicts exemplary signals of THF and polyTHF. Overall, the highest integral ratio was obtained by adding SiNCs to TrBCF, which led to an enhanced polymerization of THF.

a)

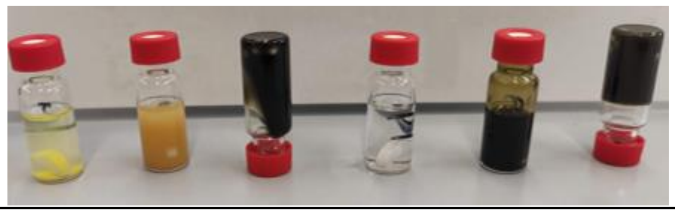

| entry | 1 | 2 | 3 | 4 | 5 | 6 | 7 |
|---|---|---|---|---|---|---|---|
| **SiNM** | SiNS | SiNC | - | - | | SiNC | SiNC |
| **Trityl salt** | | | TrBCF | $TrBF_4$ | $TrPF_6$ | TrBCF | $TrBF_4$ |
| **Integral ratio (pTHF/THF)** | 0 | 0 | 0.29 | 0 | 0.27 | 0.39 | 0 |

b)

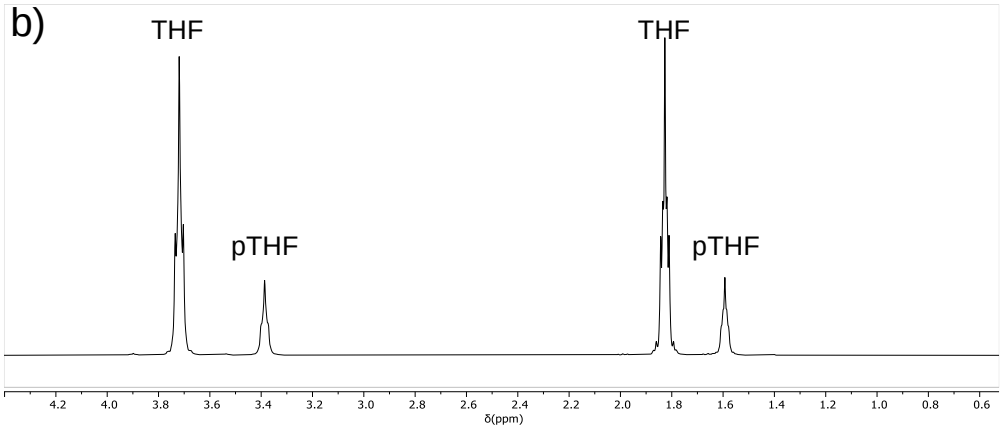


Figure 23 a) Table of THF polymerization experiments with pictures of the respective entries b) $^{1}$H-NMR spectrum of entry 5.

After all the optimization steps, different SiNC sizes are tested under the investigated conditions. Figure 24a depicts the FT-IR of 9 and 20 nm SiNCs capped with propylamine or DodecSH. At the capping with propylamine surface, oxidation of the 20 nm SiNCs is still observable ($SiO_x$ stretching at 1150 $cm^{-1}$).

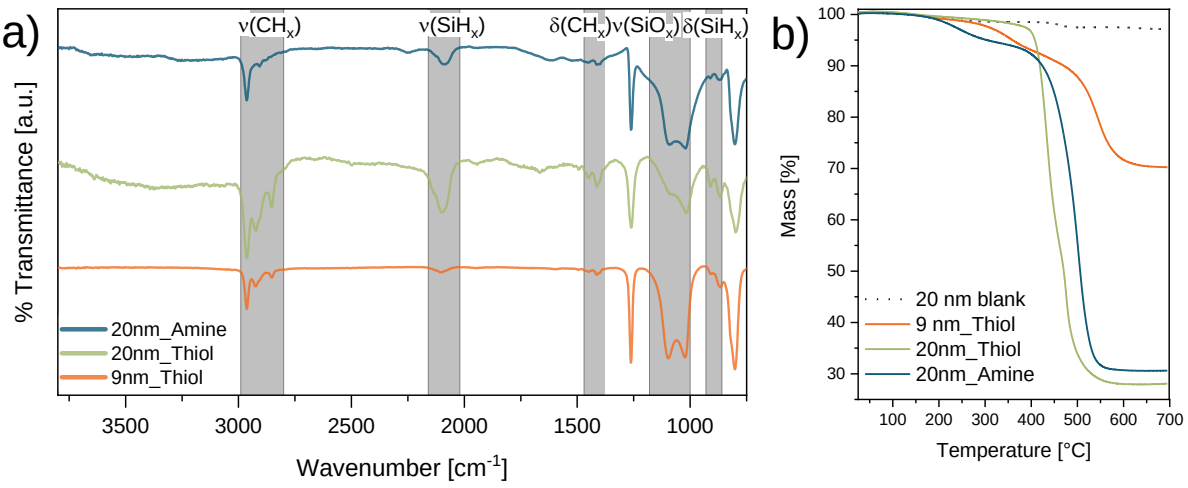


Figure 24: a) FT-IR b) TGA of 9 nm and 20 nm SiNCs capped with propylamine or DodecSH under activation of $TrBF_4$. The dotted line shows the etched and unfunctionalized 20 nm SiNCs.

It is assumed that silicon oxynitrides are formed, which could be identified with XPS.[191] The capping of thiol is comparable for the two SiNC sizes in the FT-IR. Both graphs show the characteristic aliphatic $CH_x$ signal around 2900 $cm^{-1}$. The 9 nm SiNCs are slightly more oxidized than the 20 nm ones, as indicated by the weaker SiHx stretching and stronger SiOx bands. All three samples contained residues of acetonitrile at 1250 $cm^{-1}$.

TGA reveals significantly higher mass losses for 20 nm SiNCs than the 9 nm SiNCs (Figure 24b). This result is independent of the capping substrate and contrary to the lower volume-to-surface ratio of the larger particles. A blank TGA measurement of etched and freeze-dried 20 nm SiNCs confirms that the capping substrate caused the high mass loss. The high onset temperature of the primary decomposition step can exclude the impact of solvent residues.

#### 4.2.2.3. Mechanistic insights into the hydride abstraction with $TrBF_4$

To gain more knowledge about the functionalization method, experiments to discover the mechanism were performed. The reaction mechanism of the trityl-induced functionalization is based on the hypothesis of silylium ion formation as an intermediate state. $^{29}$Si solid-state NMR measurements were performed with SiNSs activated with $TrBF_4$. Due to the high amount of substance applied in solid-state NMR spectroscopy, especially for low abundant and insensitive $^{29}$Si nuclei, SiNSs instead of SiNCs were used. Silylium ions appear between +80 and +120 ppm, depending on the environment.[192] Unfortunately, such a signal was not observable in the NMR. Figure 25 compares the cross-polarization magic spinning (CPMAS) experiment, which shows the surface of the SiNSs, with the high-power-decoupling (hdpec) method, which investigates the bulk of the material. Both spectra do not depict the expected silylium signal in the grey area. Either the intermediate is short-lived, or another reaction pathway, for example, *via* a radical intermediate, takes place.

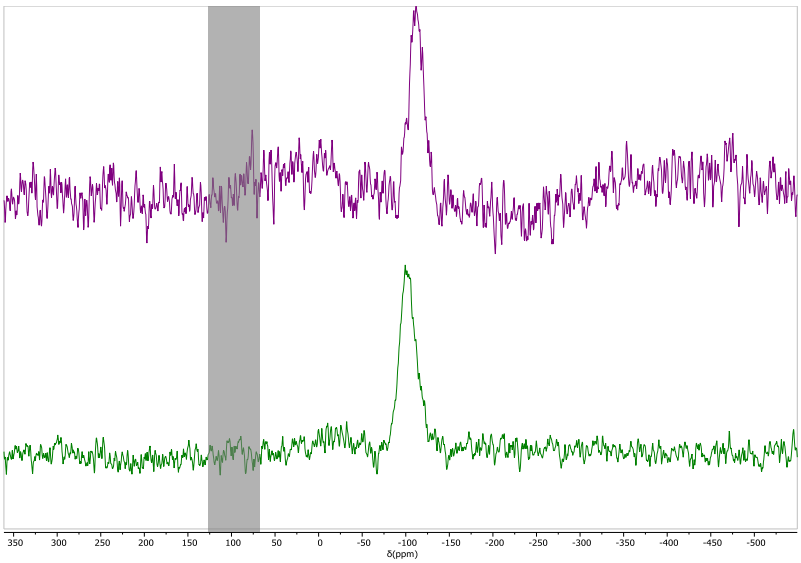


Figure 25: Solid-state NMR ($^{29}$Si CPMAS and hpdec) of SiNSs activated with $TrBF_4$. The grey box shows the signal range for the expected siliylium ions.

If silylium ions are present, the Lewis acidity of the compound increases. The Gutmann-Beckett method is a facile experiment to determine the Lewis acidity of silylium species.[193,194] Therein, a stoichiometric amount of $Et_3PO$ is added to the substrate under investigation. The difference in the chemical shift of the phosphine oxide in $^{31}$P-NMR is defined as the acceptor number. Trityl cations are also Lewis acidic due to the carbenium ion. However, silylium ions are much more Lewis acidic, so they are called Lewis superacids. However, silylium ions are much more Lewis acids, which is why they are also called Lewis superacids.

For this reason, pure trityl salts and etched SiNCs are investigated, besides activated SiNSs and SiNCs. Figure 26 depicts the $^{31}$P-NMR spectra of the different species tested. A significant shift of +28 and +22.5 ppm is observed for the pure trityl salts. This means that the trityl salts alone are already Lewis acidic. The silicon nanomaterials are activated by the trityl salt and separated from the initiator before the $Et_3PO$ is added. The SiNCs shift the phosphine oxide signal further (+5.2 ppm) than the SiNSs, indicating a higher Lewis acidity. However, both acceptor numbers are significantly lower than those of the trityl salts. This suggests that most silylium moieties are absent when $Et_3PO$ is added.

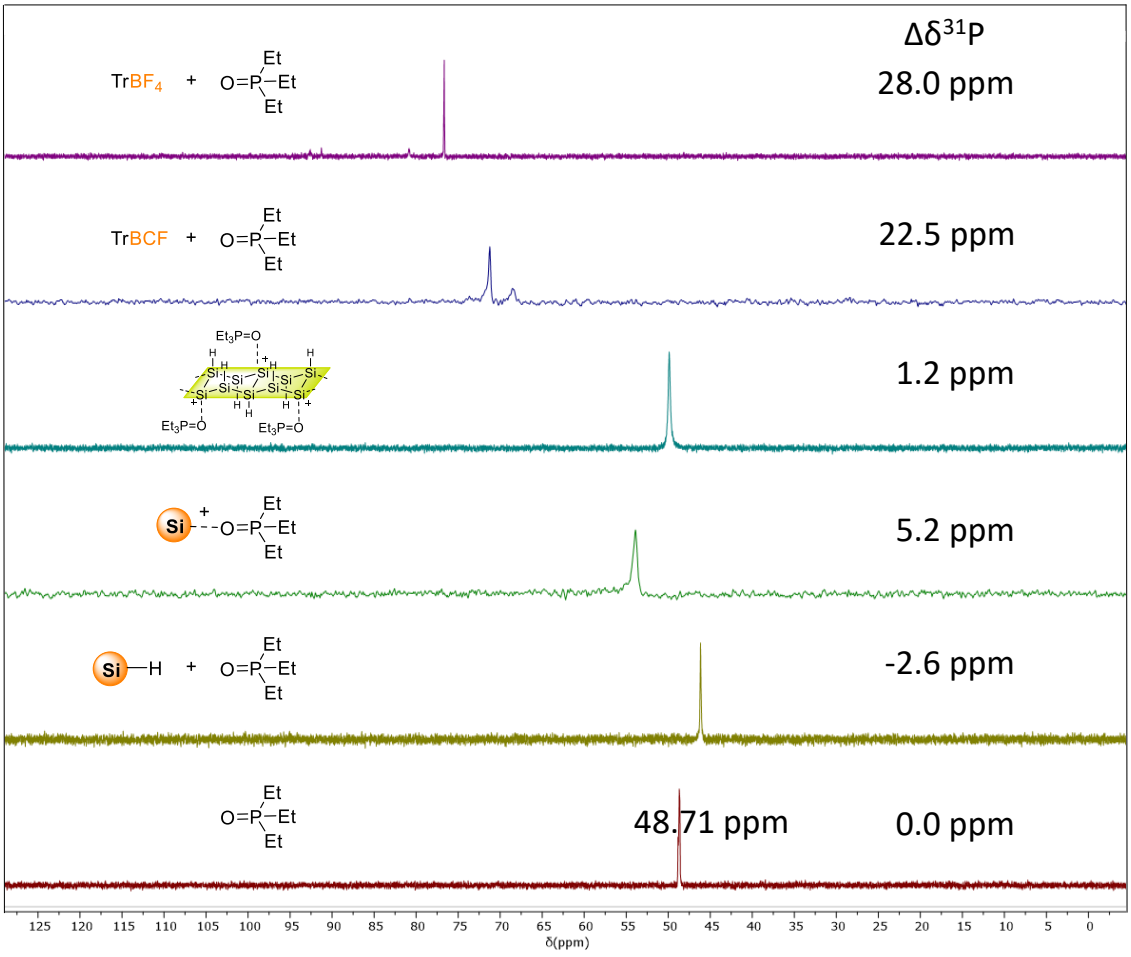


Figure 26: $^{31}$P-NMR of different species and the difference between the chemical shifts of the phosphine oxide signal.

In conclusion, both NMR experiments suggest that free silylium ions do not exist on the silicon nanomaterials' surface. Therefore, another reaction route of the trityl salt must be considered.

It is observed that after adding the $TrBF_4$ in DCM, the solution turns clear, as depicted in Figure 27a. It is assumed that after the hydride transfer, the highly electrophilic silylium moiety reacts with the $BF_4^-$ anion (Figure 27b). The formation of the strongest Si-heteroatom bond, the Si-F bond, is favored. The measurements in an inert gas atmosphere demonstrate a reproducible zeta potential of 0 mV (Figure 27d). Moreover, the dynamic light scattering (DLS) measurements of hydrodynamic radii before and after the zeta potential measurements verify that the SiNCs are neither agglomerated nor outside the standard size range. This indicates that no residues of trityl salt or other particles are present to disturb the measurement. Synthesis routes to solely fluorinated SiNCs are rarely known in the literature.[195] The material is only the subject of computational studies.[196,197] An interesting observation is that the solution turns opaque after exposition to ambient conditions. Figure 27e depicts the optical properties of the solution. It shows only PL emission after exposure to air; otherwise, just the excitation signal is visible. The emission maximum lies slightly blue-shifted to functionalized SiNCs of the same batch, indicating surface oxidation. The grey-filled spectrum shows the absorbance in the UV/Vis region, which is assigned to the dissolved unreacted $TrBF_4$ and fits literature values.[198]

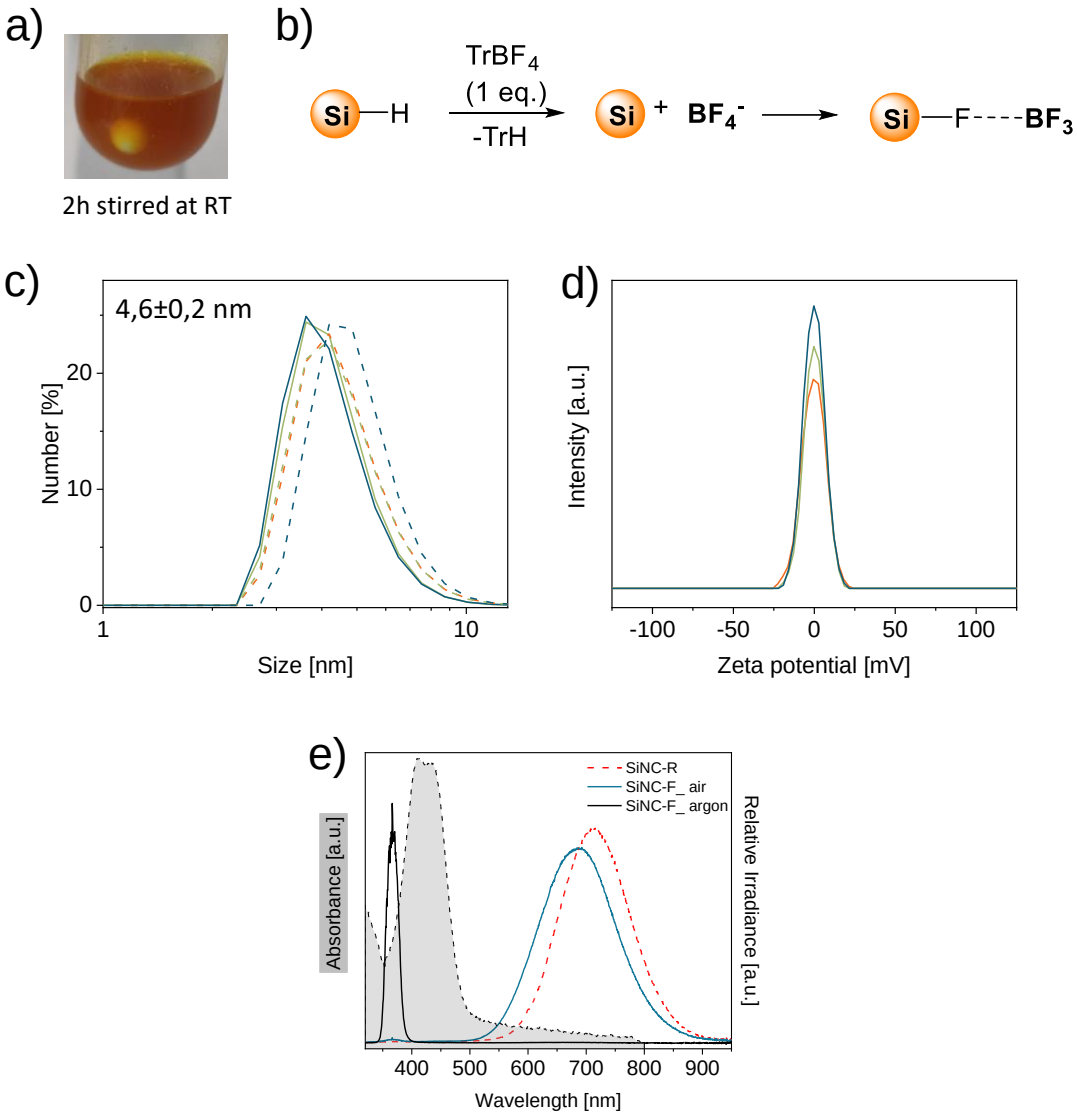


Figure 27: Properties and characterization of SiNCs activated with $TrBF_4$. a) Photograph of the reaction solution. b) Proposed reaction scheme. c) DLS measurements d) ζ-Potential measurement exhibiting no surface charge. e) UV/Vis and PL spectra with comparison to alkyl-capped SiNCs.

$^{19}$F-NMR experiments were conducted to investigate the fluorinated SiNCs further. Figure 28 compares the activation of SiNCs with two trityl salts at -35 °C and room temperature. The activation with TrBCF shows only signals of the salt anion. The defluorination of a C-F bond attached to an aromatic system is not favored. Also, the sterically demanding anion could shield the formed silylium ion to prevent side reactions.

Contrary to that, activation with $TrBF_4$ exhibits no reaction under cold conditions. At room temperature, unidentified signals between -130 and -146 ppm appear. Also, the J-coupling constant of Si and F identifies $SiF_4$. Gaseous $SiF_4$ is also observed in the silicon nanomaterials etching process with HF when $SiF_3$ surface moieties react with another fluoride ion. That means the fluorination of the SiNCs by $TrBF_4$ does not afford specific surface functionalization.

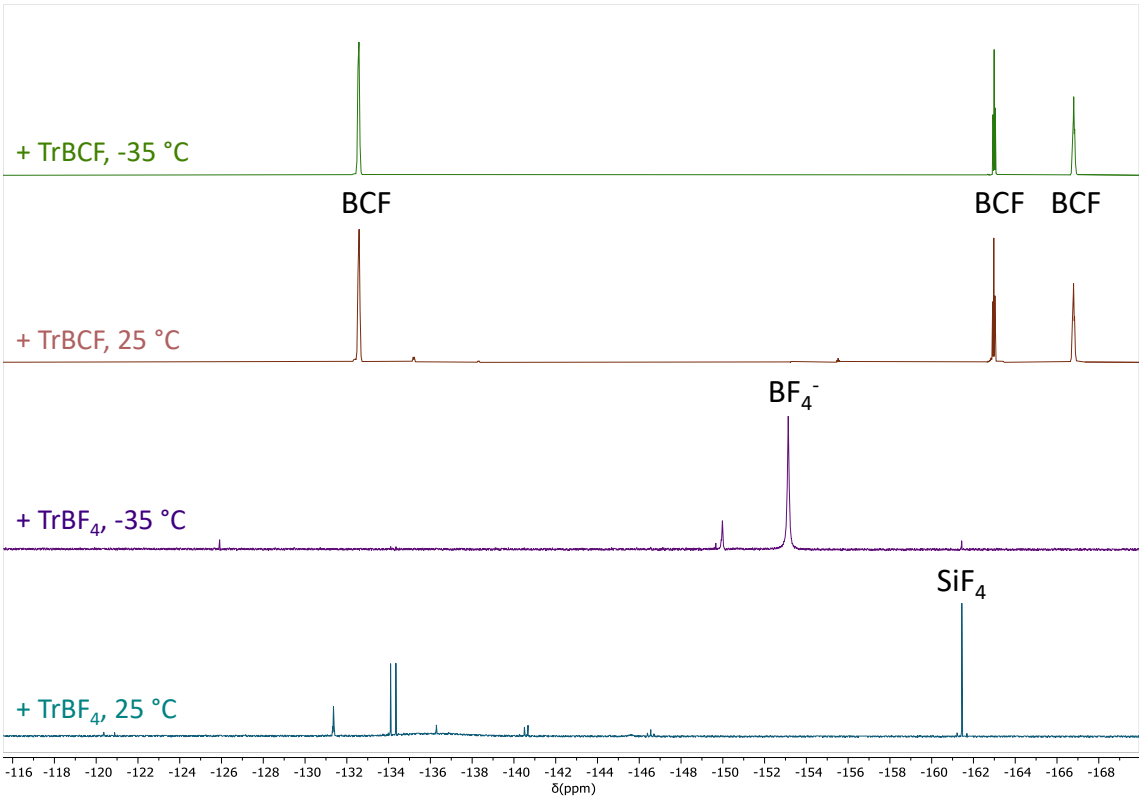


Figure 28: $^{19}$F-NMR spectra of SiNCs activated at -35 °C or room temperature with TrBCF or $TrBF_4$.

Molecular model substrates for surface groups are chosen to prove this hypothesis. Figure 29 depicts surface groups of etched SiNCs. They are categorized into hydride-termination, fluoride-termination, and siloxane bridges. The hydride-terminated surface units connected to the silicon network of the SiNC core *via* Si-Si bonds are mimicked by tris(trimethylsilyl)silane. The tetramethyl disiloxane acts as a model substrate for the siloxane bridges. In both cases, the most exciting question is whether Si-Si bond cleavage occurs with trityl activation.

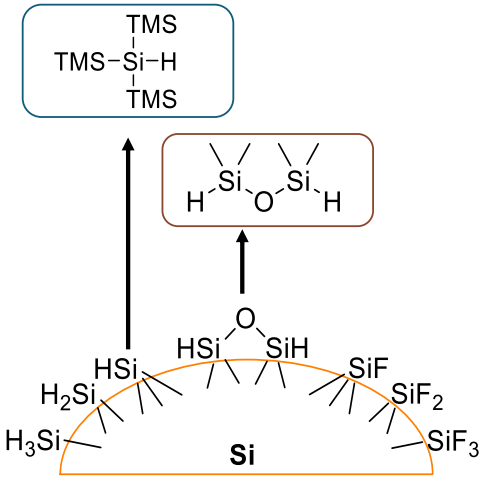


Figure 29: Overview of possible SiNC surface groups and the respective model substrate.

For $^{19}$F-NMR spectroscopy experiments, the model substrates were mixed with stoichiometric amounts of $TrBF_4$ in $CDCl_3$. Upon addition of the molecular model compounds, the yellow color of the solution of $TrBF_4$ immediately fainted, indicating a complete conversion of the trityl salt. The spectra with the assigned products are depicted in Figure 30.

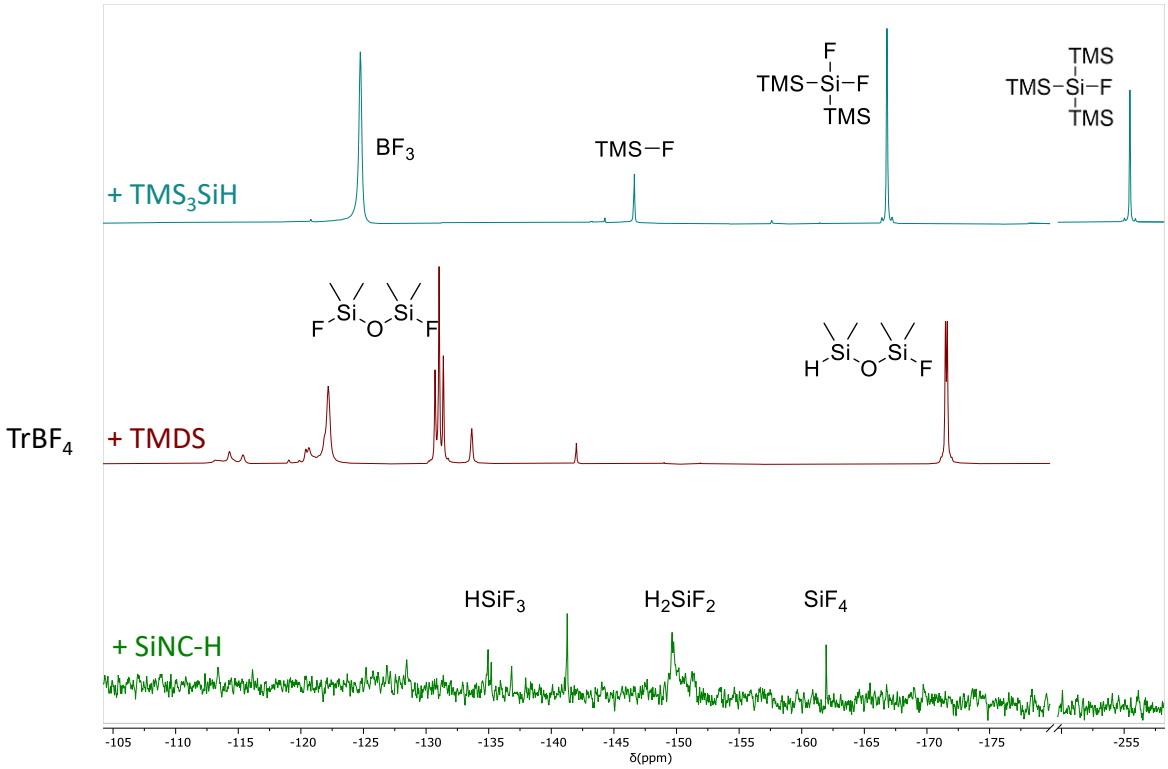


Figure 30: $^{19}$F-NMR of model substrates and SiNCs activated by $TrBF_4$.

At $TMS_3SiH$, the monofluorinated product is identified by coupling with the Si satellites.[53] The presence of tris(trimethylsilyl) fluoride is obtained. That indicates the Si-Si bond cleavage and complete fluorination of the unfunctionalized Si atoms. For the disiloxane, no Si-O bond cleavage is observed. The main products are the mono-and di-fluorinated siloxanes, as identified by multiplicity and coupling constants. This leads to the assumption that trityl activation cannot remove bridged surface siloxanes.[199] The lowest $^{19}$F-NMR spectrum depicts the clear crude solution of activated SiNCs. It indicates that besides $SiF_4$ and $HSiF_3$, other silicon hydride fluorides can be observed after trityl activation.

### 4.2.3. Summary and Conclusion

A new functionalization approach was described for SiNCs activated by trityl salts and subsequently functionalized with various nucleophiles. It was expected to insert a variety of heteroatom bonds on the SiNC surface, resulting in enhanced material properties, especially different emission colors. Substrate screening revealed that thiols and alcohols were suitable for this functionalization, as confirmed by FT-IR and TGA. Optimizing the reaction parameters led to up to 54% surface coverages for 3 nm SiNCs. Amines also worked as a capping substrate for larger SiNCs, which were less prone to oxidation. However, the expected blue luminescence was not observed. Comparing SiNCs capped with primary or secondary amines by XPS showed that nucleophilicity and the steric demand of nucleophiles influenced the capping success. A size-dependent efficiency of the functionalization was observed as 20 nm

SiNCs exhibited higher surface coverages at a lower volume-to-surface ratio than smaller SiNCs.

Activation with $TrBF_4$ or $TrPF_6$ in the absence of a nucleophile resulted in the fluorination of SiNCs, which was confirmed by DLS and a neutral zeta potential (no surface charge). These SiNCs showed unique optical properties, as they were completely soluble in organic solvents and exhibited no photoluminescence unless brought to ambient conditions. Contrary to the initial hypothesis, silylium ions were not obtained as intermediate. Molecular models mimicking surface groups revealed the formation of $SiF_4$ and unwanted Si-Si bond cleavage *via* $^{19}F$ and $^{29}Si$-NMR spectroscopy.

In summary, the studied trityl activation extends the fluorination and etching methods for silicon nanomaterials, even if it is unselective. Further optimization of this reaction may lead to applying fluorinated SiNCs as substrates for $^{19}F$ magnetic resonance bioimaging.

## 4.3. Janus SiNC Synthesis with Organolithium Reagents

### 4.3.1. Introduction

Anisotropic particles, or Janus particles, are nano- or micromaterials with different functional groups on each side of the surface, like the Roman god Janus, who had two faces. The two-sided Janus particles gain extensive interest due to their unique surface reactivity[200], self-assembly[201], and movement[202]. The realization of Janus SiNCs could expand the scope of such emerging materials.

The strong Si-C covalent bonds of alkyl-capped SiNCs hinder ligand exchange on the Si surface, facilitating anisotropic functionalization. Recently, Kloberg *et al.* developed the first synthesis of Janus SiNCs using a hybrid material consisting of SiNCs on SiNSs (SiNC@SiNS) (Scheme 14).[48] The hybrid was first prepared by thermally induced DHC of the freshly etched H-SiNCs and H-SiNSs, which was subsequently functionalized with alkenes *via* HS. Although both starting materials exhibit photoluminescence, this hybrid interestingly did not exhibit PL emission, which is most likely caused by scattering and charge-transfer processes.[203]

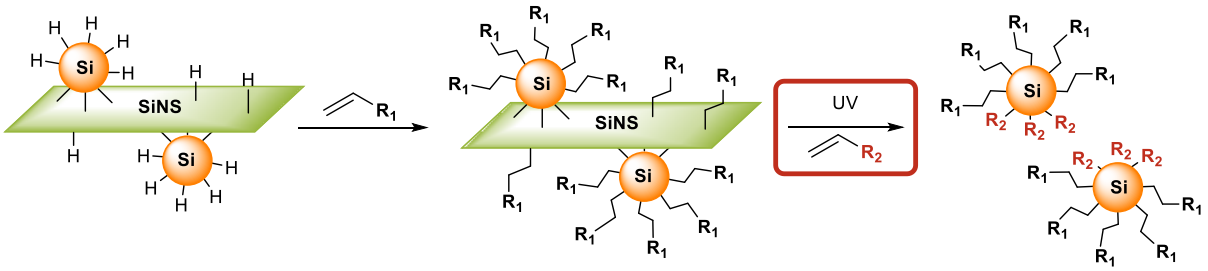


Scheme 14: Synthesis route to Janus SiNCs *via* UV induced HS.

The single-side passivated SiNCs were then subjected with alkenes to a UV lamp to liberate the SiNCs from the nanosheets simultaneously. The UV-irradiation induced degradation of the SiNSs and simultaneous HS functionalization on the other side yielding free-standing luminescent Janus SiNCs. Amphiphilic Janus SiNCs are prepared with one hydrophilic and hydrophobic side of the SiNCs' sphere due to the broad functionalization possibilities. Anisotropy was proven successfully by the fixation of gold wafers and subsequent contact angle measurement.[48]

All synthesis steps were tested successfully for SiNCs with sizes up to 64 nm. However, this reaction route is limited to small SiNCs because the UV-induced HS works only for SiNCs below the Bohr radius of an exciton (< 8 nm).[47] That means that the liberation of the large SiNCs (d > 8 nm) from the SiNSs would still occur, but the HS functionalization rate is significantly decreased, leading to oxidized SiNCs. A way to overcome this limitation requires size-independent functionalization of SiNCs with simultaneous SiNS decomposition in a one-step reaction. Organo-lithium reagents (OLR) induced-functionalization can destroy Si-Si bonds and decompose SiNSs. In contrast to UV-induced HS, OLR functionalizes SiNC

size-independently. Also, capping with OLR allows the introduction of triple bonds and aromatic side groups exclusively because the bond order remains mechanistically. This opens the opportunity to tune the optical properties anisotropically.

At first, the chapter discusses a new synthesis route of Janus SiNCs *via* exclusive organolithium reagent-induced functionalization and modification of SiNSs during the OLR treatment. The obtained Janus $R_1$-SiNC-$R_2$ are defined as follows: $R_1$ is the surface group resulting from HS, while $R_2$ is the substituent of the OLR.

## 4.3.2. Results and Discussion

### 4.3.2.1. Janus Particles

Janus SiNCs of dodecene and phenyl lithium (Dodec-SiNCs-Ph) are first synthesized as depicted in Scheme 15. SiNC@SiNS was first capped with dodecene from a standard HS method initiated by diazonium salt.

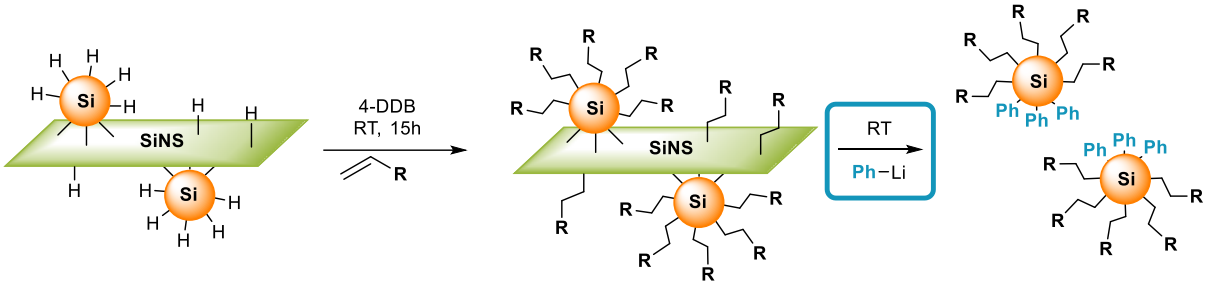


Scheme 15: Initial reaction route of Janus SiNC synthesis with OLR.

Like in the classic approach, the SiNC@SiNS formed an opaque suspension in toluene, which showed no PL (Figure 31a) OLR was then added to the purified materials, and the mixture turned dark and clear with a colorless precipitate. After workup, a clear yellow solution with red PL is obtained (Figure 31c), which indicates that the SiNCs are liberated from the SiNSs and dispersible due to successful functionalization.

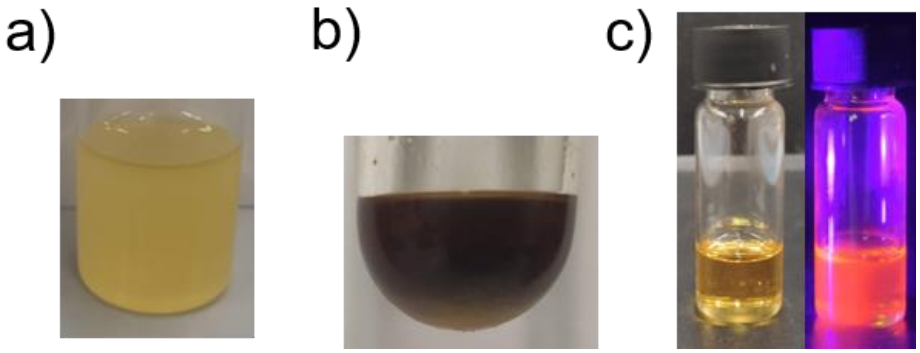


Figure 31: Photos of reaction mixtures of a) functionalized hybrid material b) reaction solution after addition of OLR c) solution Janus SiNCs after workup with and without illumination under UV light.

Figure 32 depicts the FT-IR spectra of the intermediate products and the Janus SiNCs. The hybrid material shows the characteristic stretching modes for $SiH_x$ at 2100 $cm^{-1}$ and $SiO_x$ at

1050 $cm^{-1}$. The strong signal at 900 $cm^{-1}$ is attributed to the $SiH_3$ bending mode. The aliphatic $CH_x$ stretching band is around 2900 $cm^{-1}$, likely from solvent residues.[204] The SiNC@SiNS functionalized with dodecene shows a C=C stretching at 1650 $cm^{-1}$, indicating unreacted dodecene residues that do not disturb further reaction steps. In the purified Janus SiNCs, additional signals around 3050 and 1950 $cm^{-1}$ are visible for aromatic $CH_x$ stretching of the phenyl group. The $SiH_x$ stretching signal is still observable because the OLR functionalization theoretically achieves 50% surface coverage at a maximum. The residing surface stays hydride-terminated. Also, the $SiO_x$ stretching is slightly more intense due to the workup steps that allow oxidation.

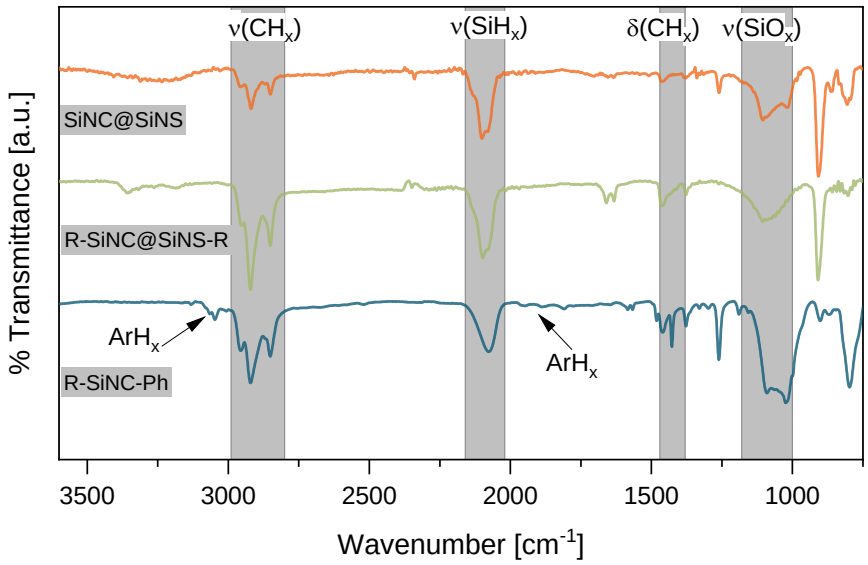


Figure 32: FT-IR of the as-synthesized and functionalized hybrid material and the Janus particles. R describes dodecyl capping.

After successfully preparing Dodec-SiNC-Ph, trimethoxy(vinyl)silane (TMVS) is tested concerning its compatibility with OLR. The Janus SiNCs with the combination of TMVS and HexLi and the uniformly capped SiNCs are characterized by FT-IR, PL, and $^1$H-NMR spectroscopy. The FT-IR spectra (Figure 33a) display the characteristic signals of $SiH_x$, $SiO_x$, and $CH_x$ stretches similar to the previous materials.

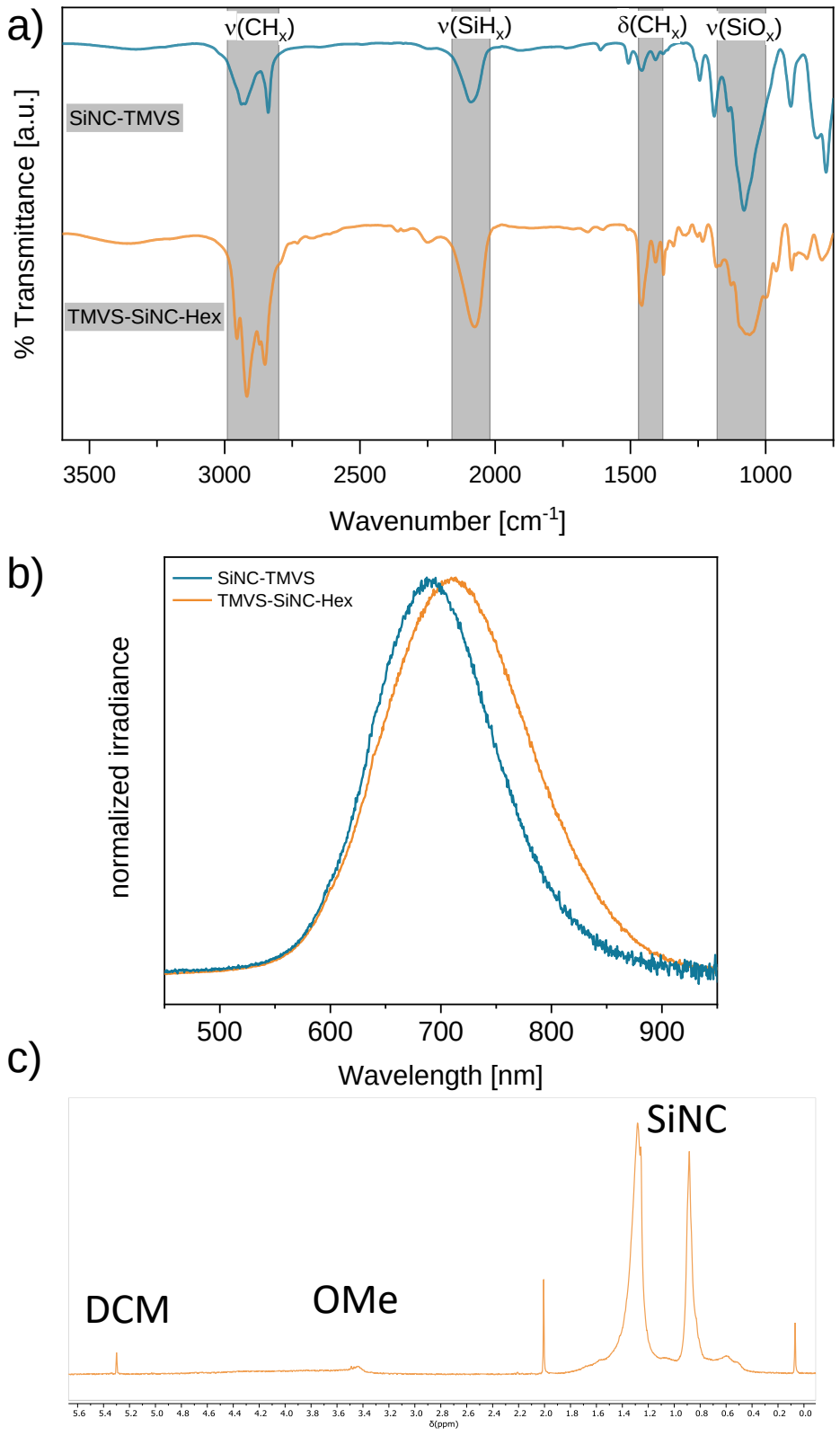


Figure 33 a) FT-IR b) PL spectra c) $^{1}$H-NMR of TMVS-SiNC-Hex and uniformly capped SiNCs with TMVS.

Both samples are luminescent, as depicted in the PL spectra in Figure 33b. The emission maximum deviates slightly because of more methoxy groups at the uniformly capped SiNCs. The $^{1}$H-NMR spectrum shows, besides the typical broad signals of SiNC surface moieties at 0.88 and 1.3 ppm, a peak at 3.5 ppm that corresponds to the methoxy groups. The DCM signal

at 5.3 ppm originates from the Cl/H-exchange, which the SiNCs cause in the presence of $CDCl_3$. The signal at 2.00 ppm indicates acetonitrile residues from workup.

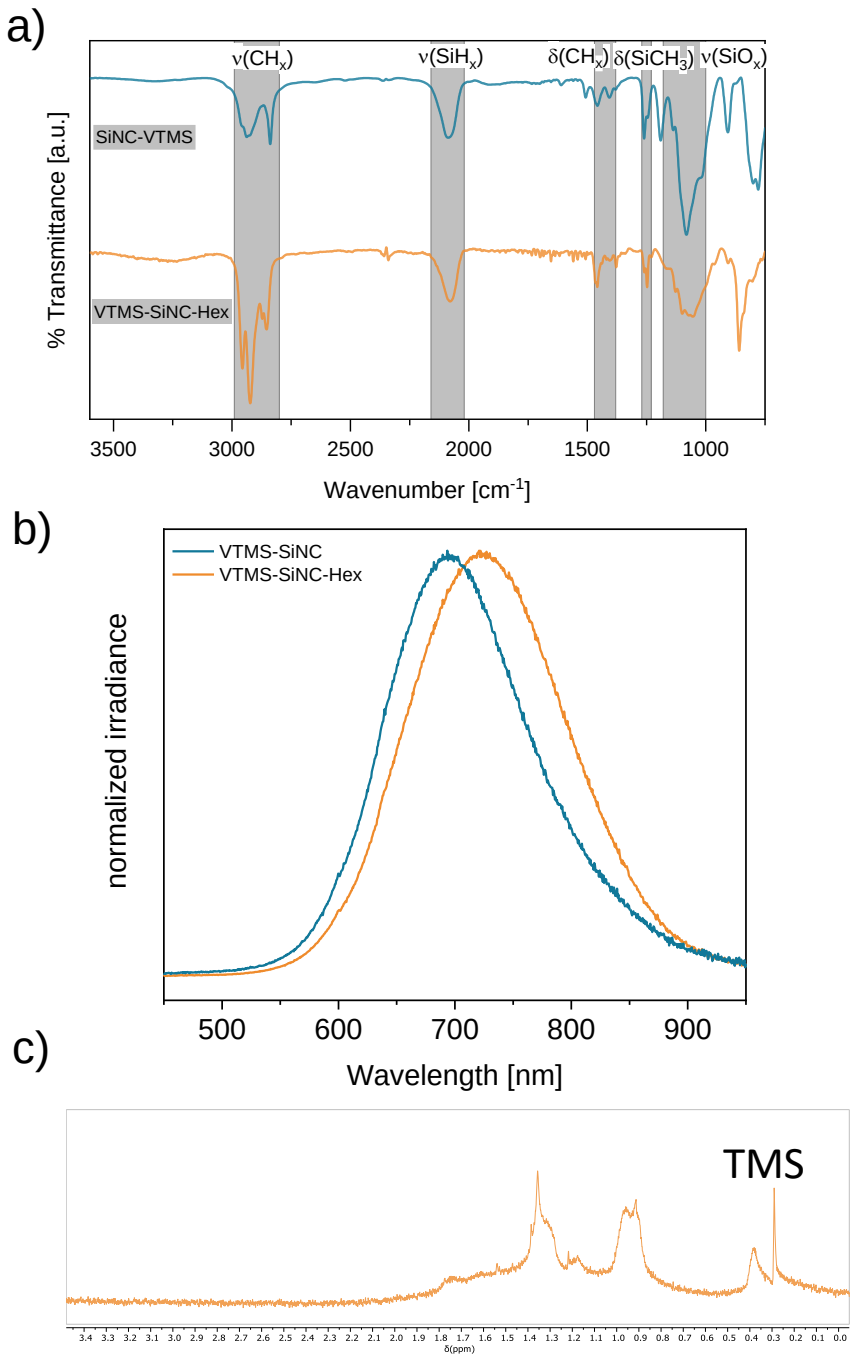


Figure 34: a) FT-IR b) PL c) $^1$H-NMR spectra of (Janus) SiNCs capped with VTMS.

Janus SiNCs are also prepared with (vinyl)trimethylsilane (VTMS) and HexLi to test the compatibility of OLR and enlarge the scope of possible substrates for HS. The samples are characterized with FT-IR (Figure 34a). At 1250 $cm^{-1}$, the $SiCH_3$ stretching of the TMS group is significantly shown for both SiNCs. Furthermore, no C=C stretching at 1650 $cm^{-1}$ is visible, which indicates the absence of unreacted VTMS. The solutions are photoluminescent with a maximum of around 700 nm, displayed in Figure 34 b. The TMS group is detected in the $^1$H-NMR spectrum (Figure 34c) at 0.35 ppm as a broad singlet due to longer relaxation times.[205]

This is caused by inhomogeneous dispersed SiNCs, on which the molecules are covalently bound to the SiNC surface.

#### 4.3.2.2. Capping with Ethynylaryls of 3 and 8 nm Janus SiNC

The functionalization with OLR enables surface motifs on SiNCs, which are impossible with HS (see chapter 2.1.2.1.). The conservation of the bond order (i.e., conjugation of triple bond) leads to conjugated surface groups which offer unique optical properties.

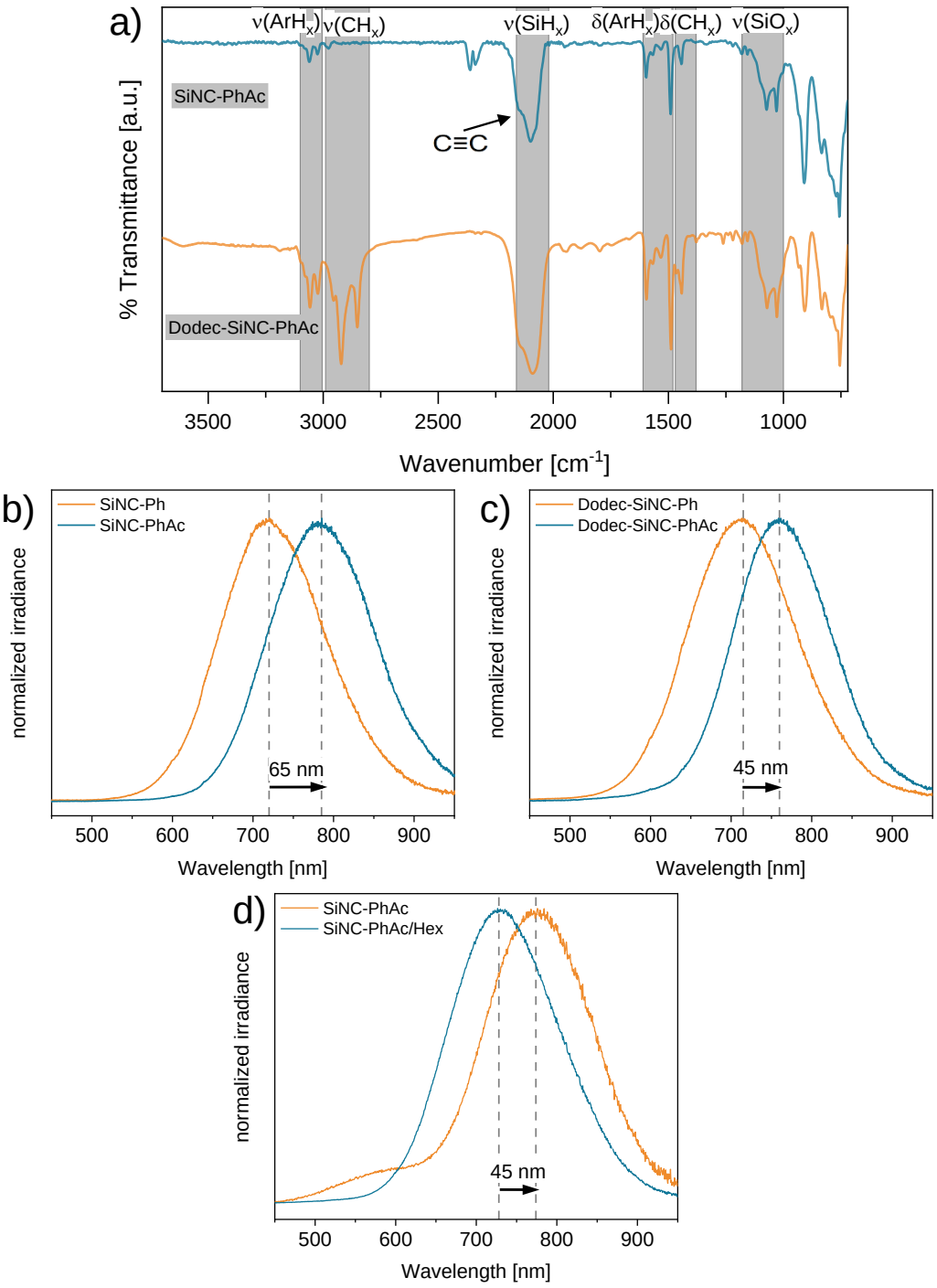


Figure 35: a) FT-IR spectra of Janus SiNCs and uniformly SiNCs capped with PhLi and PhAcLi b) PL spectra of SiNCs capped uniformly with PhLi and PhAcLi c) PL spectra of Janus SiNCs capped with PhLi and PhAcLi d) PL spectra of SiNCs capped with PhAcLi compared to a mixed surface of PhAcLi and HexLi.

Figure 35a compares the FT-IR spectra of (Janus) SiNCs capped with lithium phenylactylide. Both samples exhibit aromatic $CH_x$ stretching around 3050 $cm^{-1}$ and some $SiO_x$ stretching. The $SiH_x$ band at 2100 $cm^{-1}$ contains a shoulder assigned to C-C triple bonds. In conclusion, both functionalizations worked successfully.

SiNCs functionalized with ethynylaryls reveal a redshift in PL maximum due to in-gap states.[84] Figure 35b compares the PL spectra of SiNCs uniformly capped with PhLi and PhAcLi. A redshift of 65 nm is observed due to functionalization with PhAcLi. At Janus SiNCs functionalized with PhLi or PhAcLi, the redshift of 45 nm is slightly smaller (Figure 35c). It is assumed that a lower amount of conjugated surface groups causes the lower redshift. SiNCs functionalized in a 1:1 mixture of HexLi and PhAcLi result in a PL redshift of 45 nm (Figure 35d), which agrees with the observation of the Janus SiNCs.

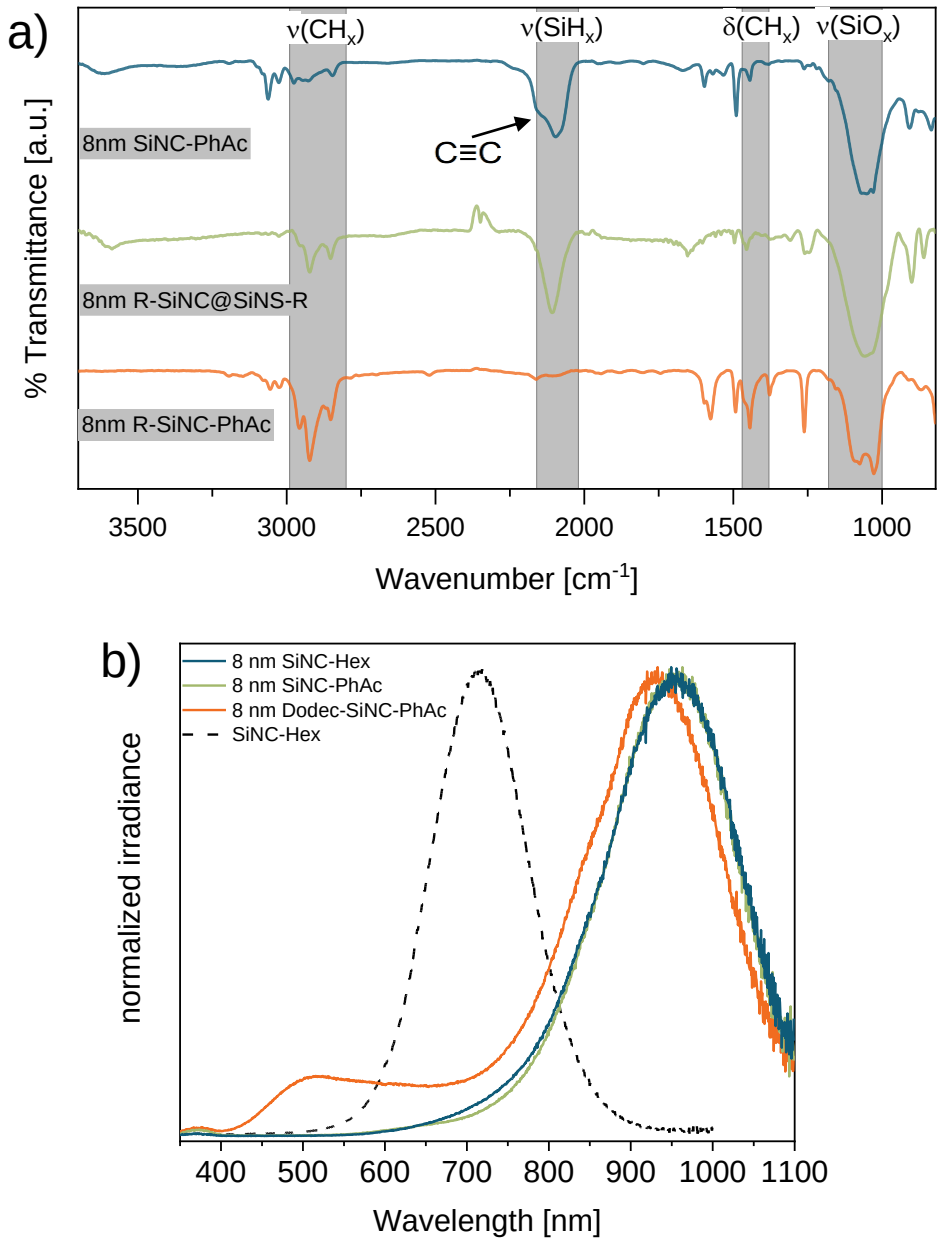


Figure 36: a) FT-IR spectra of 8 nm (Janus) SiNCs capped with PhAcLi and the 8 nm SiNC@SiNS capped with R= dodecyl b) PL spectra comparing 8 nm Janus SiNCs capped with dodecene and lithium phenylacetylide and uniformly capped 8 nm SiNCs with HexLi and PhAcLi. The dotted graph depicts 3 nm SiNCs capped with HexLi.

Another advantage of OLR is size-independency, demonstrated through the functionalization of 8 nm SiNCs here. The FT-IR in Figure 36a depicts the characteristic signals. The uniformly PhAcLi-capped SiNCs show the same signal bands as the 3 nm SiNCs in Figure 35a. The dodecyl side group of the hybrid material features aliphatic $CH_x$ stretching at 2900 $cm^{-1}$, indicating successful HS. The additional C=C stretching bands around 1650 $cm^{-1}$ from the dodecene starting material diminishes after the reaction with OLR. Afterward, the 8 nm Janus SiNCs exhibit aromatic and aliphatic $CH_x$ stretching signals at 3050 and 2900 $cm^{-1}$, respectively. Surprisingly, the Janus SiNCs do not show $SiH_x$ signal bands at 2100 $cm^{-1}$. It is assumed that due to the harsher workup in acid, the sample gets oxidized more than 3 nm Janus SiNCs. Regardless, the result here indicates that the OLR functionalization mechanism is independent of the SiNC size.

In contrast to the previous luminescence results of 3 nm SiNCs, 8 nm SiNCs no PL redshift with ethynylaryls is visible at all (Figure 36b). The emission maximum of Dodec-SiNC-PhAc is slightly blue-shifted, which is caused by the higher amount of oxidation compared to uniformly capped SiNCs. Additionally, it exhibits a shoulder around 500 nm, which reveals incomplete liberation due to characteristic PL signals of SiNSs.

#### 4.3.2.3. Destruction of SiNSs

While compositional and optical characterizations have suggested successful functionalization of Janus SiNCs from NS, the liberation of the SiNCs from the SiNSs *via* OLR is essential to understand. Therefore, a microscopic study is performed to examine the material before and after the addition of OLR. Figure 37a shows a TEM picture of incompletely liberated Janus SiNCs.

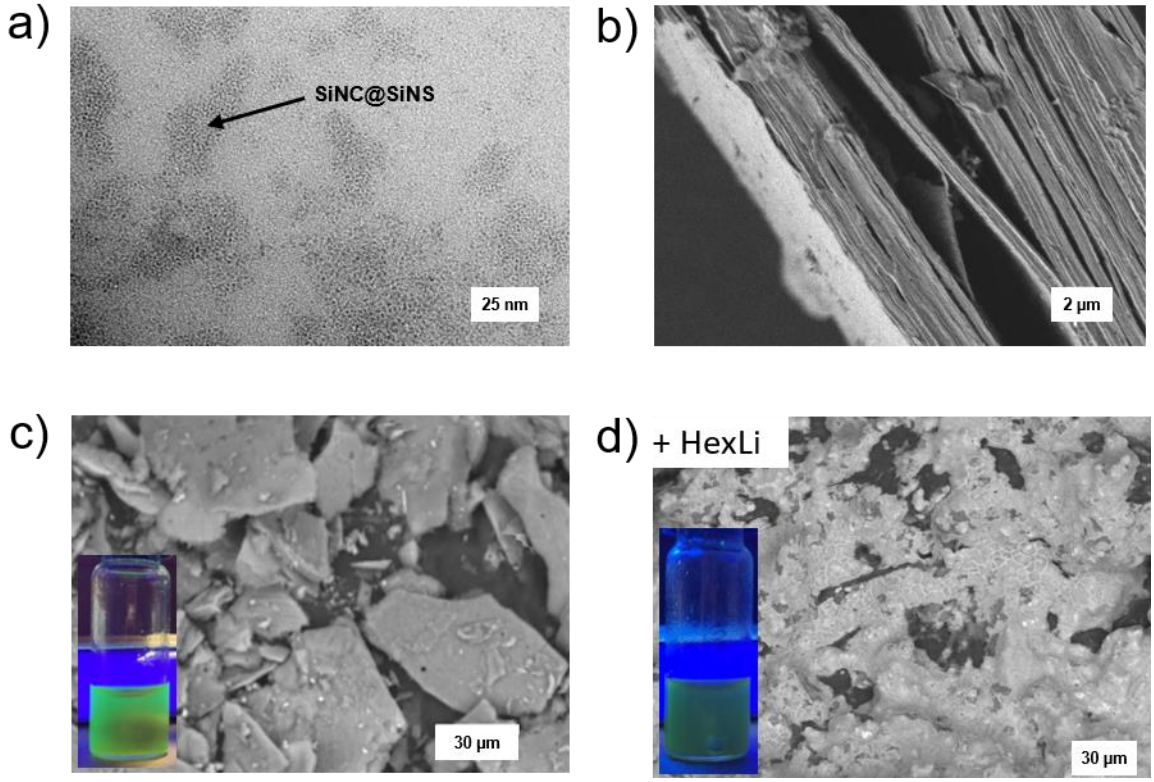


Figure 37: a) TEM picture of incomplete liberated SiNCs (assigned with an arrow). SEM pictures of b) stacked SiNS layers c) dodecyl capped SiNSs before and d) after the addition of HexLi. Insets: dispersions under UV light.

The dark groups of spots represent intact SiNC@SiNS and indicate a surplus of 2 eq. OLR is not sufficient to destroy all the SiNSs. A longer reaction time of 20 h for the OLR step did not improve SiNC liberation determined by TEM measurements. In combination with OLR, SiNCs would cause a dark solution. Thus, tracking the reaction progress is more complicated than hydrosilylation, where the reaction mixture turns clear after successful passivation. So dodecyl-capped SiNSs instead of SiNCs are mixed with HexLi in a toluene solution for further SEM study.

Insets of Figure 37c and d are photographs of the yellow SiNS solution with green PL before and after OLR addition. As shown, the reaction mixture turned colorless opaque, and lost PL. SEM enables a closer look at the nanosheet structure. The microscopic images (Figure 37c and d) showed the thick stacked sheets of the SiNSs get destroyed into thinner and smaller stacks. These observations align with the OLR reaction mechanism where Si-Si bond cleavage occurs. The monolayers of silicane break and are additionally destroyed by the alkalinity of the OLR. The incomplete liberation can be explained by the SEM picture in Figure 37b as freshly etched SiNS-H still form stacks of hundreds of layers. The OLR is sterically hindered from reaching the surface of each layer, and therefore incomplete liberation takes place.

Increasing the conventional ultrasonication time (i.e., 5 min) could increase liberation. The microscopic images reveal that sonication of SiNSs between 5 min and 30 min leads to different levels of sheet separations from the original stack (Figure 38).

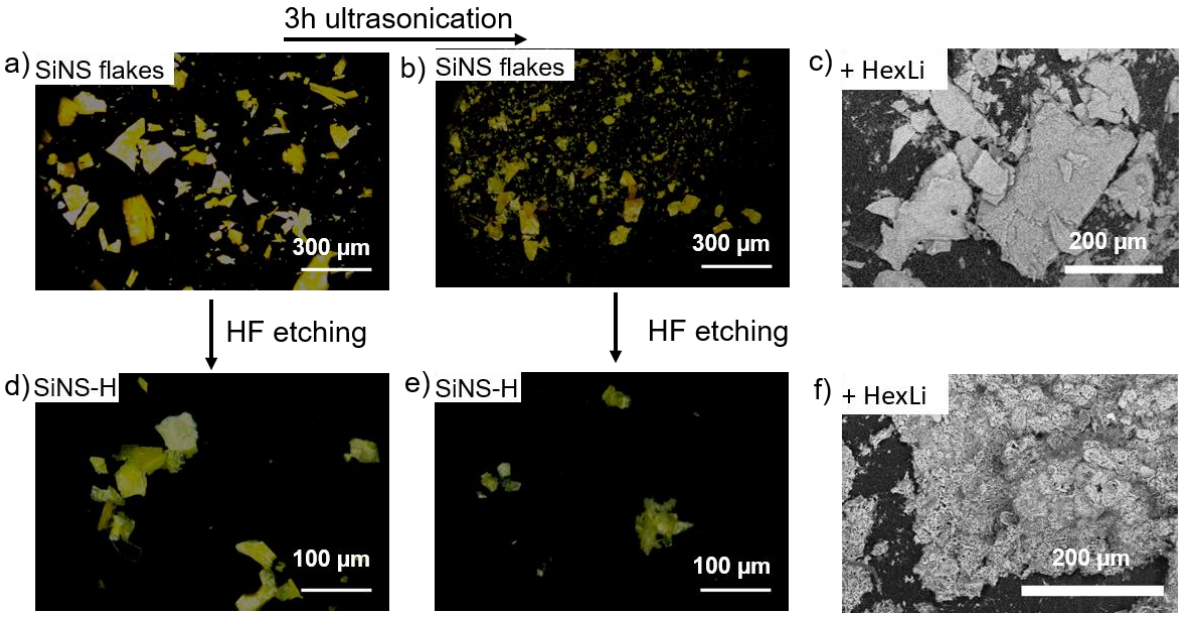


Figure 38: Scheme with microscope pictures of SiNS flakes a) after 5 min ultrasonication b) after 3 h ultrasonication c) after addition of HexLi d) freshly etched SiNS-H from classical route e) optimized route with more extended ultrasonication f) after addition of HexLi.

The SiNS flakes, as well as the etched SiNS-H, indicate a smaller average size. Figure 38c and Figure 38f further show the SiNS flakes and SiNS-H after HexLi addition, respectively. The sheet structure of the SiNS flakes is still intact as they appear as stacked layers. The SiNS-H look more destroyed with a longer sonication time, which would promote the SiNC release.

### 4.3.3. Summary and Outlook

Herein, a new synthesis approach for Janus SiNCs was described. At first, hydrosilylation passivated a hybrid material containing SiNSs decorated with SiNCs; in the second step, an OLR was utilized for functionalization and liberation. (Vinyl)trimethylsilane and trimethoxy(vinyl)silane were tested with HexLi on Janus SiNCs to investigate the compatibility

and the scope of hydrosilylation surface groups. The successful capping was confirmed *via* FT-IR and $^{1}$H-NMR with both surface groups present.

The new synthesis approach was extended to larger SiNCs than 5 nm and overcame the limitation of the UV-based synthesis. 8 nm were successfully functionalized with phenyl lithium and dodecene, confirmed by FT-IR. Unique surface groups like ethynylaryls or phenyls were also introduced for special optical properties. 3 nm Janus SiNCs capped with dodecene and PhAcLi exhibited a PL redshift of 45 nm compared to the results of a randomly mixed surface with PhAcLi and aliphatic HexLi. In contrast to uniformly PhAcLi functionalized SiNCs (65 nm), the PL redshift was slightly lower.

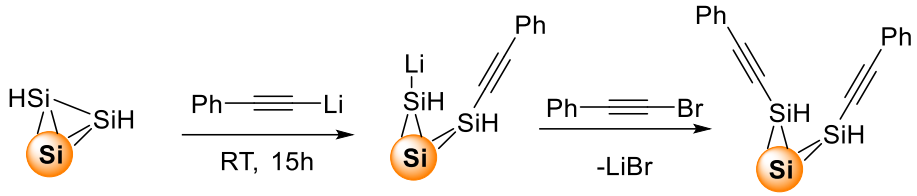


Scheme 16: Alternative workup for higher redshifts with phenylacetylene bromide.

An increased redshift may be achieved by a workup with phenylacetylene bromide instead of HCl, as depicted in Scheme 16. The amount of ethynylaryl surface groups would double theoretically. Further research needs to aim for the final proof of anisotropy by fixation of the Janus SiNCs on wafers for contact angle measurement.

## 4.4. Silicon Nanosheet Motors

### 4.4.1. Introduction

Catalytic nanomotors are defined by Gibbs *et al.* “as nano-to micrometer-sized actuators that carry an on-board catalyst and convert local chemical fuel in solution into mechanical work.”[206] More easily, catalytic nanomotors are nanoscaled particles that utilize the surrounding fuel to achieve movement. Therefore, nanomotors contain catalytic parts that convert the fuel into, e.g., gaseous products. These gaseous product bubbles induce the propellation of the nanomotors. The first nanomotors are invented at the beginning of this century. While Ozin *et al.* developed nanorotors, Paxton *et al.* investigated striped nanorods as a nanomotor structure propelled by interfacial tension.[207,208]

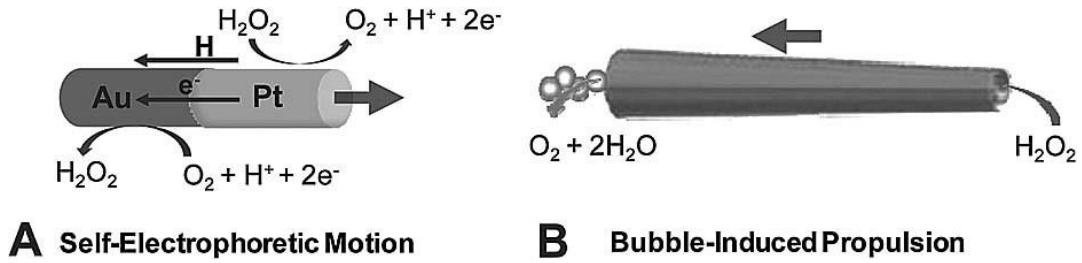


Figure 39: Two different shapes of nanomotors and their propellation technique. Reprinted with permission from Ref.[209].

Their structure and synthesis are simpler than biomotors, which need enzymes to convert the biologically relevant fuel adenosine triphosphate (ATP).[210] Since then, locomotion mechanisms have been developed. Diffusiophoresis achieves propulsion *via* a concentration gradient of the fuel interacting with the nanomotors’ surface.[211] Another propulsion mechanism for catalytic nanomotors is self-electrophoresis (Figure 39a).[207] There, redox reactions on bimetallic nanomotors’ surfaces cause local charge imbalances.[212] By introducing magnetic moieties to the nanomotors, the motion can be controlled in a magnetic field.[213] The most applied propulsion technique is the production of gas bubbles in the opposite direction of the movement (Figure 39b). The application of these structures reaches from drug delivery to a cargo carrier in chips.[214–216]

For propelling nanomotors, mostly Pd or Pt moieties are used. These metals catalyze the decomposition of hydrogen peroxide into oxygen and water. The evolution of gaseous oxygen is utilized for particle movement. Tabrizi *et al.* investigated 2D gold nanosheets with CoPt alloys to a facile design of new nanomotors.[213] Another 2D nanomaterial that is a potential candidate for nanomotors is SiNSs because of their excellent reducing properties. Under aqueous conditions, SiNSs reduce metal salts to yield metal nanoparticles that decorate the SiNS surface.

In the literature, SiNSs are already utilized to reduce metal salts to metal nanoparticles (MNP) and catalyze various reactions. For example, the group of Nakano observed the formation of

metal nanoparticles on the SiNS surface upon adding different metal salts.[153] They used the resulting hybrid material of palladium nanoparticles and SiNSs (PdNP@SiNS) for the catalytic decomposition of formic acid. Qian *et al*. combined Pd(II)-acetate with SiNSs to create a hybrid material that acts as a catalyst for $CO_2$ reduction.[152] Germanene, as the heavier homolog of SiNSs, was decorated with metal nanoparticles and utilized as a photocatalyst for the aerobic oxidation of benzyl alcohol.[217] The catalytic application of PdNP@SiNS is obvious as palladium nanoparticles (PdNPs) alone already catalyze cross-coupling, alcohol oxidation, or hydrogenation reactions.[218–220]

The construction of a SiNSs and Pd-based catalytic nanomotor is aimed, propelled by the evolution of oxygen bubbles (Scheme 17).

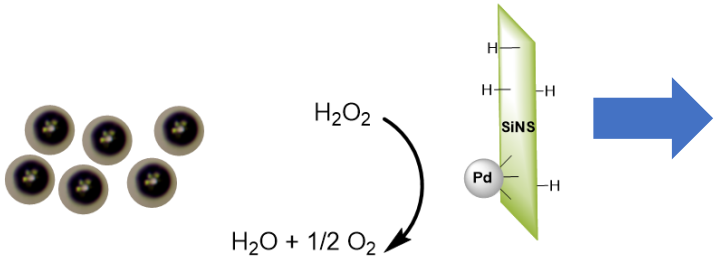


Scheme 17: Structure and general working principle of the NSM. The blue arrow depicts the movement direction.

A necessary condition for a successful nanomotor is the anisotropic structure. The propelling PdNPs should be fixed only on one side of the SiNSs. In this chapter, the reduction of various metal salts is first investigated and then the reaction parameters are optimized. In the second part, literature-known synthesis approaches are applied to anisotropic 2D nanomaterials to decorate SiNSs with PdNP.

## 4.4.2. Results and Discussion

### 4.4.2.1. Reduction of Metal Salts with SiNS

According to Ohashi *et al.,* the standard electrode potential of SiNSs lies between $Ni^{2+}/Ni$ (-0.257 V) and $Cu^{2+}/Cu^{+}$ (0,159 V).[153] Hence, $Cu^{2+}$ is barely reduced by SiNSs, and the reduction potential of SiNSs is insufficient for $Ni^{2+}$. Metal ion combinations with a higher standard electrode potential, e.g., noble metals like Au, Pd, and Pt, would be reduced more easily by SiNSs. This complicates the investigation of reaction parameters concerning the successful reduction. In the following experiments, reaction parameters (metal salt anions, reducing nanomaterial, metal/SiH ratio) for reducing copper salt to copper nanoparticles on the SiNS surface (CuNP@SiNS) are investigated.

At first hybrid materials of SiNSs and MNP are synthesized *via* the reduction of different metal salts under aqueous conditions analogous to Ohashi *et al*.[153] The SiNSs obtained from $CaSi_2$ exfoliation and HF etching are mixed with a surplus of metal salts dissolved in water or diluted acid, depending on the solubility. After ultrasonication of 1 h, the resulting dark suspension is

filtered. The obtained solid is purified from residing metal salt by washing it with water. XRD characterization is conducted to identify metal salt residues.

Figure 40 shows the XRD of freshly etched SiNSs (SiNS-H) and SiNSs containing gold, palladium, and copper NP. The freshly etched SiNSs exhibit broad reflexes for the 001 and 100 crystal planes around 15° and 27°, which fit literature values.[221] The XRD plots of the hybrid materials additionally show the reflexes of the elemental metal nanoparticles of the respective (111), (200), and (220) planes. The metal salt precursors are not observable in the XRD, indicating that their residues are washed out thoroughly at workup.

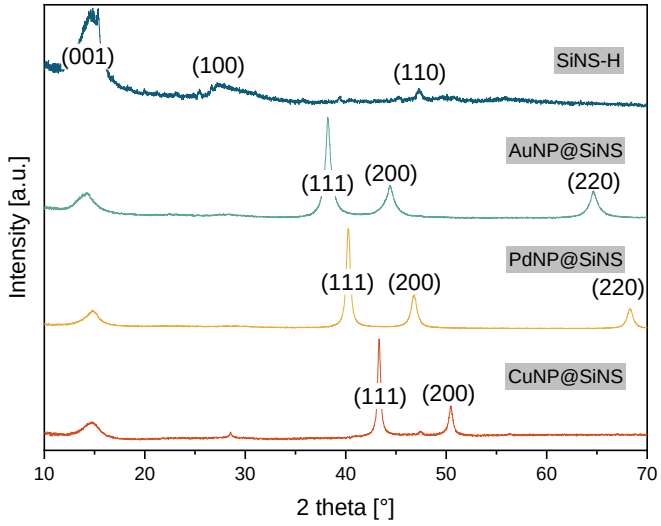


Figure 40: XRD analysis of etched SiNSs and hybrid materials of gold, palladium, and copper nanoparticles on SiNSs.

Also, the reaction parameters of the metal reduction are investigated further. Specifically, the impact of the metal salt anion, the metal ion charge, the reducing Si nanomaterial, and the ratio of metal salt to SiNSs is investigated. At first, the Cu(II)-salt anion is varied from nitrate to sulfate, acetate, and chloride. Cu(I)-chloride is also tested to see an impact on the metal oxidation state. After ultrasonication, all solutions turn to a dark brown color, which indicates the turnover to CuNPs with oxidation state Cu(0). FT-IR and XRD characterize the resulting material to determine differences in the composition. The reflex at 36° in the XRD pattern in Figure 41a belongs to copper(II)-oxide, which is only absent in the case of $CuCl_2$.[222] That means in all other samples, the CuNPs are oxidized. Besides the reflexes of the SiNSs at 15° and 27°, reflexes of elemental copper are dominant, as depicted in red reference lines underneath the plot.[146] The results of XRD show the successful synthesis of CuNP@SiNS. These results are complemented by FT-IR to confirm that the reduction occurs mechanistically by oxidation of the SiNSs (Figure 41b).

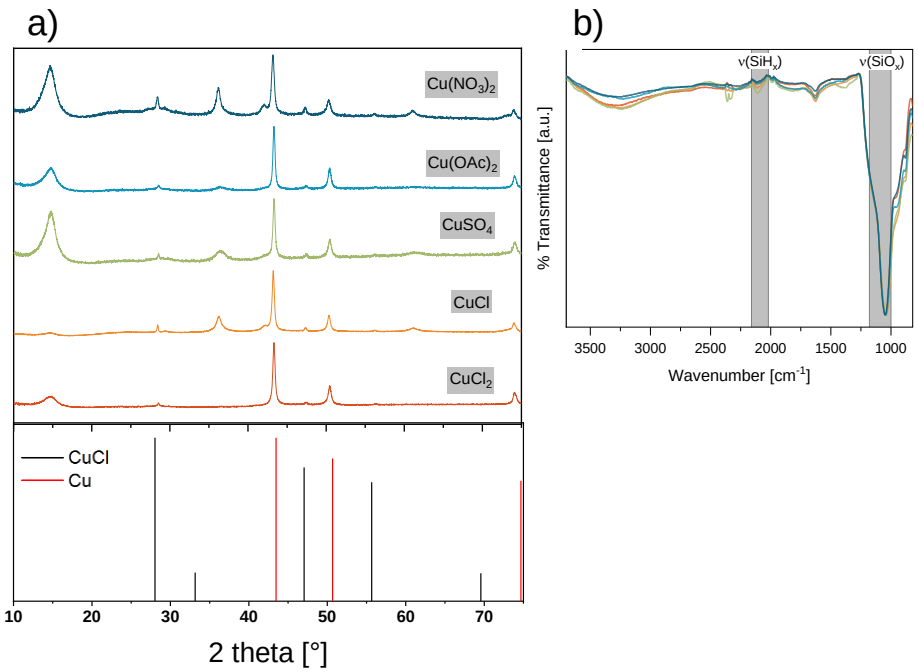


Figure 41: a) XRD pattern of the CuNP@SiNS prepared by different copper salts. The lower part of the figure displays the reference reflexes for Cu and CuCl. b) FT-IR spectra of the CuNP@SiNS prepared by different copper salts

Besides a weak SiHx stretching band at 2100 $cm^{-1}$, it shows a strong $SiO_x$ stretching band at 1050 $cm^{-1}$ for all samples. This indicates that the SiNS surface is oxidized while the metal salts are reduced. The FT-IR shows water residues in the material because there is a broad stretching band at 3300 $cm^{-1}$ and a deformation band at 1620 $cm^{-1}$. In conclusion, the copper salts do not influence the reduction severely, so the less costly $CuCl_2$ is utilized as a metal salt precursor for further experiments. Ohashi et al. investigated only etched SiNSs for metal salt reduction.[153]

In the next experiment, the reducing silicon nanomaterial is varied. For a facile and inexpensive synthesis of these hybrid materials, unetched SiNS flakes are considered to avoid HF etching. Furthermore, the self-made precursor $CaSi_2$ for the SiNS flakes is compared to more abundant commercial $CaSi_2$. Also, the impact of surface capping of SiNSs on the reactivity toward metal salts is investigated. It is assumed that the lower amount of SiH surface moieties and reduced steric abundance of organic capping groups decrease the reduction potential of SiNSs. The following figure summarizes the results of the experiment's FT-IR and XRD analysis. The FT-IR spectra in Figure 42a show strong $SiO_x$ stretching at 1050 $cm^{-1}$ for all samples. Additional signals are only observed for SiNS-Dodec, which displays aliphatic $CH_x$ stretching and deformation bands around 2900 $cm^{-1}$ and 1450 $cm^{-1}$, respectively. For the etched SiNS-H, a weak $SiH_x$ stretching band at 2100 $cm^{-1}$ indicates that the SiNSs are not completely oxidized. XRD analysis in Figure 42b exhibits that the SiNSs of the commercial precursor contain CaO as a side phase. The commercial materials still show some residing reflexes of CuCl, which indicates incomplete reduction. The self-made SiNS flakes show reflexes at 37° and 62° for oxidized CuNP. The etched SiNS-H work best for metal salts reduction because the typical

reflexes for intact SiNSs at 15° and 27° are visible. Besides that, reflexes for elemental copper at 43° and 50° appear, which is unsurprising, as the etching removes surface oxide moieties and yields Si-H surface groups as reducing agents. In conclusion, the commercial SiNS precursor material shows lower reactivity towards CuNPs compared to the self-made material due to the presence of disturbing side phases.

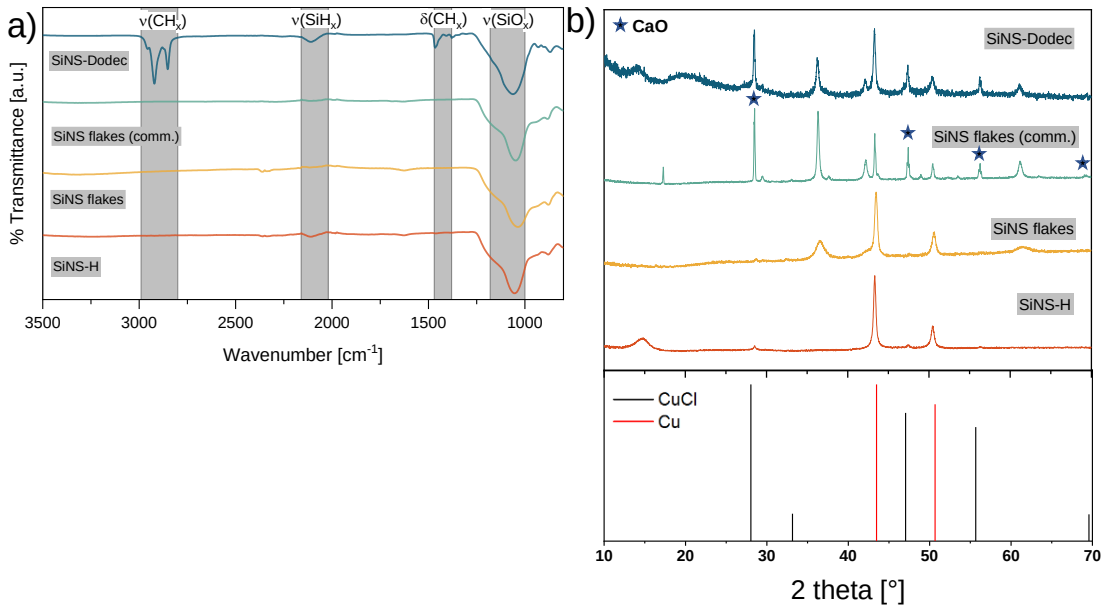


Figure 42: a) FT-IR spectra b) XRD of CuNP@SiNS observed by reduction of $CuCl_2$ with different nanomaterials. The blue stars mark reflexes of CaO as contaminating phase from the commercial $CaSi_2$.

The previous reactions are performed with a surplus of 2 eq. of metal salt. Now, $CuCl_2$ is added stoichiometrically with respect to the SiNSs to investigate whether the reduction by SiNSs runs quantitatively. The XRD pattern in Figure 43 shows complete turnover to CuCl moieties at 1 eq, but 2 eq. are needed for complete conversion to CuNP.

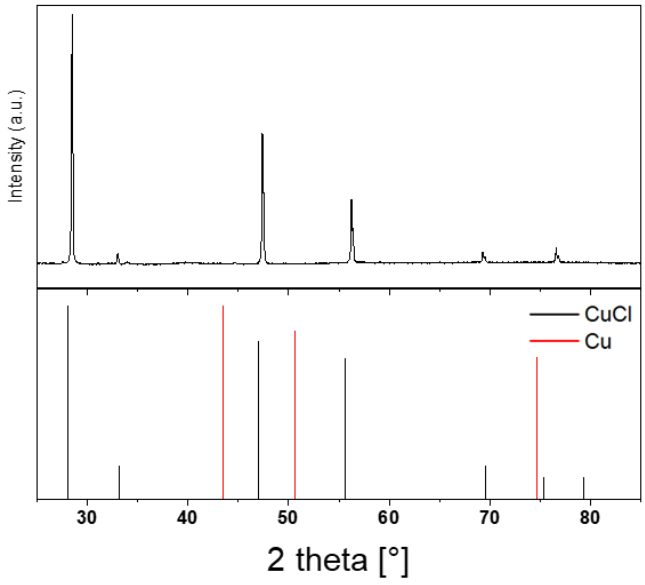


Figure 43: XRD pattern of SiNSs ultrasonicated with $CuCl_2$ in $CuCl_2$/SiH ratio = 1

The last section described the optimization of reaction parameters. These findings are applied to the synthesis of PdNP@SiNS. This material is used because Pd moieties catalyze the decomposition of hydrogen peroxide fuel. In this reaction, oxygen bubbles are obtained, which propel the nanomotors.

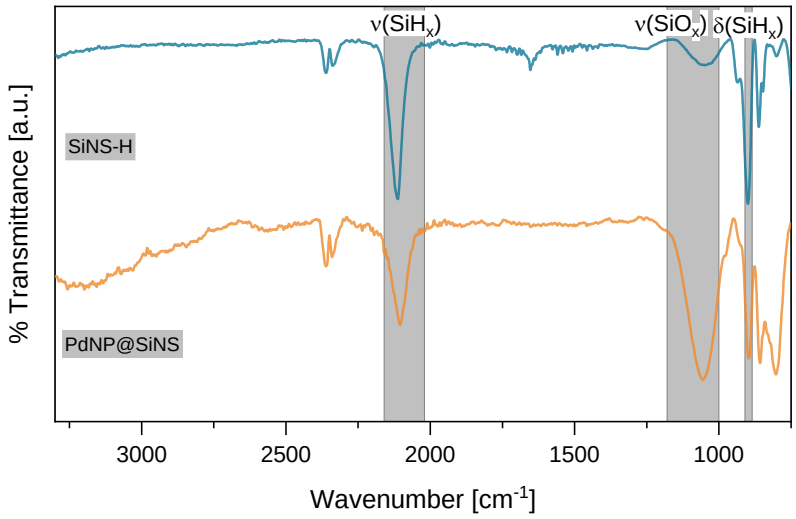


Figure 44: a) FT-IR spectra comparing etched SiNSs with the hybrid material PdNP@SiNS.

The synthesized PdNP@SiNS is characterized by FT-IR and compared to etched SiNSs. In Figure 44a, the FT-IR spectra depict an intense $SiO_x$ stretching at 1050 $cm^{-1}$ in contrast to SiNS-H. That means the SiNSs got oxidized, indicating a successful decoration of the SiNSs with PdNP.

### 4.4.2.2. Synthesis of Anisotropic 2D Material

The overall condition for the successful synthesis of nanomotors is the anisotropic decoration with PdNP. Otherwise, random motion is observed. The movement of PdNP@SiNS is tracked in a cuvette with diluted hydrogen peroxide solution with a light microscope. The nanomotor in the orange frame is followed over ten seconds, as depicted in Figure 45. This random motion indicates that propelling PdNPs are fixed isotropically on both sides. Anisotropic decoration of the PdNPs by masking SiNSs would avoid this problem. Masking means that one side of the SiNSs needs to be inaccessible during the reduction of $PdCl_2$.

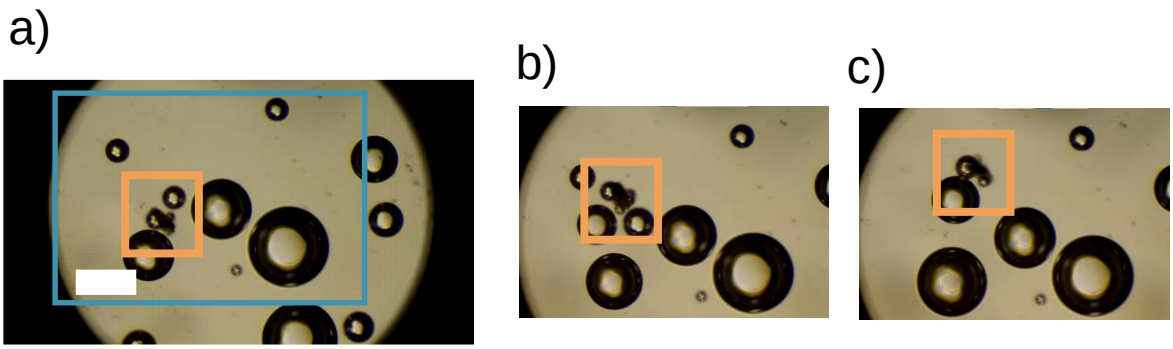


Figure 45: PdNP@SiNS nanomotor at a) t=0 s b) t=5 s c) t=10 s. The white scale bar is assigned to 200 µm.

Literature offers several approaches for the anisotropic synthesis of 2D nanomaterials, like crushing hollow spheres[223], interface synthesis[224], dropcasting[225], or *via* Pickering emulsion[226]. Crushing hollow spheres functionalized differently inside and outside is not applicable for SiNSs. Before the reduction of metal salts is possible, the material needs to be exfoliated exclusively from $CaSi_2$ and etched.[223]

As the first realizable method, the functionalization of SiNSs at an interface is investigated. Therefore, anisotropic capping of the SiNS surface with dodecyl groups is performed to deactivate one side of the SiNSs for the subsequent reaction with the metal precursor. On the interphase of two immiscible solvents, the SiNSs arrange themselves and are functionalized with dodecene Figure 46a. The subsequent reduction of metal salts can occur only at the unfunctionalized side of the SiNSs, as depicted in Figure 46b. Unfortunately, the SiNSs assembled at the glass wall of the flask instead of arranging themselves at the interphase (Figure 46c). Also, hydrophobizing the flask inverted the solvent order but did not prevent SiNSs from sticking to the glass wall.

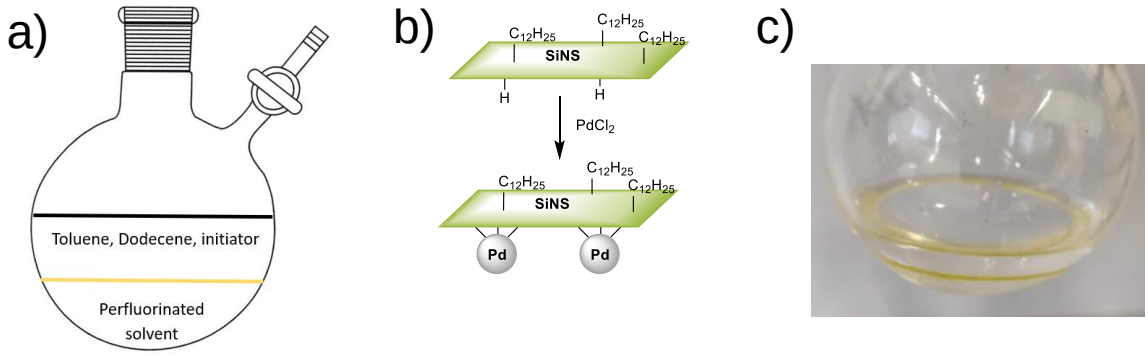


Figure 46: Anisotropic functionalization of SiNSs with dodecene a) Scheme of reaction flask the yellow line depicts the arranged SiNSs. b) Reaction scheme of the anisotropically capped SiNSs with $PdCl_2$. c) Instead of arranging at the interphase, SiNSs assemble at the flask wall.

Dropcasting of the SiNSs on glass is tried next. With this method, the nanomaterial should become inaccessible on the side which faces the glass substrate. For drop-casting SiNSs, pentane and toluene are tested. Figure 47a depicts the different patterns with both solvents. While in toluene, the SiNSs are evenly distributed throughout the solution, in pentane, they tend to assemble due to the rapid evaporation of the solvent. But upon adding the metal salt solution, the SiNSs release from the glass surface (Figure 47b). Finally, the SiNSs are decorated with PdNPs on both sides, where oxygen bubbles are observable on both sides (Figure 47c).

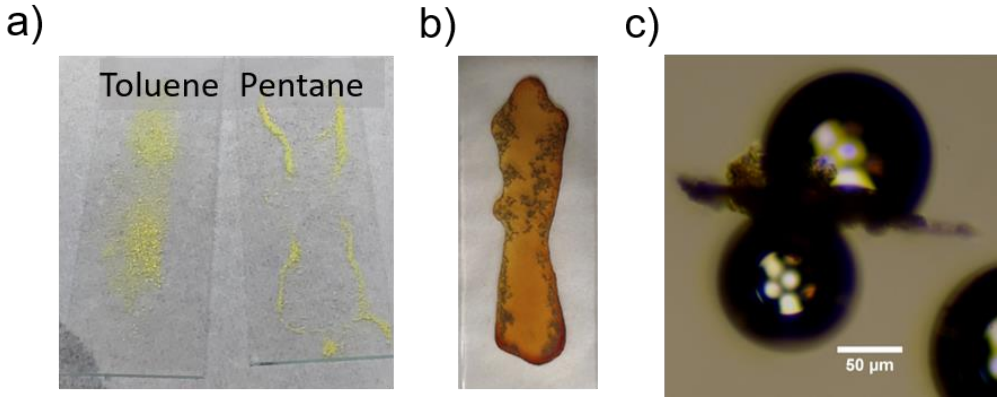


Figure 47: a) Photos of SiNS-H drop-casted on glass substrates with the respective solvent. b) after adding $PdCl_2$ solution c) microscope picture of NSM from drop-casting.

The following approach compares drop-casting and pressing the SiNSs on carbon tape. It is assumed that the tape's more adhesive nature improves the masking of one side of the SiNSs compared to the glass substrate. Figure 48 summarizes the observation of this row of experiments. At drop-casting, the amount of SiNSs per area is lower than at pressing. Both materials possess a shining metal surface after addition, but at drop-casting, some brown residues of $PdCl_2$ are still observable (Figure 48c). The hybrid material, scratched from the carbon tape, shows a low activity in $H_2O_2$ splitting and no moving particles. In contrast, the nanomotors of the pressed SiNSs are very reactive; however, no directed movement is observed.

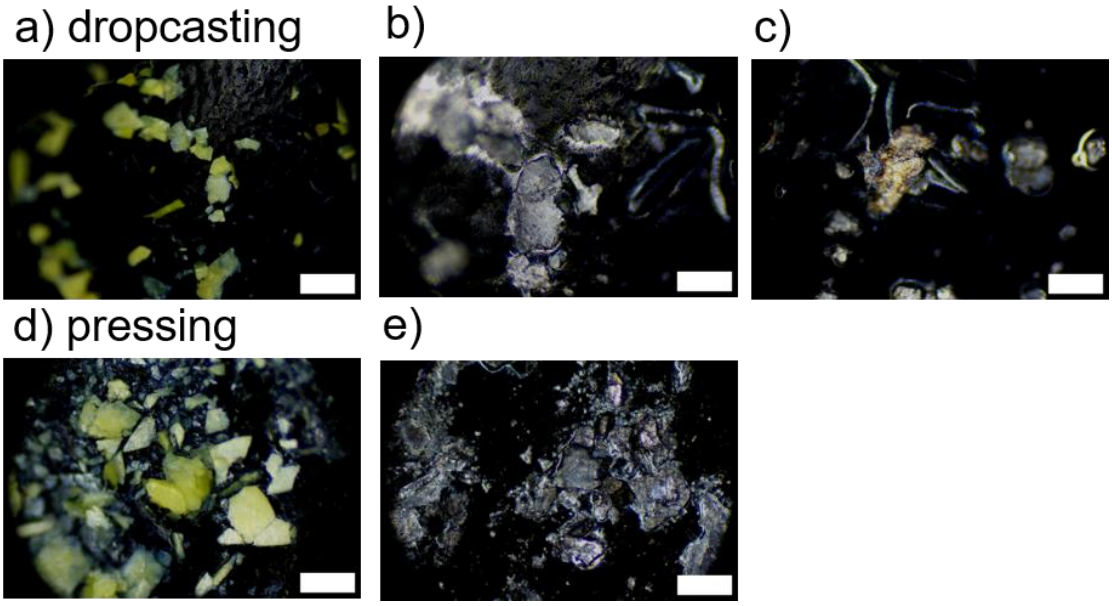


Figure 48: Microscope images of SiNSs a) drop-casted and d) pressed onto carbon tape. b) and e) show the SiNSs fixed with the respective method after treatment with PdCl2 solution. c) unreacted $PdCl_2$ residues. The scale bar is assigned to 200 µm.

In another approach, SiNSs are immobilized on wax particles rather than fixed on one side of a flat substrate. Pickering emulsions are common for preparing Janus particles but also anisotropic 2D materials.[227–229] Figure 49a depicts the setup for preparing the Pickering

emulsion. Therefore, wax is melted and ultrasonicated in water to generate an emulsion. For stabilization, solid nanomaterials are necessary.

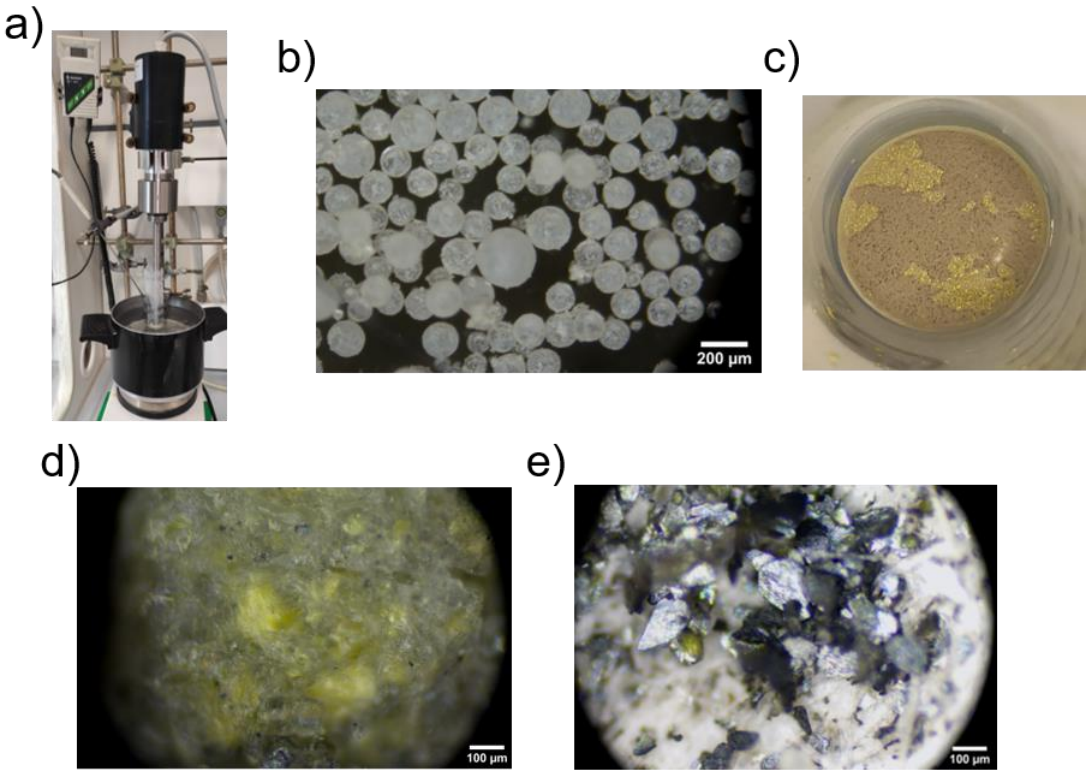


Figure 49: a) Setup for PE b) wax spheres formed with SiC nanoparticles (~100nm) c) PE with SiC NP and SiNSs d) SiNS@wax e) SiNS@wax after reduction of $PdCl_2$.

The test reaction is performed with SiC nanoparticles with dimensions of ~100 nm and yields wax particles with a narrow size distribution (Figure 49b). In combination with SiNSs, the formation of wax spheres failed because the SiNSs distributed irregularly. Figure 49d shows the SiNSs embedded deeply in wax. After adding $PdCl_2$, big Pd particles are observed, which are not fixed on the SiNS surface (Figure 49e).

In conclusion, all classical synthesis approaches did not yield anisotropically decorated SiNSs. Furthermore, the material showed no directed movement in diluted $H_2O_2$.

#### 4.4.2.3. Addition of Metal Nanoparticles

The previous approaches remained unsuccessful in decorating SiNSs on one side with PdNPs by a simultaneous reduction of $PdCl_2$. In this chapter, the nanomotor synthesis is facilitated because pre-reduced PdNPs are mixed with SiNSs. PdNPs are synthesized according to a classical route *via* a reduction in citric acid.[230] After separating the nanoparticles from the solution *via* centrifugation, SiNS-H are added (Figure 51a). The resulting hybrid material PdNP+SiNS is investigated. Figure 50 shows the straight movement of one nanomotor over 10 s. The oxygen bubbles leave traces of the previous location of the nanomotor.

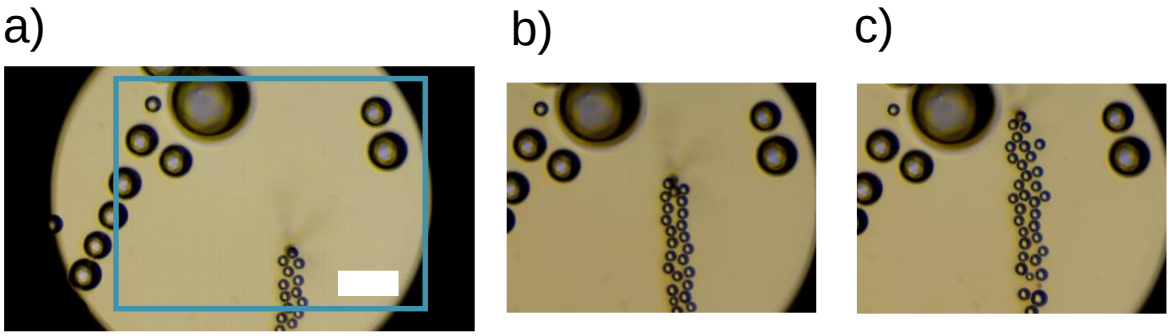


Figure 50: Microscope pictures of PdNP+SiNS nanomotor at a) t=0 s b) t=5 s c) t=10 s. The white scale bar is assigned to 200 µm.

Further characterization is done to explain the different behavior of both nanomotor structures. Figure 51b depicts the XRD of freshly etched SiNS-H, PdNP+SiNS, and PdNP@SiNS. In the pattern of PdNP+SiNS, the typical reflexes for PdNPs remain absent due to the low amount of PdNP. SEM-EDS also confirmed this because no Pd could be detected for this material. But TEM pictures in Figure 51 b and c show the difference between the two materials. While PdNP@SiNS contains only a few PdNPs that exhibit a size around 29 nm, at PdNP+SiNS, much smaller PdNPs with an average diameter of 6 nm and a lower size distribution are observed.

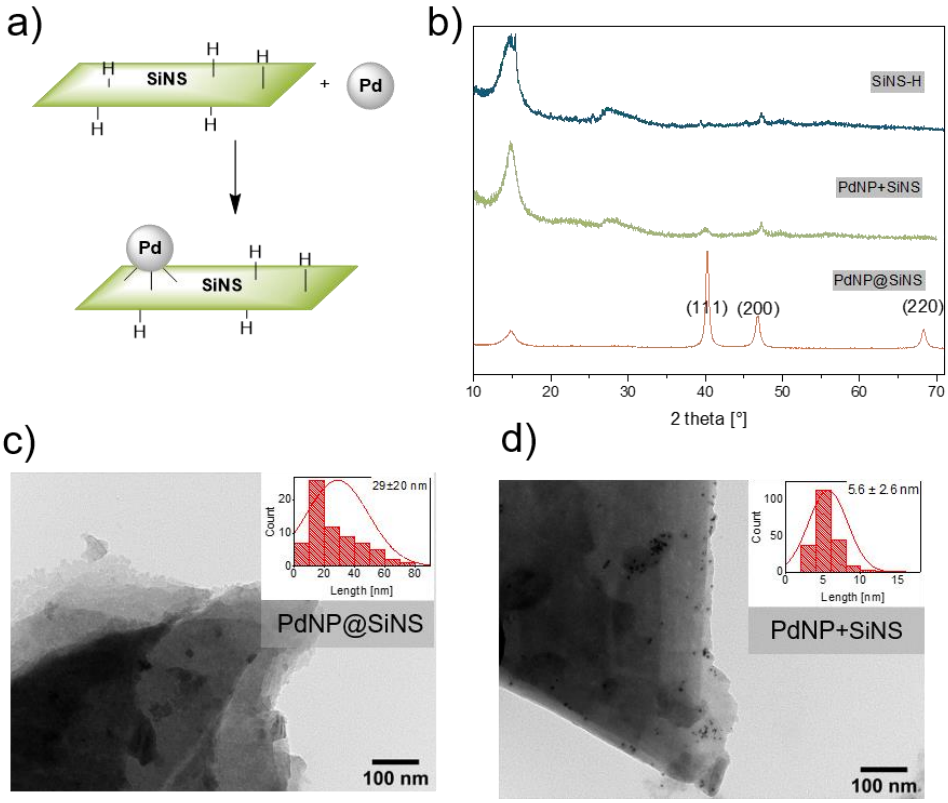


Figure 51 a) Synthesis scheme for PdNP+SiNS b) XRD patterns of SiNS-H, PdNP+SiNS, and PdNP@SiNS. TEM image of c) PdNP@SiNS d) PdNP+SiNS. The insets show the size distribution histogram evaluated from the TEM pictures.

### 4.4.3. Summary and Outlook

Catalytic nanomotors are nanoscaled particles consisting of a catalytic unit. The anisotropic fixation of the catalyst results in propulsion by utilizing the surrounding chemical fuel. The type of propulsion depends on the mechanism involved, which can cause an imbalance of charges (self-electrophoresis), concentration (diffusiophoresis), or gaseous products (bubble propellation). Nanomotors are designed to transport substances, so they are applied in drug delivery or as cargo carriers. The literature lacks a facile synthesis of nanomotors with SiNSs.

The chapter described the design of SiNS nanomotors with PdNPs propelling moieties by decomposing hydrogen peroxide fuel to, i.a., gaseous oxygen bubbles. At first, the concept of reducing $PdCl_2$ with SiH surface groups on the SiNS surface was investigated. The reaction parameters were optimized with less expensive CuNP model substrates because $Cu^{2+}/Cu^{+}$ was barely reduced by SiNSs lying at the edge of the SiNS standard electrode potential. Varying the silicon nanomaterial revealed that only etched and unfunctionalized SiNSs are applicable for reducing metal salts. Also, the reduction to metal nanoparticles is independent of the metal salt anion and runs stoichiometrically at reducing CuCl.

Literature-known approaches for anisotropic decoration of 2D nanomaterials were applied to our PdNP@SiNS nanomotor system with optimized parameters. All precise synthesis methods failed; specifically, interphase functionalization, deposition on glass substrates or carbon tape, and Pickering emulsions led to no or to a random movement of the nanomotors. Then, the synthesis concept was changed to add pre-reduced PdNPs in highly diluted to SiNSs. This very facile method yielded PdNP+SiNS nanomotors that exhibited directed and fast movement.

Further improvements on SiNS-based nanomotors are necessary on the path to the application, e.g., as cargo carriers: Exfoliation of SiNSs layer with tape and subsequent deposition of PdNPs could be a more precise alternative for small amounts of nanomotors. The structure of the SiNS nanomotors needs optimization by narrowing the size and shape distribution of SiNSs by density gradient centrifugation. Also, evaluation of the movement *via* a tracking software will yield valuable results. Ferromagnetic nanoparticles on SiNSs can lead to steering control of moving nanomotors under the influence of a magnetic field. However, the reduction potential of SiNSs is insufficient for synthesizing ferromagnetic nanoparticles. Therefore, adding pre-reduced and stabilized nanoparticles that adsorb to the SiNS surface would be the appropriate route.

## 4.5. SiNCs as Luminescent Layer in Si-LEDs

### 4.5.1. Introduction

SiNCs attract scientists to employ the material as an active layer in OLEDs, where the SiNCs must be luminescent under electric excitation. In principle, an OLED consists of the radiative recombination of excitons in the emissive layer and is enhanced by additional layers in the stack. The function of the respective layers was already described in detail in 2.3.

This is given for quantum-confined SiNCs with crystal dimensions below the exciton's Bohr radius, also called silicon quantum dots (SiQDs). SiQDs are applied as an emissive layer because of their biocompatible, semiconducting, and luminescent character. By adjusting the surface functionalization, the emission color of the SiNCs can be tuned. Loch *et al.* compared different surface functionalization methods of SiNCs and found that OLR instead of HS exhibited better Si-LED performance.[170] OLR capping causes a lower surface coverage, which decreases internal resistance. The experiments conducted in my Master thesis show that SiNCs functionalized with BuLi oxidized quickly because of the shorter side chain than HexLi.[231] It was expected that SiNCs capped with PhAcLi would yield pink-emitting Si LEDs since the corresponding SiNC solutions have pink emission color. Due to the low solubility and the limited deposition method, devices with comparable efficiency could not be prepared.

In contrast to other QD-LEDs, Si-LEDs have broad emission spectra of 130 nm-150 nm in common. Even with size separation methods like cascade centrifugation, conducted by Mastronardi *et al.,* only an FWHM of around 100 nm was achieved.[35] An alternative way is using Fabry-Pérot resonators that can narrow the emission linewidth. They consist of two reflecting mirrors, one totally and the other partially reflecting, creating a standing wave with emission obtained from excitonic recombination. Applying SiNCs as an emissive layer in such a Fabry-Pérot resonator LED, the emission linewidth is narrowed to 23 nm. However, lower EQE was observed due to the limited transmittance of the optical outcoupler.

This chapter describes the impact of the OLR chain length for SiNCs in Si-LEDs. The results are published in *Advanced Photonics Research*.[232] Colloidal SiNCs capped with sulfide groups exhibit excellent quantum yields of up to 50%.[203] Therefore the first known Si-LED with sulfide SiNCs was built. It was expected to achieve bright and effective devices with this surface group capping. Furthermore, the SiNC synthesis is upscaled to facilitate the reproducible fabrication of more devices. For this reason, an investigation of the capacitance-voltage behavior and application in Fabry-Pérot resonators is possible due to the high amount of LED devices.[233,234]

## 4.5.2. Results and Discussion

### 4.5.2.1. Si-LEDs with Varied Chain Lengths

SiNCs are functionalized by adding the respective alkyl lithium reagent overnight at room temperature. After workup and freeze-drying, OLR-capped SiNCs are characterized. As the particle size influences the Si-LED performance, hexyl-capped SiNCs are characterized by TEM and DLS. Figure 52a shows a TEM image of SiNCs functionalized with HexLi.

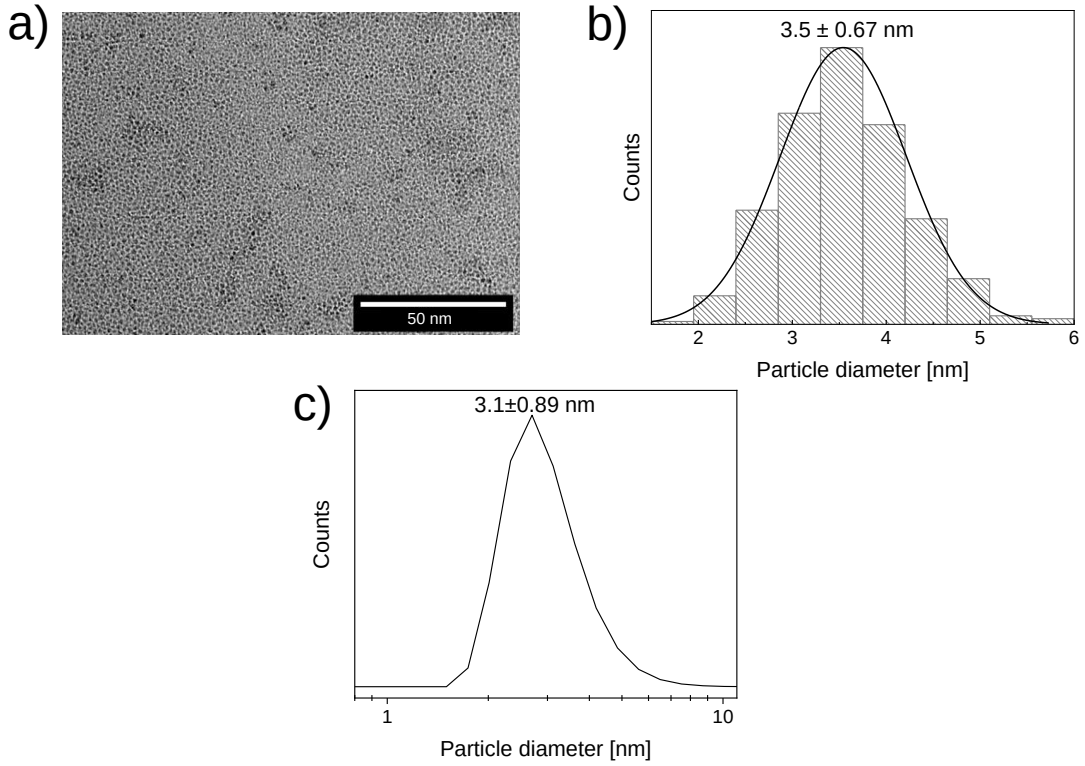


Figure 52 a) TEM image b) histogram of the particle size extracted from TEM pictures. Reprinted with permission of Ref.[232] c) DLS measurement of HexLi-capped SiNCs.

The particles exhibit an average diameter of 3.5±0.67 nm, as depicted in the histogram (Figure 52b). Also, DLS confirms the SiNC size in toluene, where the particles exhibit a hydrodynamic radius of 3.1±0.89 nm.

The previous characterization confirms that the SiNCs are roughly 3 nm, and the success of functionalization is investigated. The FT-IR spectra in Figure 53a show strong $CH_x$ stretching and deformation bands at 2900 $cm^{-1}$ and 1400 $cm^{-1}$ for all samples, indicating alkyl side chains. The Si-H stretching bonds at 2100 $cm^{-1}$ show that unfunctionalized surface groups are available. The intensity decreases from HexLi to DodecLi due to longer chain lengths, consistent with the OLR mechanism that allows 50% surface coverage at a maximum. Minor oxidation is observed at 1050 $cm^{-1}$.

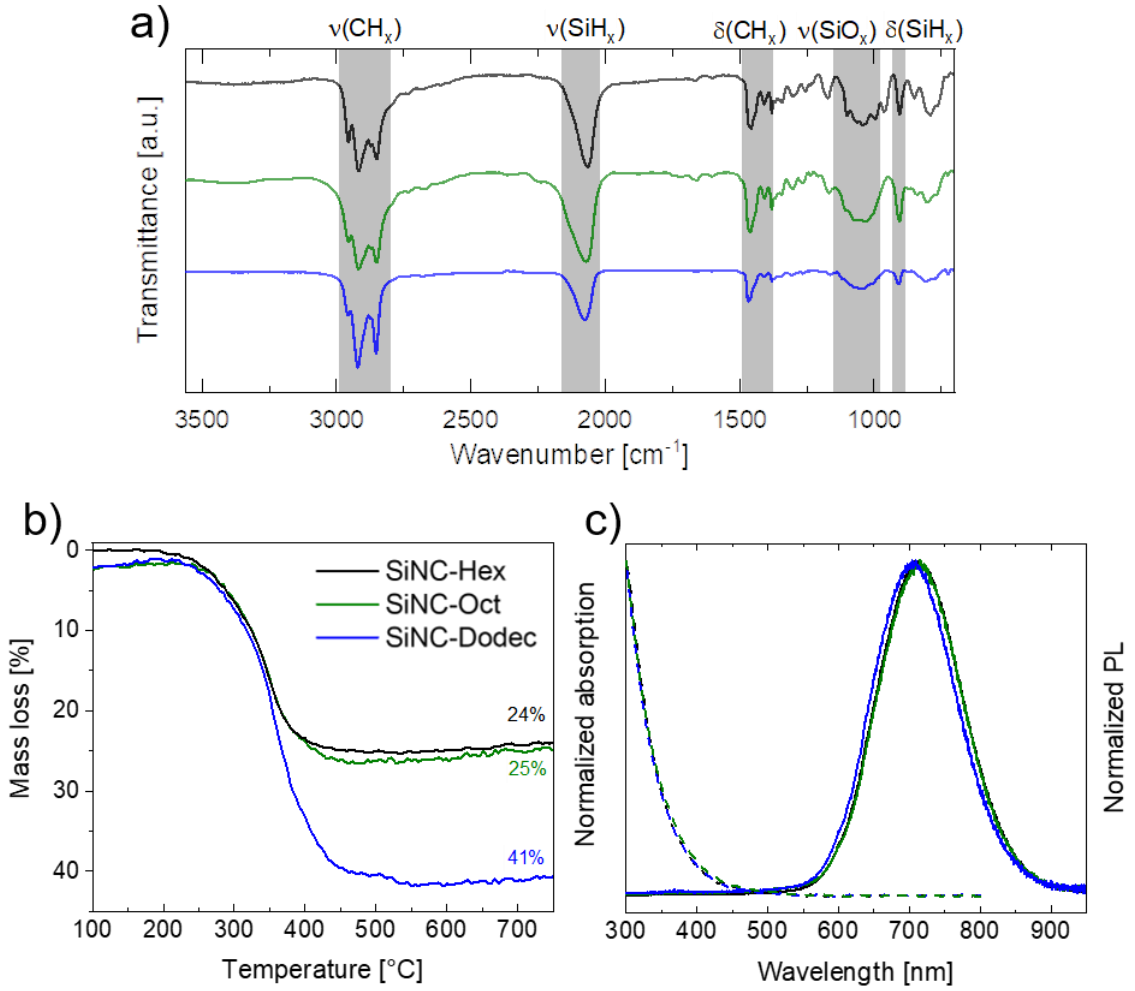


Figure 53 a) FT-IR spectra b) TGA c) UV/Vis and PL spectra of SiNCs capped with HexLi, OctLi, and DodecLi. Reprinted with permission of Ref.[232]. The legend in b) applies to all plots in the figure.

Thermogravimetric analysis (Figure 53b) shows a mass loss for all SiNCs samples between 300 and 400 °C. While DodecLi-capped SiNCs exhibit a mass loss of 41%, HexLi, and OctLi-capped SiNCs show a mass loss of 25%. These results show that the surface coverage is 40% for SiNC-Hex and SiNC-Dodec, while for SiNC-Oct, the lowest surface coverage of 33% is calculated. Due to the steric hindrance of the ligands, the values stay below the theoretical maximum.

All three sample solutions exhibit the same optical properties. The UV/Vis absorption spectra display a maximum of 300 nm. It indicates that the functionalized SiNCs are free of unsaturated substances or side products, which would show additional signals. A PL emission maximum of 710 nm with an FWHM of 140 nm is observed, revealing a size-dependent band gap emission. In conclusion, the three samples were successfully functionalized with the respective OLR and showed comparable properties.

These characterized SiNCs are implemented in optoelectronic devices. Si-LEDs are fabricated on an ITO anode with spin-coated PEDOT:PSS, PolyTPD interlayers, followed by the SiNCs

from the toluene solution (Figure 9). On top, a ZnO layer as a hole-blocking layer and silver as an anode material is deposited.

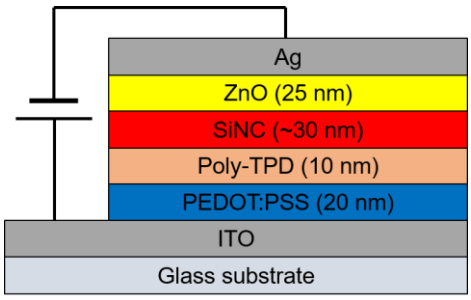


Figure 54: Stack architecture of the Si-LED. The colored layers are applied by spin-coating.

The built Si-LEDs are characterized electro-optically. The J-V characterization in Figure 55a depicts the absolute values for the current density J plotted against the applied voltage V. In the reverse diode direction, at negative voltages, J is influenced by pinholes.[235,236]

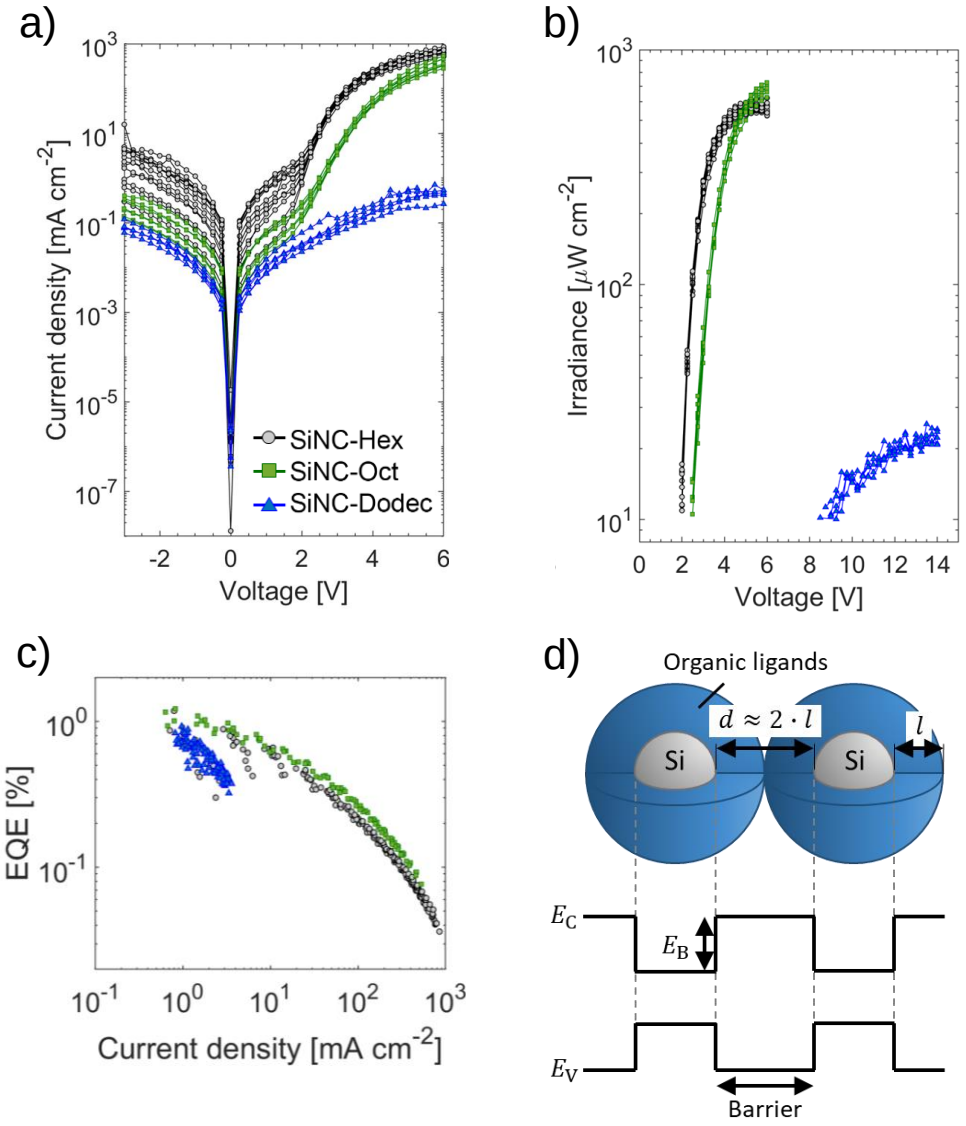


Figure 55: a) J-V characterization of Si-LEDs. The legend also applies to (b) and (c) b) Irradiance voltage characterization c) Characterization of EQE d) Scheme of the ligand energy barrier of two neighboured SiNCs. Reprinted with permission of Ref.[232].

The LED current spreads over one order of magnitude at a specific voltage for one surface functionalization, indicating small defects in the layers. In the forward direction for SiNC-Dodec-LEDs, the onset voltage lies around 8 V, defined by a turn-on irradiance of 10 µW/cm$^2$. LEDs with SiNC-Hex or SiNC-Oct exhibit a much lower onset voltage of 2 V and significantly higher current densities of ~300 mA/cm$^2$ in contrast to SiNC-Dodec with 3.5 mA/cm$^2$. The performance of LEDs with SiNC-Hex and SiNC-Oct is comparable with other Si-LEDs in literature, where photodiodes only apply lower turn-on irradiances, which are only detectable.[163,168,235]

The irradiance is plotted against the voltage from the turn-on point in Figure 55b, which shows that SiNC-Oct and SiNC-Hex exhibit maximum irradiances of 734 and 628 µW/cm$^2$, respectively. The LEDs with SiNC-Dodec performed worst with a maximum irradiance of 25 µW/cm$^2$. At 5 V, an irradiance crossover of LEDs with SiNC-Hex and SiNC-Oct is observed. It indicates a higher irradiance for Oct-LEDs because the localization of charge carriers in Hex-LEDs gets insufficient. Figure 46b depicts the EQE plotted against the current density for the three types of Si-LEDs.

The EQE lies for all three types ~1%. Single devices reach EQE values of 0.92% for SiNC-Dodec, 1.48% for SiNC-Oct, and 1.33% for SiNC-Hex. It is observable that lower EQE values stand for increased current densities, but SiNC-Oct exhibits the highest EQE for respective J.

Generally, the LEDs with SiNC-Hex and SiNC-Oct perform better than those with SiNC-Dodec. With longer surface groups, tunneling barriers increase and decrease charge transport. The scheme in Figure 55d depicts the distance of two capped SiNCs in correlation with the energy barrier of the ligands. The distances for SiNC-Hex, SiNC-Oct, and SiNC-Dodec in densely packed layers are determined to be 1.26 nm, 1.76 nm, and 2.74 nm, respectively, using *Chem 3D* version *19.1* software. When the ligand length increases, carrier mobility is hindered stronger due to a higher and wider tunneling barrier.[237] Also, the tunneling probability is higher for electrons than for holes resulting from a lower energy barrier for electrons. This can cause charge carrier imbalance, which further influences the recombination rate.

The different performances of the three types of Si-LEDs are explained by space-charge limited current (SCLC).[238] During the Si-LEDs' operation, the charge carriers can usually move freely to the other contact. If the case of defects, charge carriers remain localized and induce a space-charge, decreasing the device's current. Devices with OLR-SiNCs are known to exhibit such SCLC and a high number of trap states, but this effect is observed in LEDs with hydrosilylated SiNCs.[239–241] In conclusion, the dodecyl ligand attenuates the optical LED performance, whereas the octyl ligand exhibit enhancement.

The electroluminescence (EL) emission maximum is typically shifted to lower wavelengths for higher voltages. The EL spectra of the Si-LEDs are investigated further concerning FWHM and the blueshift of the peak. Figure 56a depicts the EL spectra of a Si-LED with SiNC-Hex at different applied voltages. With increasing voltages, the emission peak is blue-shifted by Δλ. For all three types of Si-LEDs, the deviation between the EL and PL emission maximum is plotted against the voltage in Figure 56c. All Si-LEDs show a decreasing peak difference for higher voltages, meaning only the smaller SiNCs are excited at low driving voltages. At the turn-on voltage, the maximum difference for LEDs with SiNC-Hex, SiNC-Oct, and SiNC-Dodec is at 2 V 71 nm, 2.5 V 56 nm, and 8.5 V 19 nm, respectively. With increased voltages, larger SiNCs are also excited and contribute to the emission spectrum, eventually assimilating to the PL spectrum. Devices with SiNC-Dodec reach this value at 12 V, while LEDs with SiNC-Hex and SiNC-Oct exhibit a residing deviation of 12 and 16 nm at their maximum emission at 6 V.

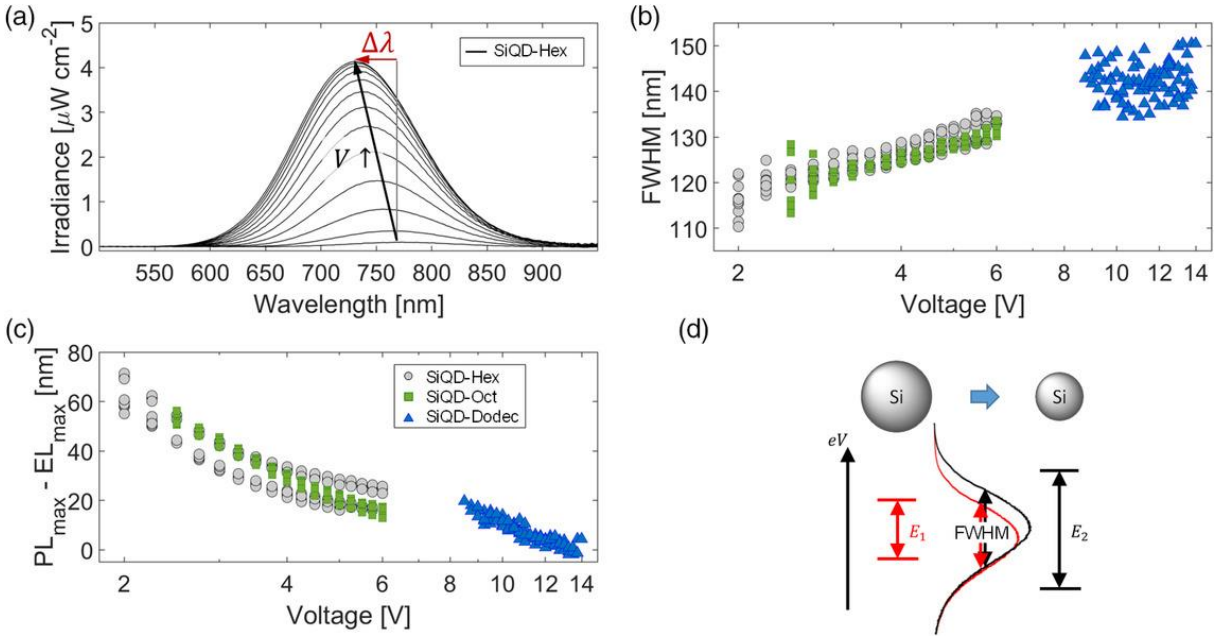


Figure 56: a) EL spectra of LEDs with SiNC-Hex b) FWHM broadening at higher voltages of Si-LEDs. c) Emission maximum deviation of Si-LEDs d) Scheme of both effects and influence of the SiNC size. Reprinted with permission of Ref.[232].

Due to the size distribution of SiNCs in the active layer, a broader FWHM of the EL spectra is observed (Figure 56b).[163,167,242] Additionally, the increased phonon concentration caused by the Joule heating effect at higher driving voltages intensifies the FWHM broadening.[243] LEDs with SiNC-Hex and SiNC-Oct start at 2.5 V with FWHM of 110 and 115 nm, respectively. The LEDs with SiNC-Dodec turn on later at 9 V and exhibit an FWHM of 130 nm. Due to noisy EL spectra, no clear FWHM trend for the SiNC-Dodec is determined.

In conclusion, Si-LEDs with SiNC-Hex are brighter, while SiNC-Oct is more efficient. SiNC-Dodec, as an active layer in Si-LEDs, performs less due to the longer side chain.

### 4.5.2.2. Si-LEDs with Sulfide-SiNCs

The Si-LEDs with OLR-capped SiNCs show a good performance. But increased luminance is necessary to reach higher EQE and compete with commercially available QD-LEDs. Sulfide-capped SiNCs (SiNC-S) are known to exhibit PLQY up to 50% and can be prepared by reaction with dichalcogenides at high temperatures.[203]

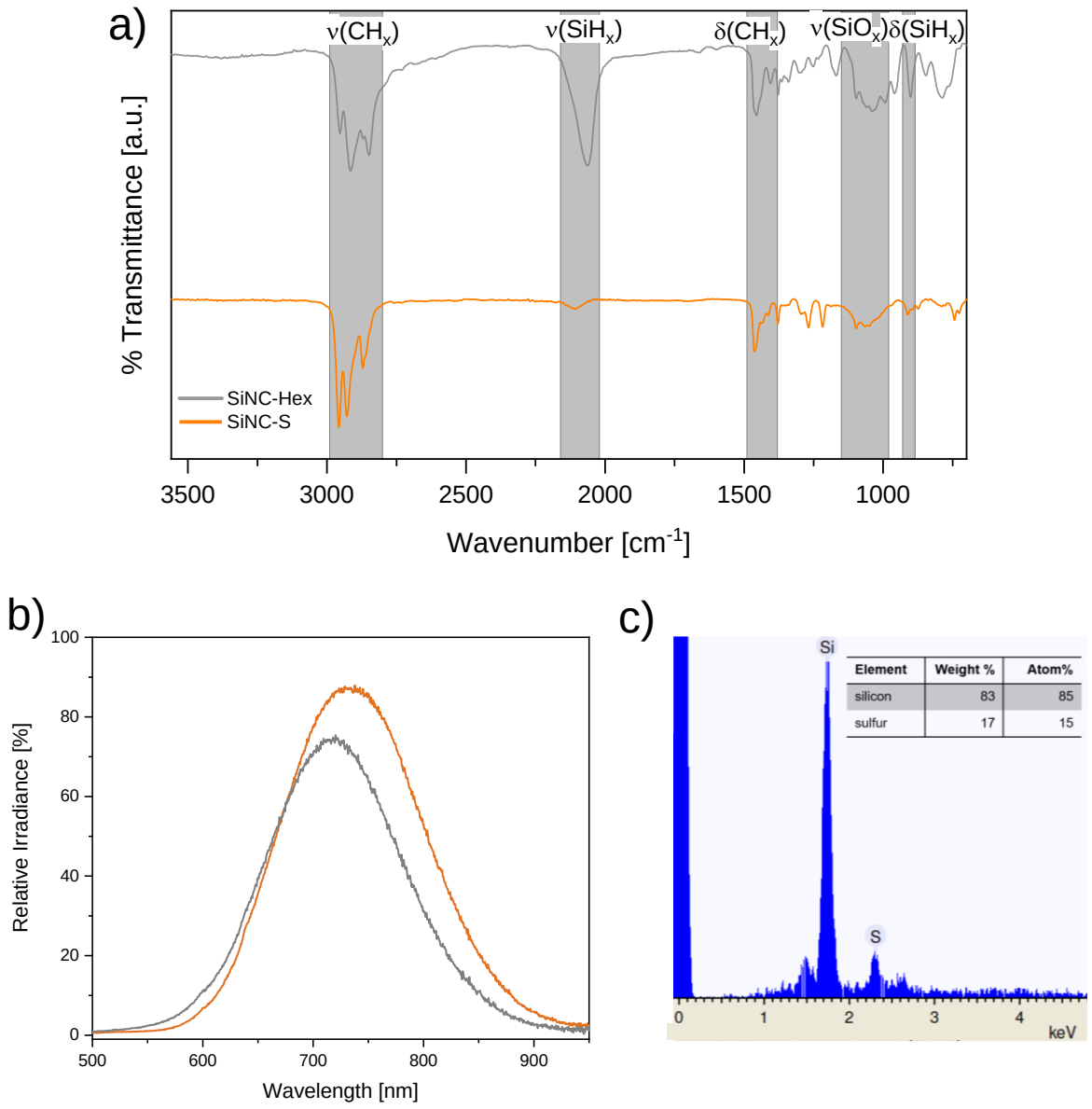


Figure 57 a) FT-IR spectra b) PL of sulfide SiNCs and SiNCs functionalized with HexLi for comparison. The legend applies to both plots. c) EDS spectrum of SiNC-S. The inset shows a table with weight% and atom% ratio.

Figure 57a SiNCs capped with butyl disulfide are characterized by FT-IR and compared with HexLi-capped SiNCs. Besides the signal bands for $SiO_x$ stretching at 1050 $cm^{-1}$, weak $SiH_x$ stretching at 2100 $cm^{-1}$ is displayed. For the butyl ligand, aliphatic $CH_x$ stretching and bending are observed at 2900 and 1450 $cm^{-1}$, respectively. Additionally, successful functionalization is confirmed by EDS. The spectrum in Figure 57a depicts that 83 wt% silicon and 17 wt% sulfur from the capping group are obtained. Generally, this setup cannot detect elements lighter than

sodium (e.g., carbon, oxygen, and fluorine). The PL spectra in Figure 57b confirms the expected optical properties. The SiNC-S exhibit a higher irradiance of up to 95% at the same concentration and irradiation intensity. The emission maximum is slightly redshifted due to another SiNCs batch with a different size distribution.

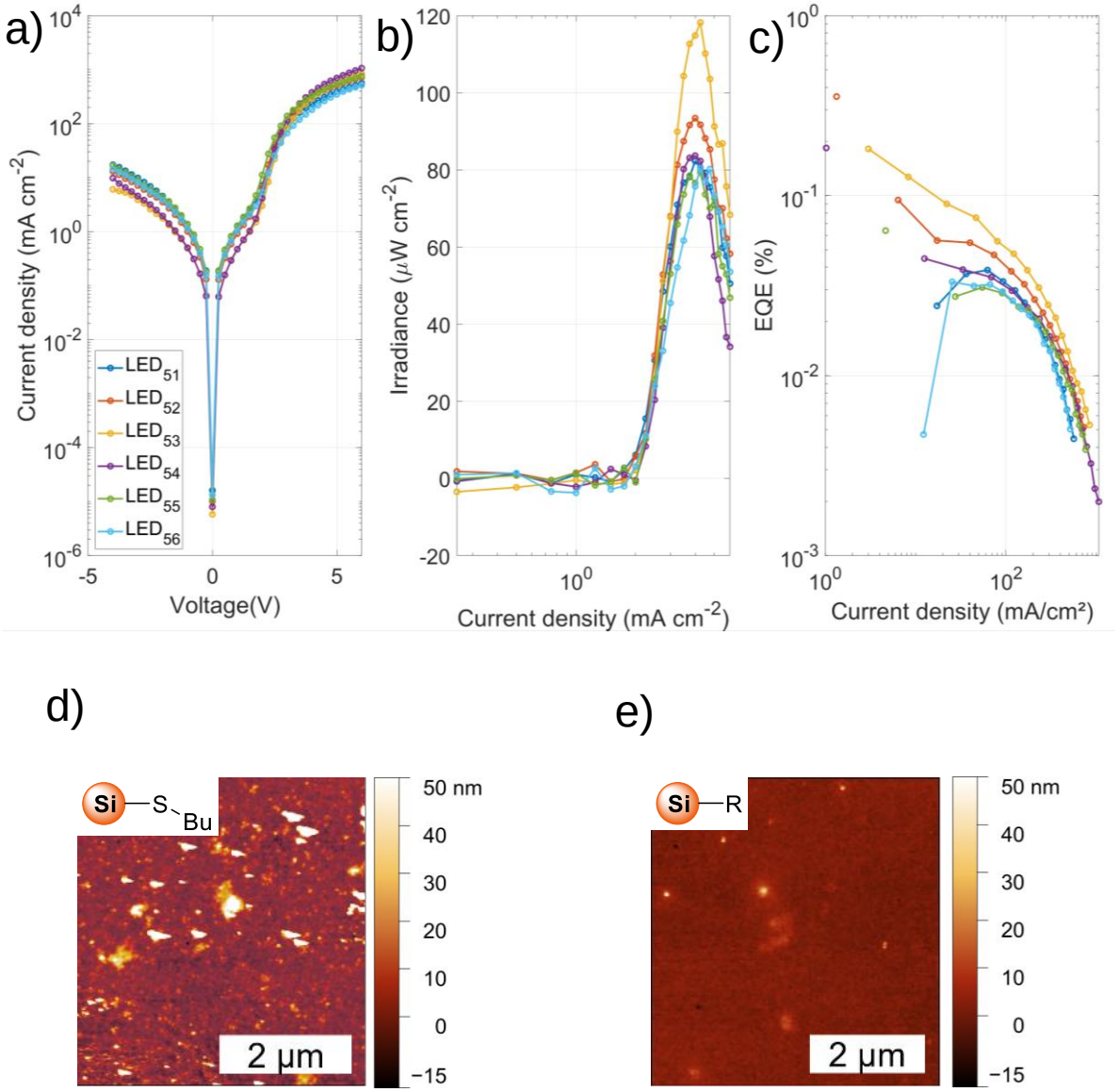


Figure 58: a) J-V characterization of Si-LEDs with SiNC-S. b) Irradiance current density characterization c) Characterization of EQE d) AFM image of SiNC-S layer e) AFM image of SiNC-Hex layer.

Si-LEDs with SiNC-S are characterized with the same method as the OLR-Si-LEDs. Figure 58a depicts the J-V analysis. A typical diode characteristic is observed. In the forward direction, the LEDs with SiNC-S exhibit a current density of up to several hundred mA/cm$^2$ at 6 V. The diode reaches its current density two orders of magnitude lower in the reverse direction. Generally, the devices with SiNC-S have a narrow deviation in performance. In Figure 58b, the Si-LEDs show an irradiance of up to 120 µW/cm$^2$, significantly lower than devices with SiNC-Hex. The EQE of Si-LEDs with SiNC-S lies around 0.1%, one magnitude lower than LEDs with SiNC-Hex.

The pressing question of these results is: Why perform Si-LEDs with SiNC-S lower; however, they show more intensive PL in solution? Therefore, the spin-coated layers of SiNC-S are compared to SiNC-Hex in AFM. In Figure 58d, the layers of SiNC-S exhibit many defects of ~100 nm height distributed over the whole measured area. The overall roughness is determined to be 2.7 nm. The defects can originate from polymer agglomeration, spin-coating defects, or foreign particles. For SiNC-Hex, the AFM shows that besides the defects on the micrometer scale, only a few spikes on the nanometer scale are present (Figure 58e). The lower number of defects explains the better performance of the SiNC-Hex in Si-LEDs than SiNC-S. Layer defects cause higher inner resistance and create hot spots in the device, leading to less stable LED operation.

#### 4.5.2.3. Further research

With the successful upscaling of the SiNC synthesis and enhanced functionalization with OLR, further research on applying SiNCs in optoelectronics is possible. Mock *et al.* observed a reproducible negative capacitance at Si LEDs upon a specific driving voltage.[234]

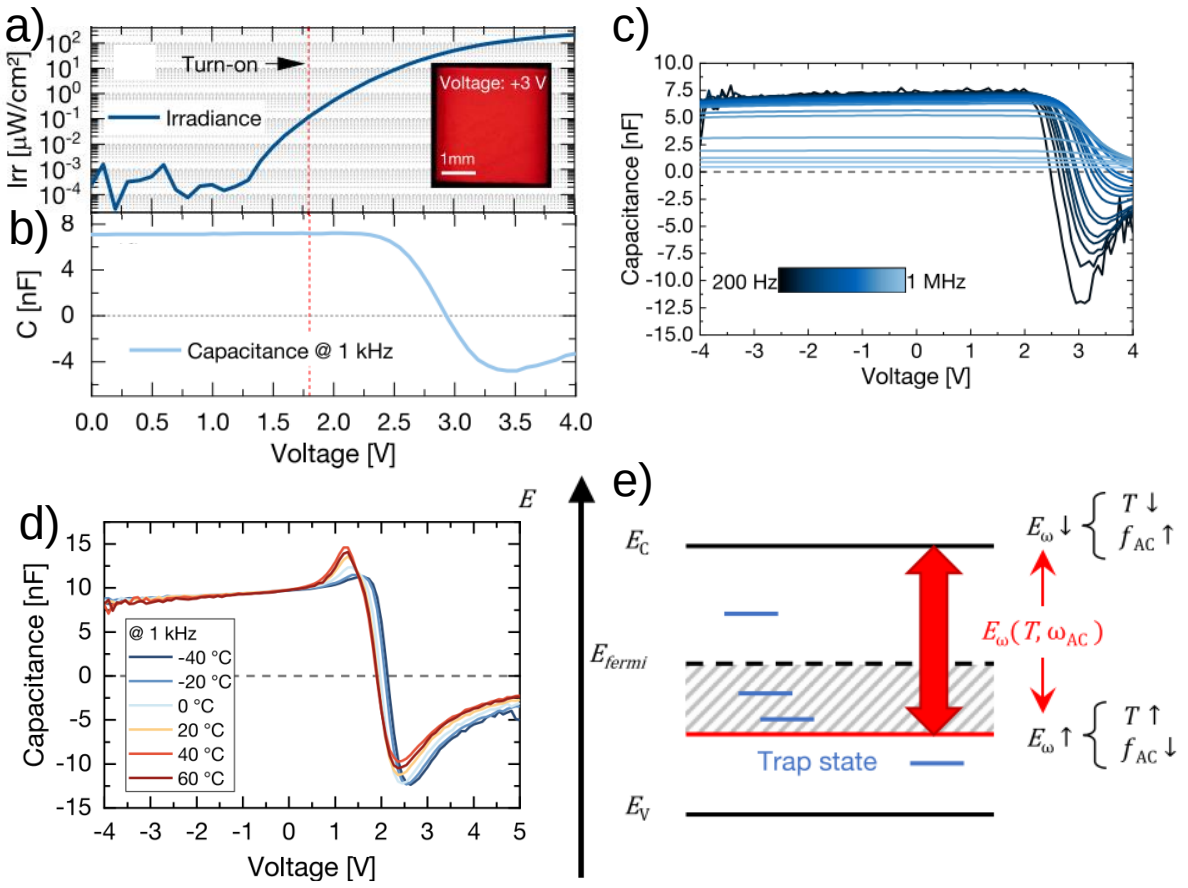


Figure 59: a) Irradiance-voltage characteristics of a Si-LED with SiNC-Hex. The turn-on-voltage is defined at 0.1 µW/cm². The inset shows a microscope picture of the respective LED at 3 V. b) Capacitance characteristics at 1kHz and room temperature. c) C-V characteristics of a Si-LED with SiNC-Hex with varied signal frequencies. d) C-V characteristics of a Si-LED with SiNC-Dodec at varied temperatures. Reprinted with permission from Ref.[234].

Negative capacitances are unusual for (opto)-electronic devices and were commonly explained by measurement or setup errors. Trap stated can contribute to the capacitance

measurement and cause a negative capacitance. The magnitude of the negative capacitance increases with lower voltage frequency or decreased temperatures (Figure 59c, d). Trap states can be occupied or emptied if the demarcation energy $E_\omega$ is large enough to cross the Fermi level. When this happens, trap states can be charged and discharged and cause a capacitance variation, eventually leading to negative capacitances.

The broad linewidth of Si-LEDs has already been discussed in chapter 4.5.2.1. Cheong *et al.* investigated SiNCs functionalized with OLR with the same optical properties and could narrow the linewidth by application in a Fabry-Pérot cavity.[233] The thickness of the $SiO_2$ layer and the top mirror Ag layer is varied for optimization of the stack architecture. Due to the resonance condition in this device, the blueshift observed at higher driving voltages for conventional Si-LEDs diminishes. However, brightness and efficiency were sacrificed in this setup for the narrowed linewidth. Further research should focus on more transparent outcoupling materials like $WO_3$/W.[244]

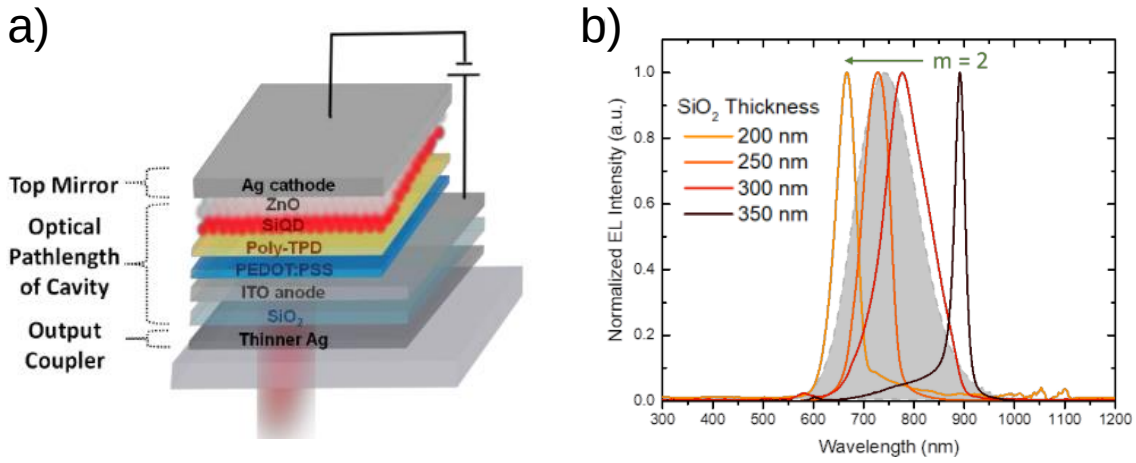


Figure 60: a) Stack architecture b) EL spectra of a Fabry-Pérot resonator Si-LEDs with varied $SiO_2$ layer thicknesses. Reprinted with permission from Ref.[233].

### 4.5.3. Summary and Conclusion

SiNCs are a non-toxic and abundant alternative to commonly used heavy metal quantum dots in optoelectronics, like displays. In this chapter SiNCs with two different surface functionalizations were applied as a luminescent layer in Si-LEDs.

In the first study, the chain length of the OLR ligands was varied from hexyl and octyl to dodecyl. While SiNC-Hex exhibited the highest irradiance, SiNC-Oct showed the highest EQE of 1.48%. Longer ligands caused a higher potential barrier between the SiNCs and reduced the charge transport within the active layer. Also, space charges created by defects decreased the performance by SCLC.

In the second study, sulfide-capped SiNCs were applied in Si-LEDs for the first time. Their excellent optical properties in colloidal dispersions allowed the assumption of enhanced LED performance. The devices performed with a severely lower efficiency, mainly caused by small

pin holes in the spin-coated sulfide-SiNCs layers. AFM images showed a higher roughness, which might reduce the conductivity and efficiency of these Si-LEDs.

With CV measurements, insights into the transition mechanisms of SiNCs in Si-LEDs were achieved. The study revealed negative capacitances for Si-LEDs caused by the demarcation energy effect. Thus, such trap-mediated recombinations of sub-bandgap energy states led to an equilibrating current that lags behind the voltage.

To narrow the emission spectra line width, an engineering solution was found. The application in Fabry-Pérot cavities achieved the expected lower FWHM. However, lower EQE and brightness were observed, so a more transparent outcoupler needs to be found in the future.

# 5. Summary and Conclusion

The first project in chapter 4.1 deals with the dehydrogenative coupling of silicon nanocrystals (SiNCs) and silicon nanosheets (SiNSs) with silanes to enlarge the silicon network, whereby the semiconducting properties were expected to be enhanced. The focus was on initiation with boron-containing Lewis acids and yielded in oxidized materials due to the lack of Si-H bond polarization. Since dehydrogenative coupling was unsuccessful, evidence of improvement in semiconducting properties was not possible. Other mechanisms for Si-Si bond formation on SiNCs, e.g., halogen substitution or silicon Grignard reagents, need to be considered in the future.

Trityl salt-induced functionalization of SiNCs with nucleophiles is investigated in the second project (chapter 4.2). After screening several nucleophiles, alcohols, and thiols yielded the highest surface coverage (up to 54%). Furthermore, the fluorination of the SiNC surface can be induced by activating trityl tetrafluoroborate or trityl hexafluorophosphate in the absence of a nucleophile. This outcome was verified by observing no agglomeration of SiNCs through dynamic light scattering and observing no surface charge through neutral zeta potential. Molecular model compounds mimicking SiNC surface groups like Si-H, Si-O-Si bridges, and Si-Si backbone revealed unselective fluorination of the surface. Optical characterization like photo luminescence lifetimes or absolute quantum yield of the activated or functionalized SiNCs needs to be performed and will decide on the potential applicability for bioimaging or optoelectronic devices.

The advancement of the Janus SiNC synthesis with organolithium reagents broadens the scope of surface moieties like ethynylaryls or phenyl groups. Photoluminescence measurements at Janus SiNCs functionalized on one side with conjugated surface groups reveal redshifted emission of 45 nm in contrast to alkyl-capped SiNCs. Also, the synthesis method is widened to 8 nm Janus SiNCs, overcoming the limitation of the former synthesis route, which is only applicable to SiNCs smaller than 5 nm. Proof of anisotropy, synthesis of amphiphilic Janus SiNCs, and optical characterization of self-assembled monolayers are subjects of future research.

Another project introduces to SiNSs decorated with metal nanoparticles prepared by the reduction of metal salts by Si-H surface groups (chapter 4.4). Reaction parameters were investigated in detail for copper nanoparticles. Decoration with palladium nanoparticles yields the first SiNS-based nanomotors. Their random motion is changed to directed movement by adding pre-reduced palladium nanoparticles to the SiNSs. Future optimization includes magnetic components like iron oxide nanoparticles to ensure directional movement control by applying a magnetic field.

The most promising field of application for luminescent silicon nanomaterials is optoelectronic devices like light-emitting diodes (LEDs). The fifth project investigates the application of SiNCs functionalized with sulfides or different organolithium reagents varying alkyl chain lengths in chapter 4.5. While hexyl-capped SiNCs revealed an irradiance of 748 µW/cm$^2$, octyl-capped SiNCs showed the highest external quantum efficiency of 1.48%. Sulfide-SiNCs exemplify that high quantum yields (~50%) do not guarantee LED performances above average Si-LEDs. Atomic force microscopy images reveal defects in the SiNC layer, originating from poor processability. The upscale of SiNC synthesis ensured an easy and safe procedure and reproducible SiNC properties using conventional lab equipment. Collaborative research enabled more precise Si-LED characterization and investigation of capacitance-voltage characteristics. Also, applying SiNCs in Fabry-Pérot cavities is possible with narrowed line width emission; however, the devices showed low efficiency. Optimizing the stack architecture of LEDs, especially on the transport layers, is the subject of future research. To achieve Si-LEDs with various emission colors, SiNCs with different surface groups, e.g., amines or conjugated groups, should be investigated. Upscaling into an industrial scale of Si-LEDs still needs gas-phase synthesis of SiNCs.

# 6. Experimental Procedures

All experiments, including air-sensitive materials, are conducted and used under Schlenk conditions. Purchased chemicals are used as received unless otherwise specified. TrBCF[245], polymeric hydrogen silsesquioxane (HSQ)[33], and PhAcLi[84] are synthesized according to procedures known in the literature. 4-Decyldiazobenzene tetrafluoroborate[50] and tris(trimethylsilyl)silyl potassium[246] are taken from the chair and synthesized according to procedures known in the literature. Dry solvents are obtained from an *MBraun SPS 800 solvent purification system* with Argon 5.0 as the operating gas. Acetone, acetonitrile, and 1,2-dichlorobenzene are dried over activated aluminum oxide and molecular sieve.

## 6.1. Preparation of the Silicon Nanomaterials

### 6.1.1. Synthesis of Silicon Nanocrystals

#### 6.1.1.1. Synthesis of the SiNC/ $SiO_2$ Composite

For the synthesis of 3 nm SiNC composite HSQ (7 g) is weighed in a quartz reaction boat, heated from ambient to a peak processing temperature of 1100 °C at 18 °C/min in a *Nabertherm RD 50/250/12 furnace* with quartz working tube under an atmosphere consisting of 5% $H_2$ and 95% $N_2$. The sample is kept at 1100 °C for 1 h. After cooling to room temperature, the resulting solid is ground into a fine brown powder using a mortar and pestle. The composite is dispersed in ethanol and further ground in a shaker for 24 h with high-purity silica beads using a *WAB* Turbula mixer. The resulting SiNC/$SiO_2$ composite is vacuum-dried. Composites with 6, 9, or 20 nm SiNC are prepared analogously to this process, with the surface temperature increased to 1200, 1300, or 1400 °C.

#### 6.1.1.2. Liberation of Hydride-Terminated SiNC

300 mg of the SiNC/$SiO_2$ composite is transferred to an ethylene-tetrafluoroethylene (ETFE) beaker equipped with a PTFE-coated stir bar. Ethanol (3 mL) and water (3 mL) are then added and stirred to form a brown suspension, followed by adding 3 mL of 49% aqueous HF solution. After 30 min of etching, the color of the mixture turns yellow. Hydride-terminated SiNCs are subsequently extracted from the aqueous layer into ca. 30 mL of toluene by multiple (e.g., 3 × 10 mL) extractions. The SiNC suspension in toluene is centrifuged in an ETFE centrifuge tube at 9000 rpm for 4 min. Extracted particles are redispersed in 5 mL dry acetone or 5 mL dry toluene and centrifuged once more to remove residual water and ethanol.

**Functionalization of SiNCs *via* Hydrosilylation of Alkenes**

Freshly etched hydride-terminated SiNCs (from 300 mg Si/$SiO_2$ composite) are reacted with 1-hexene (0.5 ml, 4 mmol) or 1-dodecene (0.5 ml, 2.25 mmol) in 2 mL toluene and 10 mg AIBN in a dried Schlenk flask and degassed three times. The mixture is stirred for 15 h at 75 °C. The functionalized particles are precipitated from toluene with 12 mL 1:1 methanol/ethanol mixture

and centrifuged in ETFE tubes for 10 min at 9000 rpm. They are then resuspended in a minimal amount of toluene and precipitated again with 12 mL of 1:1 methanol/ethanol mixture. The precipitation-centrifugation-redispersion cycle is performed a total of three times. The functionalized and purified SiNCs are dispersed in diethyl ether for characterization and freeze-dried in 2 mL benzene.

## 6.1.2. Synthesis of Silicon Nanosheets

### 6.1.2.1. Synthesis of the Zintl Phase $CaSi_2$

The Zintl phase $CaSi_2$ is prepared from a stoichiometric amount of calcium and silicon pressed to a pellet which is melted with an arc furnace in a glove box. The resulting silver nugget is ground in an agate mortar. The gross solid is pressed into a pellet again, and the procedure is repeated twice.

### 6.1.2.2. Exfoliation from $CaSi_2$

1 g of $CaSi_2$ is added to a 100 mL flask of precooled to -30 °C concentrated hydrochloric acid (37% aq.). The exfoliation is completed after 7 d at -30 °C and aided by gently shaking the flask. The resulting yellow flakes are filtered using a Schlenk frit and washed with dry acetone to remove residual calcium dichloride. The yellow solid is dried under vacuum and stored in a glove box. A typical yield from 1 g of $CaSi_2$ is 600 mg SiNS flakes.

### 6.1.2.3. Etching of the Silicon Nanosheets

30 mg of SiNS flakes are dispersed in 2 mL dry, degassed ethanol and ultrasonicated for 5 min to break up large agglomerates. The dispersion is transferred to a PTFE tube, adding 1 mL of water and 0.25 mL of HF (48% aq.). The orange suspension turns bright yellow immediately. After 15 seconds, dichloromethane (~5 mL) is added, and the container is gently shaken. The etched SiNS-H is located in the organic phase. The SiNS-H are extracted and transferred into a PTFE centrifuge tube using a polypropylene pipette. This process is repeated until all nanosheets are collected. The tube is filled with toluene to enhance the precipitation of the SiNS-H. If the amount of dichloromethane exceeds the amount of toluene, the dispersion is split into two tubes and filled with toluene. After centrifugation of suspensions (9000 rpm, 4 min), the SiNS-H pellet is dispersed in dry acetone, centrifuged (9000 rpm, 4 min), redispersed in dry toluene, and centrifuged again (9000 rpm, 4 min). The SiNS-H are now dispersed in dry reaction solvent or dry benzene for freeze-drying. The etching procedure typically yields 20 mg of SiNS-H.

### 6.1.2.4. Functionalization of SiNSs *via* Hydrosilylation of Alkenes with AIBN

20 mg of freshly etched hydride-terminated SiNSs are reacted with 0.5 mL of the respective 1-alkene, 2 mL toluene, and initiator 10 mg AIBN in a dried Schlenk flask and degassed three times. The mixture is stirred for 15 h at 75 °C. The functionalized SiNSs are washed with

toluene and centrifuged in ETFE tubes for 2 min at 4000 rpm. This is performed three times in total. The functionalized and purified SiNSs are dispersed in toluene for characterization and freeze-dried in 2 mL benzene afterward.

#### 6.1.2.1. Functionalization of SiNSs *via* Hydrosilylation of Alkenes with BIP

20 mg of freshly etched hydride-terminated SiNSs are reacted with 0.5 mL of the respective 1-alkene, 2 mL EtOAc, and 7 mg of BIP in a dried Schlenk flask and degassed three times. The mixture is stirred for 15 h at room temperature. The functionalized SiNSs are washed with EtOH and toluene and centrifuged in ETFE tubes for 2 min at 4000 rpm. This is performed three times in total. The functionalized and purified SiNSs are dispersed in toluene for characterization and freeze-dried in 2 mL benzene afterward.

## 6.2. Instruments Information

**FT-IR** measurements are performed with liquid nitrogen-cooled *Bruker Vertex 70 FT-IR*. 32 scans are measured in a wavelength region of 4000 $cm^{-1}$ to 700 $cm^{-1}$ with a resolution of 4 $cm^{-1}$. Measurements are performed by a *Platinum ATR* unit from *Bruker*, and the spectra are monitored by the software *Opus* and reported in transmission mode.

**TGA** measurements are conducted with freeze-dried samples in the glovebox on a *Netzsch TG 209 F 1 Libra* with a heat rate of 10°K/min from 30 to 600 °C under an Argon flow (4.8) of 20 mL/min in aluminum oxide pans. The data are evaluated by the software *Netzsch Proteus 6*. In determining the **surface coverage**, it is assumed that the residual mass is pure silicon nanomaterials and that the functionalized substrates cause all the mass loss. For 3 nm SiNCs, an icosahedral model exhibits the molecular formula of $Si_{1100}H_{300}$ and a molecular weight M of 30800 g*$mol^{-1}$.[247]

$$SC = \frac{M(SiNC)}{300 * M(Substrate)} * \frac{\Delta m}{1 - \Delta m} \quad (5)$$

The calculation is based on the assumption that organic ligands decompose into gaseous substances. These cause the observed mass loss Δ*m* and the bare silicon nanomaterial remains. For SiNSs, it is assumed that the molecular formula is $(SiH)_n$. Transferring equation (5) to the model of SiNSs, the resulting equation (6) for the surface coverage is:

$$SC = \frac{M(SiH)}{M(Substrate)} * \frac{\Delta m}{1 - \Delta m} \quad (6)$$

**$^{1}$H, $^{13}$C, $^{31}$P,** and **$^{29}$Si-NMR** spectra are obtained on an *ARX-300* or *AV-400HD* from *Bruker* at 300 K. The chemical shifts $\delta$ are reported in ppm relative to the residual proton or carbon signal of the deuterated solvent. Samples for **solid-state NMR** are prepared in a 4 mm

double-resonance (H-X) Bruker MAS NMR probe. The $^{29}$Si-CPMAS and hpdec spectra are recorded on *Avance III HD 400* from *Bruker* at a rotation frequency of 12 Hz.

**Photoluminescence** spectroscopy is performed with an *AVANTES AVA-Spec 2048* spectroradiometer coupled with the light source (365 nm) Prizmatix (LED current controller) and *Avantes CUV-FL-UV/VIS* cuvette holder. Measurements are taken in a quartz glass cuvette with dimensions of 40 mm × 10 mm × 1 mm. Measurements are recorded with a 90° angle between the light source and the spectrometer. The data are recorded with *AVA-Soft 8* software. Unless otherwise stated, toluene is used as the solvent for all the samples.

**Absolute quantum yields** are obtained using a *Hamamatsu Quantaurus-QY C11347* spectrometer equipped with an integrated sphere.

Particle size determination is determined with **dynamic light scattering** on a *Malvern Zetasizer Nano ZS*. A quartz cuvette (40 mm × 10 mm × 10 mm) and toluene as a solvent are used. Before the measurement, the solution is filtered over a 0.2 µm PTFE syringe filter. The data are averaged over ten measurements. For **ζ-potential** measurements, a dip cell setup is used, and the data are averaged over three sets of up to 100 measurements.

**AFM** images are recorded in tapping mode using an *Asylum Research AFM MFP-3D* from *Oxford Instruments*. All AFM images are analyzed with the software *Gwyddion*.

**Scanning electron microscopy** imaging is performed using a *Hitachi TM-1000* tabletop microscope operated at 200 kV. EDX spectra are obtained using a *SwiftED-TM* EDX unit (*Oxford Instruments*) attached to the tabletop microscope. SEM images are also recorded on an *FE-SEM JSM 7500F* from *Jeol* at an accelerating voltage of 1 kV.

**Light microscopy** images are captured with a *Panthera TEC* from *Motic* at magnifications of 50×, 100×, 200× and 500× and evaluated with *MicroCamLab II*.

**XRD** patterns are recorded on a silicon wafer by a benchtop X-ray powder diffractometer *MiniFlex 600-C* from *Rigaku* equipped with a Cu X-ray tube and a high-speed one-dimensional detector *D/teX Ultra,* and a Kβ-filter.

**XP spectra** are recorded on a *VersaProbe III* X-ray photoelectron spectrometer from *PHI* with a monochromatic Al Kα source at 50 W. Samples are prepared by drop-casting toluene solutions onto a copper foil. High-resolution spectra are obtained using an analyzer pass energy of 20 eV and a step of 0.1 eV. A pass energy of 160 eV and a step of 0.3 eV is used for survey spectra. Spectra are calibrated to the aliphatic carbon component of the C 1s binding energy of adventitious carbon (284.8 eV). The signal is fit to appropriate spin–orbit pairs using *CasaXPS* software from *VAMAS* with a Shirley-type background.

**UV/VIS-spectroscopy** is conducted with a *Varian Cary 50* scan spectrometer within the 200 to 800 nm range.

**Bright-field TEM** images are obtained using a *JEOL-2012* electron microscope equipped with LaB6 filament and operated at an accelerating voltage of 200 kV. ImageJ software calculates particle size distribution by counting at least 200 particles (Version 1.49).

## 6.3. Homonuclear Dehydrogenative Coupling

### 6.3.1. DHC of Silicon Nanosheets with Silane (First reactions)

12 mg of SiNS-H (from etching 15 mg of SiNSs according to 6.1.2.3) are dispersed in 2 mL dry solvent, and 0.5 mmol of the tertiary silane (trioctyl silane or triethyl silane) is added. Depending on the experiment, the initiator is added respectively to the amounts used to activate HS or DHC in the literature (Table 2). The dispersion is degassed *via* three freeze-pump-thaw cycles and stirred at the respective temperature for 16 h. The resulting reaction mixture is centrifuged (9000 rpm, 4 min). The supernatant is discarded, and the pellet is re-dispersed. The precipitation/dispersion cycle is repeated twice to yield purified functionalized SiNSs.

Table 2: Reaction conditions of the first DHC experiments with 12 mg SiNS-H each.

| | m [mg] | n [µmol] | solvent | T [°C] |
|---|---|---|---|---|
| therm | - | - | Tol | 100 |
| AIBN | 15 | 91 | Tol | 80 |
| Iodonium | 7,0 | 13,0 | EtOAc | RT |
| cat | 6,0 | 6,0 | Tol | 50 |

### 6.3.2. Lewis Acid Induced DHC of Silicon Nanocrystals

**DHC of silicon nanocrystals with different Lewis acids**

150 mg of SiNC/$SiO_2$ composite is etched according to 6.1.1.2. and redispersed in 1 mL dry toluene, and 0.1 mL of hexyl silane is added. 0.2 mmol of the respective LA is added dropwise from a 1M solution ($BH_3$·THF, $BH_3$·$SMe_2$, $BF_3$·$Et_2O$) or BCF as a solid. The resulting reaction mixture is centrifuged (9000 rpm, 4 min). The supernatant is discarded, and the pellet is re-dispersed. The precipitation/dispersion cycle is repeated twice to yield purified functionalized SiNCs.

**DHC of Silicon Nanocrystals with Different Silanes**

400 mg of SiNC/$SiO_2$ composite is etched according to 6.1.1.2. and redispersed in 1 mL dry toluene, and 0.4 mmol of the respective silane is added. 0.2 mL of $BH_3$·THF (1M) is added dropwise. The dispersion is degassed *via* three freeze-pump-thaw cycles and stirred at 100 °C for 16 h. The resulting reaction mixture is centrifuged (9000 rpm, 4 min). The supernatant is discarded, and the pellet is re-dispersed. The precipitation/dispersion cycle is repeated twice to yield purified functionalized SiNCs.

### 6.3.3. Lewis Acid Induced Functionalization with Silicon Nanosheets

For the NMR test reaction, hexyl silane and $BH_3$·THF are dissolved in 1 mL toluene in equimolar amounts of 0.25 mmol, and then the mixture is heated to 100°C for 16 h. The solvent and LA residues are removed *in vacuo,* and the resulting solid is measured in $CDCl_3$. For the other reactions, 12 mg of SiNS-H (from etching 15 mg of SiNS) are redispersed in 2 mL dry toluene and mixed with 0.8 mmol hexyl silane. 0.8 mmol BH3·THF (1M) is added for the LA initiation. The samples are treated analogously to the test reaction above.

## 6.4. Trityl induced Functionalization

### 6.4.1. Initial Experiments

**Investigation of different nucleophiles for SiNC-functionalization**

150 mg of SiNC/$SiO_2$ composite is etched according to 6.1.1.2., redispersed in 2 mL dry dichloromethane, and 70 mg of $TrPF_6$ (0.2 mmol, 5 eq.) is added. Subsequently, 1 mmol of the respective nucleophile is added. The dispersion is degassed *via* three freeze-pump thaw cycles and stirred at room temperature for 16 h. The resulting reaction mixture is centrifuged (9000 rpm, 4 min). The supernatant is discarded, and the residue is redispersed in acetonitrile. The precipitation/dispersion cycle is repeated twice to obtain the purified functionalized SiNCs, which are freeze-dried in benzene before characterization.

**Investigation of different group IV nucleophiles**

150 mg of SiNC/$SiO_2$ composite is etched according to 6.1.1.2., redispersed in 2 mL dry toluene, and mixed with 60 mg of TrBCF (0.6 mmol, 3 eq.). 1 mL of the respective nucleophile is added dropwise from a 1M solution in dry toluene. The dispersion is degassed *via* three consecutive freeze-pump-thaw cycles and stirred at room temperature for 16 h. The resulting reaction mixture is centrifuged (9000 rpm, 4 min). The supernatant is discarded, and the residue is redispersed in a small amount of toluene and precipitated in methanol. The precipitation/dispersion cycle is repeated twice to yield the purified functionalized SiNCs, which are freeze dried in benzene before characterization.

### 6.4.2. Optimization of Reaction Parameters

**Variation of the chain length of primary alcohols for SiNC surface functionalization**

150 mg of SiNC/$SiO_2$ composite is etched according to 6.1.1.2., redispersed in 3 mL dry toluene, mixed with 13 mg of TrBCF (0.02 mmol, 0.6 eq.) and 1 mL of the respective alcohol. The dispersion is degassed *via* three consecutive freeze-pump thaw cycles and stirred at room temperature for 16 h. The resulting reaction mixture is centrifuged (9000 rpm, 4 min). The supernatant is discarded, and the pellet is re-dispersed. The precipitation/dispersion cycle is

repeated twice to yield the purified functionalized SiNCs, which are freeze dried in benzene before characterization.

**Comparison of Secondary and Primary Amines**

200 mg of SiNC/$SiO_2$ (9nm) composite is etched according to 6.1.1.2, redispersed in 3 mL dry toluene and 22 mg of TrBCF (0.02 mmol, 1 eq.), as well as 1 mL of the respective amine, is added dropwise. The suspension turns brighter after addition and is degassed *via* three freeze-pump-thaw cycles and stirred at 40 °C for 16 h. The resulting reaction mixture is centrifuged (9000 rpm, 4 min). The supernatant is discarded, and the pellet is re-dispersed. The precipitation/dispersion cycle is repeated two times to yield purified functionalized SiNCs which are freeze dried in benzene for characterization.

**Variation of the trityl counterion for hydride abstraction of SiNCs**

200 mg of SiNC/$SiO_2$ (9nm) composite is etched according to 6.1.1.2, redispersed in 1 mL dry dichloromethane, and 0.05 mmol, 2 eq. of the respective trityl salt is added. The dispersion is treated for 15 min with ultrasonication. Then, 1 mL of dodecanethiol is added. The suspension is degassed *via* three freeze-pump-thaw cycles and stirred at 40 °C for 16 h. The resulting reaction mixture is centrifuged (9000 rpm, 4 min). The supernatant is discarded, and the pellet is re-dispersed. The precipitation/dispersion cycle is repeated two times to yield purified functionalized SiNCs which are freeze dried in benzene for characterization.

To conduct the NMR experiments, 100 mg of SiNC/$SiO_2$ (3 nm) composite is etched following the procedure outlined in section 6.1.1.2. The resulting material is then redispersed in 1.5 mL of dry dichloromethane, followed by adding 0.5 mL of dodecanethiol. The suspension is degassed *via* three freeze-pump-thaw cycles and stirred at room temperature for 16h. The opaque suspension is separated and transferred to three vessels, each containing 2 eq. (0.05 mmol) of the respective trityl salt. While the solution with $TrPF_6$ turns clear after 30 min, the $TrBF_4$ solution and the control reaction turn clear after 5 h. The resulting reaction mixture is centrifuged (9000 rpm, 4 min). The supernatant is discarded, and the pellet is redispersed in a small amount of DCM. The precipitation/dispersion cycle is repeated twice. The purified functionalized SiNCs are redispersed in $CDCl_3$ and analyzed with $^1$H-NMR spectroscopy.

**Polymerization of THF**

To 0.05 mmol of the respective trityl salt or 9 mg of freeze-dried SiNSs or SiNCs, 1 mL of dry THF is added and stirred. Successful polymerizations are indicated by an immediate color change of the polymerization mixture to brown and an increase in viscosity. Polymerizations that do not exhibit immediate initiation are stirred for 8 h at room temperature. To determine the conversion, $^1$H-NMR spectra of the crude solution in $CDCl_3$ are recorded.

**Variation of Silicon Nanomaterial**

4 mg of SiNC/$SiO_2$ (9 nm or 20 nm) composite is etched according to 6.1.1.2, redispersed in 1 mL dry dichloromethane and 2 eq. (0.05 mmol for 9 nm, 0.02 mmol for 20 nm) of $TrBF_4$ is added. The dispersion is treated for 15 min with ultrasonication. Afterward, 1 mL of dodecanethiol (4.2 mmol) or 0.3 mL of propylamine (3.7 mmol) is added. The suspension is degassed *via* three freeze-pump thaw cycles and stirred at 40 °C for 16 h. The resulting reaction mixture is centrifuged (9000 rpm, 4 min). The supernatant is discarded, and the residue is redispersed in fresh acetonitrile. The precipitation/dispersion cycle is repeated twice to yield purified functionalized SiNCs.

### 6.4.3. Mechanistic Insights and Fluorination

**Determination of Lewis Acidity with the Gutmann-Beckett method**

For preliminary tests, pure trityl salts and non-activated SiNCs are mixed in stoichiometric amounts with a 0.5 M $Et_3PO$ solution. For activated SiNSs, 3 eq. and in the case of activated SiNCs, 1 eq. of TrBCF is added, and the resulting mixture is stirred in 1.5 mL dry toluene overnight. The reaction mixture is then centrifuged (9000 rpm, 4 min). The supernatant is discarded, and the residue is redispersed in acetonitrile. The precipitation/dispersion cycle is repeated two additional times. Afterward, stoichiometric amounts of 0.5 M $Et_3PO$-solution are added. All samples are diluted in $C_6D_6$ and $^{31}$P-NMR spectra are recorded.

**NMR monitoring of fluorination during SiNC activation**

2 mg of freeze-dried SiNCs are mixed with 0.3 mmol of trityl salt in dry $CDCl_3$ precooled to -35°C, and the mixture is left at this temperature for 1 h. The solution is transferred from a glass vile to a screw cap NMR tube. $^1$H and $^{19}$F-NMR measurements are acquired immediately in the cooled state and one day later at room temperature.

**Sample preparation for solid-state-NMR**

90 mg of freeze-dried etched SiNSs obtained according to 6.1.2.3 are mixed with 660 mg of $TrBF_4$ pre-dissolved in 5 mL of dry MeCN and stirred for 1.5 h. The yellow solid with the dark liquid phase is washed with 3x5 mL of dry MeCN until the solvent is colorless. The solid is redispersed in 5 mL dry benzene, freeze-dried, and transferred to a PTFE rotor.

**Reactions with molecular model substrates**

For molecular test reactions, 0.6 mmol of $TMS_3SiH$ or TMDS (1 eq.) are added to solutions of 0.6 mmol $TrBF_4$ (1 eq.) in 0.5 mL $CDCl_3$ leading to an immediate decoloration of the reaction mixture. Subsequently, $^1$H, $^{19}$F, and $^{29}$Si-NMR are acquired in a screwcap NMR tube to investigate the formed species.

## 6.5. New Janus SiNC Synthesis with Organolithium Reagents

### 6.5.1. Initial Synthesis Approach

**DHC of SiNCs on SiNS**

The procedure to deposit SiNCs on SiNSs is adapted from a literature-known process.[48] 500 mg of SiNC/$SiO_2$ composite is etched as described in 6.1.2.3, the freshly etched SiNC-H is dispersed in 4 mL toluene, and the dispersion is degassed with argon for 20 min. 20 mg SiNSs are prepared according to 6.1.2.3 and added to the suspension with 1 mL toluene. The resulting reaction mixture is degassed *via* two freeze-pump-thaw cycles and stirred at 100 °C for around three days before it is cooled to room temperature.

**Functionalization of SiNC@SiNS *via* Hydrosilylation**

2 mmol of alkene and 7 mg 4-DDB are added to the reaction mixture of SiNC@SiNS, which is then degassed *via* two freeze-pump-thaw cycles and covered with aluminum foil to protect the SiNSs from decomposition by UV irradiation. After stirring at room temperature overnight, it is centrifuged (9000 rpm, 4 min) to remove uniformly functionalized SiNCs dispersed in the toluene supernatant.

**Liberation and Functionalization of the Janus SiNC**

The residue is redispersed in 4 mL of dry toluene, and the dispersion is degassed *via* two freeze-pump-thaw cycles. 0.5 mmol of organolithium reagent is added, and the reaction mixture is stirred at room temperature overnight. The resulting reaction mixture, which appears dark and clear, is then precipitated by slowly adding it dropwise to a solution of 12 mL of MeOH/EtOH (1:1) and 0.2 mL of HCl (37% aq.). This is followed by centrifugation at 9000 rpm for 4 min. 2 mL toluene or benzene is added to the residue leading to a colored solution of functionalized Janus SiNCs and a remaining precipitate (destructed SiNSs). The liquid is filtered using a syringe filter (0.45 µm) and reduced before it is precipitated by dropwise addition to 12 mL MeOH/EtOH (1:1). The precipitation/dispersion cycle is repeated two times. The product is finally dissolved in 1.5 mL benzene and freeze dried.

### 6.5.2. Capping with Ethynylaryls of 3 and 8 nm Janus SiNC

**Synthesis of 8 nm Janus SiNC**

The synthesis of 8 nm Janus SiNCs is performed similarly to the process described in 6.5.1. The SiNCs exhibit PL in the IR region, so reaction control of the bare eye under UV irradiation is impossible. Due to the lower solubility of the larger SiNCs, the solution is not filtered over a syringe filter but left for 10 min to settle the SiNSs residues. Afterward, purification *via* precipitation in MeOH/EtOH (1:1) is conducted analogously to 6.5.1.

**SiNSs Destruction Test with PhLi**

10 mg of freeze-dried SiNS-Dodec is obtained after etching and capping with dodecene according to 6.1.2.3, and the resulting functionalized SiNSs are dispersed in dry toluene. 0.3 mL of 2.3M PhLi solution is added dropwise while stirred at room temperature. The yellow solution turns colorless and opaque. The precipitate is drop-casted on carbon tape and characterized by SEM.

**Optimized Destruction of SiNSs**

4 mg of SiNS flakes are dispersed in 1.5 mL dry and degassed toluene and ultrasonicated for 3 h. Afterward, 1 mL of HexLi (2.6 M in hexane) is added and stirred overnight. The mixture is purified by precipitation in 12 mL MeOH/EtOH mixture (1:1) and 0.2 mL of HCl conc. The purification with alcohol is repeated twice.

For the etched SiNSs, 7.5 mg of flakes are dispersed in 1.5 mL dry and degassed toluene and ultrasonicated for 3 h, too. Afterward, the SiNSs are etched according to 6.1.2.3 and dispersed in toluene. 1 mL of HexLi (2.6 M in hexane) is added and stirred overnight. The mixture is purified by precipitation in 12 mL MeOH/EtOH mixture (1:1) and 0.2 mL of HCl conc.

**Functionalization of SiNCs with OLR**

300 mg of SiNC/$SiO_2$ composite is etched according to 6.1.1.2. and redispersed in 2 mL dry toluene, and degassed *via* three freeze-pump-thaw cycles. 0.2 mmol of organometallic reagent is added, and the dispersion is stirred at room temperature for 16 h. The resulting dark and clear reaction mixture is precipitated in a solution of 12 mL MeOH/EtOH 1:1 and 0.2 mL of HCl conc. Then the suspension is centrifuged (9000 rpm, 4 min) in ETFE tubes. The supernatant is discarded, and the pellet is re-dispersed. The precipitation/dispersion cycle is repeated two times without acid to yield purified functionalized SiNCs.

## 6.6. Silicon Nanosheet Motors

### 6.6.1. Reduction of Metal Salts with SiNS

**Synthesis of CuNP@SiNS with Different Anions**

6x10 mg of freeze-dried SiNS-H, obtained from etching according to 6.1.2.3, are put into a 1.5 mLglass vile each, and 1 mL of 80 mM copper salt solution in $H_2O$ ($CuNO_3$, $CuSO_4$, $Cu(CH_3COO)_2$, $CuCl_2$) or 1M HCl (CuO, CuCl) is added to achieve a SiH/Cu ratio of 4:1. The resulting suspension is ultrasonicated for 1 h, filtered, washed with 3 mL of dist. water and dried at 60 °C overnight.

**Synthesis of CuNP@SiNS with Different Silicon nanomaterials**

For the test reaction with SiNS flakes, 11 mg of dried material, obtained from exfoliation of commercial or self-made $CaSi_2$ according to 6.1.2.2, is added to 2 mL of 80 mM $CuCl_2$ solution

in 1 M HCl. After ultrasonication for 1 h, the suspension is filtered and washed with 3 mL of dist. water and dried at 60 °C overnight. The filtrates exhibit a dark color which indicates loss of CuNPs, which are not adsorbed to the flakes' surface.

15 mg of dodecene-capped SiNSs, obtained after HS with dodecene according to 6.1.2.4, are added to 1.5 mL of 80 mM $CuCl_2$ solution. After ultrasonication for 1 h, the suspension is filtered, washed with 3 mL of dist. water and dried at 60 °C overnight. The resulting material behaves highly hydrophobic.

**Stoichiometric Reduction of $CuCl_2$ to CuCl**

5 mg of SiNSs are mixed with 1 mL $CuCl_2$ (200 mM in dist. water) to reach a stoichiometric ratio of Cu and SiH. After ultrasonication for 1 h, the suspension is filtered, washed with 3 mL of dist. water and dried at 60 °C overnight.

**Analysis of Nanomotors' Movement**

A small amount of solid nanomaterial is dispersed in a glass cuvette (10 mm x 2 mm x 36 mm) containing 2% $H_2O_2$ solution and sealed with a PTFE cap. The cuvette is put horizontally underneath a light microscope and moving particles are searched.


Figure 61: Experimental setup for movement observation of nanomotors.

### 6.6.2. Synthesis of Anisotropic 2D Material

**Interphase Reaction**

For the anisotropic functionalization with dodecene, 2 mL of FC-72 and 5 mg of SiNS-H in 3 mL toluene are added to a Schlenk flask. 13 mg of 4-DDB is mixed with 0.5 mL of dodecene and added to the flask. The mixture is left at room temperature without stirring overnight. Afterward, 0.7 mL of $PdCl_2$ (8 mM in 1 M HCl) and three phases are obtained. The suspension is filtered and washed with dist. water.

To hydrophobize the glass for another experiment, two droplets of hexamethyldisilazane (HMDS) are added and the sealed flask is heated shortly under argon. Residing HMDS is removed *in vacuo*.

**Dropcast on Glass**

0.25 mL of a SiNS-H dispersion in toluene or pentane is dropped on standard and hydrophobic glass substrates and left for 30 min. Afterward, $PdCl_2$ solution (80 mM in $H_2O$) is dropped on the substrates. In all cases, the SiNSs detach from the glass surface.

For hydrophobizing the glass, two droplets of hexamethyldisilazane (HMDS) are added, and the sealed flask is heated shortly under argon. Residing HMDS is removed *in vacuo*.

**Fixation on Carbon tape**

For drop-casting on the carbon tape, 0.5 mg of freeze-dried SiNS-H are redispersed in 0.2 mL of toluene. 1-2 droplets of this suspension are put onto the carbon tape and dried in vacuo. In another experiment, a small amount (~0.2 mg) of SiNS-H is pressed onto carbon tape with a spatula. In both cases, 2 drops of 80 mM $PdCl_2$ solution are disposed on the loaded tape, left for 1 h at room temperature, and washed with dist. water and scratched off with a spatula to test the material for directed movement.

**Pickering Emulsion**

In a 50 mL PP falcon tube 3 mL dest. water, 0.25 mL brine, and 0.3 g of paraffine wax are added and heated to 70 °C in an oil bath. When the wax is melted, 3 mg of SiC nanoparticles and 1 mg of SiNS-H are added and treated with an ultrasonication horn for 30 s at 10% power. After the treatment, the tube is immediately stored in an ice bath to solidify the wax particles. Afterward, the wax particles are filtered, freeze-dried, and 0.5 mL of $PdCl_2$ solution (1 g/mL) is added and shaken gently for 2 h. The suspension is filtered again, freeze-dried, and washed with 8 mL pentane to liberate the hybrid material.

### 6.6.3. Addition of Metal Nanoparticles

**Synthesis of PdNP**

The PdNPs are synthesized according to a procedure described in the literature.[230] 275 mg of citric acid (1.3 mmol, 18 eq.) and 38.8 mg of PVP (0.35 mmol, 5 eq.) are dissolved in 7 mL of DI water stirred under reflux. 12.4 mg of $PdCl_2$ (0.07 mmol, 1 eq.) are dissolved in 3 mL of DI water and added quickly. The solution is stirred under reflux for 3 h. The resulting PdNPs are separated by ultracentrifugation (25000 rpm, 30 min) and washed twice with 1.5 mL of EtOH and redispersed in 3 mL

**Synthesis of PdNP+SiNS**

1 mL of the resulting suspension is mixed with 2 mg of freeze-dried SiNSs observed from etching according to 6.1.2.3, stirred for 2 h, filtered, and dried at 60 °C.

## 6.7. Application of SiNCs in Optoelectronic Devices

### 6.7.1. Si-LEDs with Varied Chain Lengths

**Functionalization of SiNCs with OLR of Different Chain Lengths**

OctLi and HexLi are prepared from the respective chloroalkane in the presence of 2 eq. of lithium in dry toluene.[231]

The preparation of SiNCs for Si-LEDs is upscaled to exclude performance variations caused by SiNC size distribution and degree of oxidation: 2.2 g of SiNC/$SiO_2$ composite is etched according to 6.1.1.2. and redispersed in 8 mL dry toluene and degassed *via* three freeze-pump-thaw cycles. 4 mmol of organometallic reagent is added, and the dispersion is stirred at room temperature for 16 h. The resulting dark and clear reaction mixture is precipitated in a solution of 60 mL MeOH/EtOH 1:1 and 1 mL of HCl conc. Then the suspension is centrifuged (9000 rpm, 4 min) in ETFE tubes. The supernatant is discarded, and the pellet is re-dispersed. The precipitation/dispersion cycle is repeated two times without acid to yield purified functionalized SiNCs.

**Fabrication of Si-LEDs**

For the fabrication of optoelectronic devices, glass substrates with pre-patterned ITO films (15 Ω/square, 120 nm) are cleaned by successive sonication for 15 min each in lab detergent, acetone, and isopropanol (HPLC grade), dried by a nitrogen gun and heated for 2 min at 140 °C on a hot plate. All layers are annealed at 140 C for 10 min after spin coating. The PEDOT:PSS solution in isopropanol (1:3) is spin-coated to a thickness of 20 nm and annealed at 140 °C for 10 min in ambient conditions. For further processing, all substrates are transferred into a nitrogen-filled glovebox. Afterward, poly-TPD (5 mg/mL in DCB) is spin coated and annealed at 140 °C for 10 min to a 10 nm-thick layer. The SiQDs are diluted in dry toluene (10 mg/mL for SiNC-Hex and SiNC-Oct and 20 mg/mL for SiNC-Dodec) and deposited with a thin film thickness of 35 nm. On top, a 25 nm-thick layer of ZnO nanoparticles (1:3 in dry isopropanol) is spin-coated. Before usage, the SiQD and ZnO solution is filtered by a 0.2 µm polytetrafluoroethylene (PTFE) filter, while the PEDOT:PSS solution is filtered over a 0.45 µm regenerated cellulose (RC) syringe filter. The Ag top electrode is thermally evaporated by a *Leybold Univex 350* PVD system (3 Å/s, $<10^{-5}$ mbar). The Ag and ITO cross-section defines the 3x3 mm device area. The devices are encapsulated with a thin microscope cover glass (18 mm x 18 mm x 0.1 mm) glued on top of the device by a two-component epoxy resin *Araldite 2011* and cured on the hot plate at 80 °C for 10 min.

**Characterization of Si-LEDs**

The SiQD LEDs are characterized by a *Thorlabs IS200-4* integrating sphere and a calibrated *AvaSpec-ULS2048 64TEC* spectrometer from *Avantes*. An EL spectrum is measured at every

measurement step. For the electrical characterization, a two-channel *Keithley 2602A* source measure unit and the software *Matlab* are used to control the voltage and measure the current at the same time.

### 6.7.2. Si-LEDs with Sulfide-SiNC

**Functionalization of SiNCs with Butyl Disulfide**

300 mg of SiNC/$SiO_2$ composite is etched according to 6.1.1.2. and redispersed in 2 mL dry DCB, and 0.3 mL of butyl disulfide is added. The dispersion is degassed *via* three freeze-pump-thaw cycles and stirred at 150 °C for 1 h. The resulting reaction mixture is concentrated *in vacuo* precipitated in 6 mL acetonitrile and centrifuged (9000 rpm, 4 min). The supernatant is discarded, and the pellet is re-dispersed. The precipitation/dispersion cycle is repeated two times and freeze-dried in benzene to yield purified functionalized SiNCs.

**Fabrication and Characterization of Si-LEDs**

Si-LEDs with sulfide-SiNCs are prepared from a 10 mg/mL solution in DCB and characterized analogous to the description in 6.7.1.

## 7. References


[1] R. Feynman, *Caltech Engineering and Science* **1960**, *23*, 22.
[2] C. Chen, *Introduction to scanning tunneling microscopy*, Oxford University Press, New York, **1993**.
[3] "Global Nanotechnology Market - Industry Trends and Forecast to 2029", can be found under https://www.databridgemarketresearch.com/reports/global-nanotechnology-market, **2022**.
[4] M. Faraday, *Phil. Trans. R. Soc.* **1857**, *147*, 145.
[5] R. D. Tweney, *Perspectives on Science* **2006**, *14*, 97.
[6] Z. Li, Y. Yi, X. Luo, N. Xiong, Y. Liu, S. Li, R. Sun, Y. Wang, B. Hu, W. Chen et al., *J Med Virol* **2020**, *92*, 1518.
[7] Z. I. Alferov, R. F. Kazarinov, 181737.
[8] H. Kroemer, *Proc. IEEE* **1963**, *51*, 1782.
[9] V. Wood, V. Bulović, *Nano Reviews* **2010**, *1*, 5202.
[10] H. Okamoto, Y. Sugiyama, H. Nakano, *Chemistry* **2011**, *17*, 9864.
[11] L. T. Canham, *Appl. Phys. Lett.* **1990**, *57*, 1046.
[12] A. A. Moosa, M. S. Abed, *Turk J Chem* **2021**, *45*, 493.
[13] A. S. Heintz, M. J. Fink, B. S. Mitchell, *Adv. Mater.* **2007**, *19*, 3984.
[14] L. Patrone, D. Nelson, V. I. Safarov, M. Sentis, W. Marine, S. Giorgio, *J. Appl. Phys.* **2000**, *87*, 3829.
[15] N. Mansour, A. Momeni, R. Karimzadeh, M. Amini, *Opt. Mater. Express* **2012**, *2*, 740.
[16] T. Shimizu-Iwayama, K. Fujita, S. Nakao, K. Saitoh, T. Fujita, N. Itoh, *J. Appl. Phys.* **1994**, *75*, 7779.
[17] N. Lalic, J. Linnros, *Journal of Luminescence* **1998**, *80*, 263.
[18] L. E. Brus, P. F. Szajowski, W. L. Wilson, T. D. Harris, S. Schuppler, P. H. Citrin, *J Am Chem Soc* **1995**, *117*, 2915.
[19] X. Li, Y. He, S. S. Talukdar, M. T. Swihart, *Langmuir* **2003**, *19*, 8490.
[20] U. Kortshagen, *J. Phys. D: Appl. Phys.* **2009**, *42*, 113001.
[21] L. Mangolini, E. Thimsen, U. Kortshagen, *Nano Lett* **2005**, *5*, 655.
[22] Z. Li, U. R. Kortshagen, *Chem. Mater.* **2019**, *31*, 8451.
[23] J. R. Heath, *Science* **1992**, *258*, 1131.
[24] X. Cheng, S. B. Lowe, P. J. Reece, J. J. Gooding, *Chem Soc Rev* **2014**, *43*, 2680.
[25] J. P. Wilcoxon, G. A. Samara, P. N. Provencio, *Phys. Rev. B* **1999**, *60*, 2704.
[26] R. K. Baldwin, K. A. Pettigrew, J. C. Garno, P. P. Power, G. Liu, S. M. Kauzlarich, *J Am Chem Soc* **2002**, *124*, 1150.

[27] S. Milliken, A. N. Thiessen, I. T. Cheong, K. M. O'Connor, Z. Li, R. W. Hooper, C. J. T. Robidillo, J. G. C. Veinot, *Nanoscale* **2021**, *13*, 16379.
[28] R. A. Bley, S. M. Kauzlarich, *J Am Chem Soc* **1996**, *118*, 12461.
[29] D. Mayeri, B. L. Phillips, M. P. Augustine, S. M. Kauzlarich, *Chem. Mater.* **2001**, *13*, 765.
[30] K. A. Pettigrew, Q. Liu, P. P. Power, S. M. Kauzlarich, *Chem. Mater.* **2003**, *15*, 4005.
[31] S. Hayashi, T. Nagareda, Y. K. Yoshihiko Kanzawa, K. Y. Keiichi Yamamoto, *Jpn. J. Appl. Phys.* **1993**, *32*, 3840.
[32] H. Sugimoto, T. Okazaki, M. Fujii, *Adv. Optical Mater.* **2020**, *8*, 2000033.
[33] C. M. Hessel, E. J. Henderson, J. G. C. Veinot, *Chem. Mater.* **2006**, *18*, 6139.
[34] C.-C. Yang, W.-C. Chen, *J. Mater. Chem.* **2002**, *12*, 1138.
[35] M. L. Mastronardi, F. Maier-Flaig, D. Faulkner, E. J. Henderson, C. Kübel, U. Lemmer, G. A. Ozin, *Nano Lett* **2012**, *12*, 337.
[36] C. M. Hessel, D. Reid, M. G. Panthani, M. R. Rasch, B. W. Goodfellow, J. Wei, H. Fujii, V. Akhavan, B. A. Korgel, *Chem. Mater.* **2012**, *24*, 393.
[37] S. Terada, Y. Xin, K. Saitow, *Chem. Mater.* **2020**, *32*, 8382.
[38] R. J. Clark, M. Aghajamali, C. M. Gonzalez, L. Hadidi, M. A. Islam, M. Javadi, M. H. Mobarok, T. K. Purkait, C. J. T. Robidillo, R. Sinelnikov et al., *Chem. Mater.* **2017**, *29*, 80.
[39] G. W. Trucks, K. Raghavachari, G. S. Higashi, Y. J. Chabal, *Phys. Rev. Lett.* **1990**, *65*, 504.
[40] M. Steinert, J. Acker, S. Oswald, K. Wetzig, *J. Phys. Chem. C* **2007**, *111*, 2133.
[41] J. K. Kang, C. B. Musgrave, *J. Chem. Phys.* **2002**, *116*, 275.
[42] Y.-R. Luo, *Comprehensive Handbook of Chemical Bond Energies*, CRC Press, **2007**.
[43] J. M. Buriak, *Chem Rev* **2002**, *102*, 1271.
[44] J. Holm, J. T. Roberts, *Langmuir* **2009**, *25*, 7050.
[45] Z. Yang, M. Iqbal, A. R. Dobbie, J. G. C. Veinot, *J Am Chem Soc* **2013**, *135*, 17595.
[46] A. Fermi, M. Locritani, G. Di Carlo, M. Pizzotti, S. Caramori, Y. Yu, B. A. Korgel, G. Bergamini, P. Ceroni, *Faraday Discuss* **2015**, *185*, 481.
[47] J. A. Kelly, J. G. C. Veinot, *ACS Nano* **2010**, *4*, 4645.
[48] M. J. Kloberg, H. Yu, E. Groß, F. Eckmann, T. M. F. Restle, T. F. Fässler, J. G. C. Veinot, B. Rieger, *Adv. Mater.* **2021**, *33*, e2100288.

[49] T. Helbich, M. J. Kloberg, R. Sinelnikov, A. Lyuleeva, J. G. C. Veinot, B. Rieger, *Nanoscale* **2017**, *9*, 7739.
[50] I. M. D. Höhlein, J. Kehrle, T. Helbich, Z. Yang, J. G. C. Veinot, B. Rieger, *Chemistry* **2014**, *20*, 4212.
[51] Z. Yang, C. M. Gonzalez, T. K. Purkait, M. Iqbal, A. Meldrum, J. G. C. Veinot, *Langmuir* **2015**, *31*, 10540.
[52] J. Nelles, D. Sendor, A. Ebbers, F. M. Petrat, H. Wiggers, C. Schulz, U. Simon, *Colloid Polym Sci* **2007**, *285*, 729.
[53] M. H. Mobarok, T. K. Purkait, M. A. Islam, M. Miskolzie, J. G. C. Veinot, *Angew. Chem.* **2017**, *129*, 6169.
[54] M. A. Islam, M. H. Mobarok, R. Sinelnikov, T. K. Purkait, J. G. C. Veinot, *Langmuir* **2017**, *33*, 8766.
[55] X. D. Pi, R. W. Liptak, J. Deneen Nowak, N. P. Wells, C. B. Carter, S. A. Campbell, U. Kortshagen, *Nanotechnology* **2008**, *19*, 245603.
[56] Y.-C. Liao, J. T. Roberts, *J Am Chem Soc* **2006**, *128*, 9061.
[57] B. N. Jariwala, O. S. Dewey, P. Stradins, C. V. Ciobanu, S. Agarwal, *ACS Appl Mater Interfaces* **2011**, *3*, 3033.
[58] R. D. Tilley, J. H. Warner, K. Yamamoto, I. Matsui, H. Fujimori, *Chem Commun (Camb)* **2005**, 1833.
[59] J. M. Buriak, M. P. Stewart, T. W. Geders, M. J. Allen, H. C. Choi, J. Smith, D. Raftery, L. T. Canham, *J Am Chem Soc* **1999**, *121*, 11491.
[60] T. K. Purkait, M. Iqbal, M. H. Wahl, K. Gottschling, C. M. Gonzalez, M. A. Islam, J. G. C. Veinot, *J Am Chem Soc* **2014**, *136*, 17914.
[61] J. H. Song, M. J. Sailor, *J Am Chem Soc* **1998**, *120*, 2376.
[62] N. Y. Kim, P. E. Laibinis, *J Am Chem Soc* **1998**, *120*, 4516.
[63] I. M. D. Höhlein, A. Angı, R. Sinelnikov, J. G. C. Veinot, B. Rieger, *Chemistry* **2015**, *21*, 2755.
[64] A. Angı, M. Loch, R. Sinelnikov, J. G. C. Veinot, M. Becherer, P. Lugli, B. Rieger, *Nanoscale* **2018**, *10*, 10337.
[65] A. Angı, *Surface Chemistry of Silicon Nanocrystals: Influence on Properties and Applications*, Technische Universität München, **2018**.
[66] Y. Yu, C. E. Rowland, R. D. Schaller, B. A. Korgel, *Langmuir* **2015**, *31*, 6886.
[67] M. Dasog, J. R. Thompson, N. S. Lewis, *Chem. Mater.* **2017**, *29*, 7002.
[68] M. Dasog, G. B. de los Reyes, L. V. Titova, F. A. Hegmann, J. G. C. Veinot, *ACS Nano* **2014**, *8*, 9636.
[69] L. Ruizendaal, S. P. Pujari, V. Gevaerts, J. M. J. Paulusse, H. Zuilhof, *Chem Asian J* **2011**, *6*, 2776.

[70] G. Morselli, F. Romano, P. Ceroni, *Faraday Discuss* **2020**, *222*, 108.
[71] F. Romano, S. Angeloni, G. Morselli, R. Mazzaro, V. Morandi, J. R. Shell, X. Cao, B. W. Pogue, P. Ceroni, *Nanoscale* **2020**, *12*, 7921.
[72] J. Kehrle, I. M. D. Höhlein, Z. Yang, A.-R. Jochem, T. Helbich, T. Kraus, J. G. C. Veinot, B. Rieger, *Angew Chem Int Ed Engl* **2014**, *53*, 12494.
[73] J. R. Chelikowsky, M. L. Cohen, *Phys. Rev. B* **1974**, *10*, 5095.
[74] B. Monserrat, R. J. Needs, *Phys. Rev. B* **2014**, *89*, 214304.
[75] R. Sinelnikov, M. Dasog, J. Beamish, A. Meldrum, J. G. C. Veinot, *ACS Photonics* **2017**, *4*, 1920.
[76] M. V. Wolkin, J. Jorne, P. M. Fauchet, G. Allan, C. Delerue, *Phys. Rev. Lett.* **1999**, *82*, 197.
[77] R. Mazzaro, F. Romano, P. Ceroni, *Phys Chem Chem Phys* **2017**, *19*, 26507.
[78] G. W. Bryant, *Phys Rev B Condens Matter* **1988**, *37*, 8763.
[79] Al.L. Efros, Al. L. Efros, *Soviet physics. Semiconductors* **1982**, *16*, 772.
[80] J. P. Proot, C. Delerue, G. Allan, *Appl. Phys. Lett.* **1992**, *61*, 1948.
[81] L. Pavesi, D. J. Lockwood (Eds.) *Topics in Applied Physics*, *Vol. 94*, Springer-Verlag, Berlin, **2004**.
[82] W. J. I. DeBenedetti, Y. J. Chabal, *Journal of Vacuum Science & Technology A: Vacuum, Surfaces, and Films* **2013**, *31*, 50826.
[83] B. Dierre, R.-J. Xie, N. Hirosaki, T. Sekiguchi, *J. Mater. Res.* **2007**, *22*, 1933.
[84] A. Angı, R. Sinelnikov, A. Meldrum, J. G. C. Veinot, I. Balberg, D. Azulay, O. Millo, B. Rieger, *Nanoscale* **2016**, *8*, 7849.
[85] A. N. Thiessen, M. Ha, R. W. Hooper, H. Yu, A. O. Oliynyk, J. G. C. Veinot, V. K. Michaelis, *Chem. Mater.* **2019**, *31*, 678.
[86] A. N. Thiessen, L. Zhang, A. O. Oliynyk, H. Yu, K. M. O'Connor, A. Meldrum, J. G. C. Veinot, *Chem. Mater.* **2020**, *32*, 6838.
[87] D. Balzar, N. Audebrand, M. R. Daymond, A. Fitch, A. Hewat, J. I. Langford, A. Le Bail, D. Louër, O. Masson, C. N. McCowan et al., *J Appl Crystallogr* **2004**, *37*, 911.
[88] S. Bhattacharjee, I. M. C. M. Rietjens, M. P. Singh, T. M. Atkins, T. K. Purkait, Z. Xu, S. Regli, A. Shukaliak, R. J. Clark, B. S. Mitchell et al., *Nanoscale* **2013**, *5*, 4870.
[89] A. Shiohara, S. Hanada, S. Prabakar, K. Fujioka, T. H. Lim, K. Yamamoto, P. T. Northcote, R. D. Tilley, *J Am Chem Soc* **2010**, *132*, 248.

[90] J. Liu, F. Erogbogbo, K.-T. Yong, L. Ye, J. Liu, R. Hu, H. Chen, Y. Hu, Y. Yang, J. Yang et al., *ACS Nano* **2013**, *7*, 7303.
[91] A. M. Derfus, W. C. W. Chan, S. N. Bhatia, *Nano Lett.* **2004**, *4*, 11.
[92] C. H. Nguyen, C. Zeng, S. Boitano, J. A. Field, R. Sierra-Alvarez, *Int J Toxicol* **2020**, *39*, 218.
[93] Z. F. Li, E. Ruckenstein, *Nano Lett.* **2004**, *4*, 1463.
[94] N. H. Alsharif, C. E. M. Berger, S. S. Varanasi, Y. Chao, B. R. Horrocks, H. K. Datta, *Small* **2009**, *5*, 221.
[95] F. Erogbogbo, K.-T. Yong, I. Roy, G. Xu, P. N. Prasad, M. T. Swihart, *ACS Nano* **2008**, *2*, 873.
[96] C. Tu, X. Ma, P. Pantazis, S. M. Kauzlarich, A. Y. Louie, *J Am Chem Soc* **2010**, *132*, 2016.
[97] F. Erogbogbo, C.-W. Chang, J. L. May, L. Liu, R. Kumar, W.-C. Law, H. Ding, K. T. Yong, I. Roy, M. Sheshadri et al., *Nanoscale* **2012**, *4*, 5483.
[98] A. Jane, R. Dronov, A. Hodges, N. H. Voelcker, *Trends in Biotechnology* **2009**, *27*, 230.
[99] F. A. Harraz, *Sensors and Actuators B: Chemical* **2014**, *202*, 897.
[100] M. J. Sailor, E. C. Wu, *Adv. Funct. Mater.* **2009**, *19*, 3195.
[101] R. Freeman, J. Girsh, I. Willner, *ACS Appl Mater Interfaces* **2013**, *5*, 2815.
[102] C. M. Gonzalez, M. Iqbal, M. Dasog, D. G. Piercey, R. Lockwood, T. M. Klapötke, J. G. C. Veinot, *Nanoscale* **2014**, *6*, 2608.
[103] J. Zhang, S.-H. Yu, *Nanoscale* **2014**, *6*, 4096.
[104] J. Zhao, J. Deng, Y. Yi, H. Li, Y. Zhang, S. Yao, *Talanta* **2014**, *125*, 372.
[105] J. Lin, Q. Wang, *RSC Adv* **2015**, *5*, 27458.
[106] Y. Yi, G. Zhu, C. Liu, Y. Huang, Y. Zhang, H. Li, J. Zhao, S. Yao, *Anal Chem* **2013**, *85*, 11464.
[107] Y. Feng, Y. Liu, C. Su, X. Ji, Z. He, *Sensors and Actuators B: Chemical* **2014**, *203*, 795.
[108] C. M. Gonzalez, J. G. C. Veinot, *J. Mater. Chem. C* **2016**, *4*, 4836.
[109] F. Priolo, T. Gregorkiewicz, M. Galli, T. F. Krauss, *Nature Nanotech* **2014**, *9*, 19.
[110] W. Shockley, H. J. Queisser, *J. Appl. Phys.* **1961**, *32*, 510.
[111] A. R. Zanatta, *Results in Optics* **2022**, *9*, 100320.
[112] X. Pi, Q. Li, D. Li, D. Yang, *Sol. Energy Mater. Sol. Cells* **2011**, *95*, 2941.
[113] R. Mazzaro, A. Gradone, S. Angeloni, G. Morselli, P. G. Cozzi, F. Romano, A. Vomiero, P. Ceroni, *ACS Photonics* **2019**, *6*, 2303.

[114] S. Saeed, E. M. L. D. de Jong, K. Dohnalova, T. Gregorkiewicz, *Nat Commun* **2014**, *5*, 4665.
[115] S. K. Shrestha, P. Aliberti, G. J. Conibeer, *Sol. Energy Mater. Sol. Cells* **2010**, *94*, 1546.
[116] M. C. Beard, K. P. Knutsen, P. Yu, J. M. Luther, Q. Song, W. K. Metzger, R. J. Ellingson, A. J. Nozik, *Nano Lett.* **2007**, *7*, 2506.
[117] Z. Sun, X. Chen, Y. He, J. Li, J. Wang, H. Yan, Y. Zhang, *Advanced Energy Materials* **2022**, *12*, 2200015.
[118] S. Guha, J. Yang, B. Yan, *Sol. Energy Mater. Sol. Cells* **2013**, *119*, 1.
[119] S.-K. Kim, C.-H. Cho, B.-H. Kim, S.-J. Park, J. Won Lee, *Appl. Phys. Lett.* **2009**, *95*, 143120.
[120] C.-W. Jiang, M. A. Green, *J. Appl. Phys.* **2006**, *99*, 114902.
[121] E.-C. Cho, S. Park, X. Hao, D. Song, G. Conibeer, S.-C. Park, M. A. Green, *Nanotechnology* **2008**, *19*, 245201.
[122] C.-Y. Liu, Z. C. Holman, U. R. Kortshagen, *Adv. Funct. Mater.* **2010**, *20*, 2157.
[123] Z. Ni, S. Zhou, S. Zhao, W. Peng, D. Yang, X. Pi, *Materials Science and Engineering: R: Reports* **2019**, *138*, 85.
[124] F. Wöhler, *Ann. Chem. Pharm.* **1863**, *127*, 257.
[125] A. Weiss, G. Beil, H. Meyer, *Zeitschrift für Naturforschung B* **1980**, *35*, 25.
[126] Dahn, JR, B. M. Way, E. Fuller, J. S. Tse, *Phys Rev B Condens Matter* **1993**, *48*, 17872.
[127] S. Yamanaka, H. Matsu-ura, M. Ishikawa, *Materials Research Bulletin* **1996**, *31*, 307.
[128] K. Nishimura, Y. Nagao, S. Yamanaka, H. Matsu-ura, *Jpn. J. Appl. Phys.* **1996**, *35*, L293.
[129] W. L. B. Huey, J. E. Goldberger, *Chem. Soc. Rev.* **2018**, *47*, 6201.
[130] G. Schott, D. Naumann, *Z. Anorg. Allg. Chem.* **1957**, *291*, 103.
[131] E. Hengge, G. Scheffler, *Monatsh. Chem.* **1964**, *95*, 1450.
[132] H. Nakano, T. Mitsuoka, M. Harada, K. Horibuchi, H. Nozaki, N. Takahashi, T. Nonaka, Y. Seno, H. Nakamura, *Angew. Chem.* **2006**, *118*, 6451.
[133] S. W. Kim, J. Lee, J. H. Sung, D. Seo, I. Kim, M.-H. Jo, B. W. Kwon, W. K. Choi, H.-J. Choi, *ACS Nano* **2014**, *8*, 6556.
[134] H. Okamoto, Y. Sugiyama, K. Nakanishi, T. Ohta, T. Mitsuoka, H. Nakano, *Chem. Mater.* **2015**, *27*, 1292.
[135] Y. Sugiyama, H. Okamoto, T. Mitsuoka, T. Morikawa, K. Nakanishi, T. Ohta, H. Nakano, *J Am Chem Soc* **2010**, *132*, 5946.

[136] T. Helbich, A. Lyuleeva, P. Marx, L. M. Scherf, T. K. Purkait, T. F. Fässler, P. Lugli, J. G. C. Veinot, B. Rieger, *Adv. Funct. Mater.* **2017**, *27*, 1606764.
[137] T. Helbich, A. Lyuleeva, T. Ludwig, L. M. Scherf, T. F. Fässler, P. Lugli, B. Rieger, *Adv. Funct. Mater.* **2016**, *26*, 6711.
[138] T. Helbich, A. Lyuleeva, I. M. D. Höhlein, P. Marx, L. M. Scherf, J. Kehrle, T. F. Fässler, P. Lugli, B. Rieger, *Chemistry* **2016**, *22*, 6194.
[139] H. Nakano, M. Nakano, K. Nakanishi, D. Tanaka, Y. Sugiyama, T. Ikuno, H. Okamoto, T. Ohta, *J Am Chem Soc* **2012**, *134*, 5452.
[140] A. Lyuleeva, T. Helbich, B. Rieger, P. Lugli, *J. Phys. D: Appl. Phys.* **2017**, *50*, 135106.
[141] M. J. Kloberg, T. Helbich, B. Rieger, *Nanotechnology* **2019**, *30*, 75602.
[142] C. Zhang, A. de Sarkar, R.-Q. Zhang, *J. Phys. Chem. C* **2011**, *115*, 23682.
[143] O. D. Restrepo, R. Mishra, J. E. Goldberger, W. Windl, *J. Appl. Phys.* **2014**, *115*, 33711.
[144] F. Li, R. Lu, Q. Yao, E. Kan, Y. Liu, H. Wu, Y. Yuan, C. Xiao, K. Deng, *J. Phys. Chem. C* **2013**, *117*, 13283.
[145] D. Q. Fang, Y. Zhang, S. L. Zhang, *New J. Phys.* **2014**, *16*, 115006.
[146] B. J. Ryan, M. P. Hanrahan, Y. Wang, U. Ramesh, C. K. A. Nyamekye, R. D. Nelson, Z. Liu, C. Huang, B. Whitehead, J. Wang et al., *Chem. Mater.* **2020**, *32*, 795.
[147] I. Kuritka, F. Schauer, P. Saha, J. Zemek, P. Jiricek, S. Nespurek, *Czech J Phys* **2006**, *56*, 41.
[148] D. L. Staebler, C. R. Wronski, *Appl. Phys. Lett.* **1977**, *31*, 292.
[149] E. Hengge in *Topics in Current Chemistry Fortschritte der Chemischen Forschung* (Ed.: A. Horn), Springer Berlin Heidelberg, Berlin, Heidelberg, **1974**, pp. 1–127.
[150] A. Stathis, M. Stavrou, I. Papadakis, J. Mock, M. J. Kloberg, M. Becherer, A. Lyuleeva-Husemann, S. Couris, *J. Phys. Chem. C* **2021**, *125*, 18510.
[151] P. Bøggild, D. M. A. Mackenzie, P. R. Whelan, D. H. Petersen, J. D. Buron, A. Zurutuza, J. Gallop, L. Hao, P. U. Jepsen, *2D Mater.* **2017**, *4*, 42003.
[152] C. Qian, W. Sun, D. L. H. Hung, C. Qiu, M. Makaremi, S. G. Hari Kumar, L. Wan, M. Ghoussoub, T. E. Wood, M. Xia et al., *Nat Catal* **2019**, *2*, 46.
[153] M. Ohashi, R. Yaokawa, Y. Takatani, H. Nakano, *ChemNanoMat* **2017**, *3*, 534.

[154] Y. Kumai, S. Shirai, E. Sudo, J. Seki, H. Okamoto, Y. Sugiyama, H. Nakano, *Journal of Power Sources* **2011**, *196*, 1503.
[155] A. Lyuleeva, P. Holzmüller, T. Helbich, M. Stutzmann, M. S. Brandt, M. Becherer, P. Lugli, B. Rieger, *J. Mater. Chem. C* **2018**, *6*, 7343.
[156] M. N. Obrovac, L. Christensen, *Electrochem. Solid-State Lett.* **2004**, *7*, A93.
[157] C. W. Tang, S. A. VanSlyke, *Appl. Phys. Lett.* **1987**, *51*, 913.
[158] E. Bellmann, S. E. Shaheen, S. Thayumanavan, S. Barlow, R. H. Grubbs, S. R. Marder, B. Kippelen, N. Peyghambarian, *Chem. Mater.* **1998**, *10*, 1668.
[159] V. L. Colvin, M. C. Schlamp, A. P. Alivisatos, *Nature* **1994**, *370*, 354.
[160] H. J. Jang, J. Y. Lee, J. Kwak, D. Lee, J.-H. Park, B. Lee, Y. Y. Noh, *J. Inf. Disp.* **2019**, *20*, 1.
[161] *Restriction of the use of certain hazardous substances in electrical and electronic equipment*, **2017**.
[162] K.-Y. Cheng, R. Anthony, U. R. Kortshagen, R. J. Holmes, *Nano Lett* **2010**, *10*, 1154.
[163] K.-Y. Cheng, R. Anthony, U. R. Kortshagen, R. J. Holmes, *Nano Lett* **2011**, *11*, 1952.
[164] Schubert E. F., *Light Emitting Diodes Cambridge University*, **2006**.
[165] L. Yao, T. Yu, L. Ba, H. Meng, X. Fang, Y. Wang, L. Li, X. Rong, S. Wang, X. Wang et al., *J. Mater. Chem. C* **2016**, *4*, 673.
[166] B. Ghosh, H. Yamada, S. Chinnathambi, İ. N. G. Özbilgin, N. Shirahata, *J Phys Chem Lett* **2018**, *9*, 5400.
[167] F. Maier-Flaig, J. Rinck, M. Stephan, T. Bocksrocker, M. Bruns, C. Kübel, A. K. Powell, G. A. Ozin, U. Lemmer, *Nano Lett* **2013**, *13*, 475.
[168] X. Liu, S. Zhao, W. Gu, Y. Zhang, X. Qiao, Z. Ni, X. Pi, D. Yang, *ACS Appl Mater Interfaces* **2018**, *10*, 5959.
[169] Y. Xu, S. Terada, Y. Xin, H. Ueda, K. Saitow, *ACS Appl. Nano Mater.* **2022**, *5*, 7787.
[170] M. Loch, *Nanomaterials for hybrid organic-inorganic optoelectronic devices processed from solution*, Technische Universität München, **2018**.
[171] Z. Yang, M. H. Wahl, J. G. Veinot, *Can. J. Chem.* **2014**, *92*, 951.
[172] D. Kim, J. Joo, Y. Pan, A. Boarino, Y. W. Jun, K. H. Ahn, B. Arkles, M. J. Sailor, *Angew. Chem.* **2016**, *128*, 6533.
[173] H. Yu, A. N. Thiessen, M. A. Hossain, M. J. Kloberg, B. Rieger, J. G. C. Veinot, *Chem. Mater.* **2020**, *32*, 4536.
[174] M. Oestreich, J. Hermeke, J. Mohr, *Chem Soc Rev* **2015**, *44*, 2202.

[175] M. C. Lipke, A. L. Liberman-Martin, T. D. Tilley, *Angew Chem Int Ed Engl* **2017**, *56*, 2260.
[176] *Handbook of Chemistry and Physics, ed*, **1999**.
[177] J. He, J. S. Tse, D. D. Klug, K. F. Preston, *J. Mater. Chem.* **1998**, *8*, 705.
[178] J. Da Carlos Araujo Silva, M. Birot, J.-P. Pillot, M. Pétraud, *Journal of Organometallic Chemistry* **2002**, *646*, 179.
[179] A. G. Sturm, T. Santowski, T. Felder, K. M. Lewis, M. C. Holthausen, N. Auner, *Organometallics* **2022**, *41*, 1960.
[180] F. Koch, V. Petrova-Koch, T. Muschik, *Journal of Luminescence* **1993**, *57*, 271.
[181] M. Dasog, J. G. C. Veinot, *Phys. Status Solidi A* **2012**, *209*, 1844.
[182] P. D. Bartlett, F. E. Condon, A. Schneider, *J Am Chem Soc* **1944**, *66*, 1531.
[183] M. Dasog, K. Bader, J. G. C. Veinot, *Chem. Mater.* **2015**, *27*, 1153.
[184] E. Rogozhina, G. Belomoin, A. Smith, L. Abuhassan, N. Barry, O. Akcakir, P. V. Braun, M. H. Nayfeh, *Appl. Phys. Lett.* **2001**, *78*, 3711.
[185] I. M. D. Höhlein, J. Kehrle, T. K. Purkait, J. G. C. Veinot, B. Rieger, *Nanoscale* **2015**, *7*, 914.
[186] M. Dasog, J. R. Thompson, N. S. Lewis, *Chem. Mater.* **2017**, *29*, 7002.
[187] A. Angı, R. Sinelnikov, H. H. Heenen, A. Meldrum, J. G. C. Veinot, C. Scheurer, K. Reuter, O. Ashkenazy, D. Azulay, I. Balberg et al., *Nanotechnology* **2018**, *29*, 355705.
[188] M. Dasog, Z. Yang, S. Regli, T. M. Atkins, A. Faramus, M. P. Singh, E. Muthuswamy, S. M. Kauzlarich, R. D. Tilley, J. G. C. Veinot, *ACS Nano* **2013**, *7*, 2676.
[189] N. Shirahata, S. Furumi, Y. Sakka, *Journal of Crystal Growth* **2009**, *311*, 634.
[190] D. M. VonNiederhausern, G. M. Wilson, N. F. Giles, *J. Chem. Eng. Data* **2006**, *51*, 1982.
[191] S. S. Nekrashevich, V. A. Gritsenko, *J. Appl. Phys.* **2011**, *110*, 114103.
[192] V. Y. Lee, *Russ. Chem. Rev.* **2019**, *88*, 351.
[193] M. A. Beckett, G. C. Strickland, J. R. Holland, K. Sukumar Varma, *Polymer* **1996**, *37*, 4629.
[194] U. Mayer, V. Gutmann, W. Gerger, *Monatsh. Chem.* **1975**, *106*, 1235.
[195] S. Li, Y. Yuan, Y. Yang, C. Li, M. T. McMahon, M. Liu, S. Chen, X. Zhou, *J Mater Chem B* **2018**, *6*, 4293.
[196] Y. Ma, X. Pi, D. Yang, *J. Phys. Chem. C* **2012**, *116*, 5401.

[197] J. E. Santana, F. de Santiago, Á. Miranda, L. A. Pérez, F. Salazar, A. Trejo, M. Cruz-Irisson, *Mater. Adv.* **2021**, *2*, 1072.
[198] J. Lv, Q. Zhang, X. Zhong, S. Luo, *J Am Chem Soc* **2015**, *137*, 15576.
[199] S. Enthaler, *Angew. Chem.* **2014**, *126*, 2754.
[200] B. Greydanus, D. K. Schwartz, J. W. Medlin, *ACS Appl Mater Interfaces* **2020**, *12*, 2338.
[201] A. H. Gröschel, A. Walther, T. I. Löbling, F. H. Schacher, H. Schmalz, A. H. E. Müller, *Nature* **2013**, *503*, 247.
[202] E. Poggi, J.-F. Gohy, *Colloid Polym Sci* **2017**, *295*, 2083.
[203] M. J. Kloberg, *Two Sides of the Same Silicon Particle*, Technische Universität München, **2021**.
[204] Y. Cahyono, F. Darul Muttaqin, U. Maslakah, Darminto, *IOP Conf. Ser.: Mater. Sci. Eng.* **2017**, *196*, 12038.
[205] L. E. Marbella, J. E. Millstone, *Chem. Mater.* **2015**, *27*, 2721.
[206] J. Gibbs, Y. Zhao, *Front. Mater. Sci.* **2011**, *5*, 25.
[207] W. F. Paxton, K. C. Kistler, C. C. Olmeda, A. Sen, S. K. St Angelo, Y. Cao, T. E. Mallouk, P. E. Lammert, V. H. Crespi, *J Am Chem Soc* **2004**, *126*, 13424.
[208] S. Fournier-Bidoz, A. C. Arsenault, I. Manners, G. A. Ozin, *Chem Commun (Camb)* **2005**, *0*, 441.
[209] W. Gao, S. Sattayasamitsathit, J. Wang, *Chem Rec* **2012**, *12*, 224.
[210] G. A. Ozin, I. Manners, S. Fournier-Bidoz, A. Arsenault, *Adv. Mater.* **2005**, *17*, 3011.
[211] S. Shim, *Chem Rev* **2022**, *122*, 6986.
[212] M. Kuron, P. Kreissl, C. Holm, *Acc Chem Res* **2018**, *51*, 2998.
[213] M. Amouzadeh Tabrizi, M. Shamsipur, *RSC Adv* **2015**, *5*, 51508.
[214] X. Ma, K. Hahn, S. Sanchez, *J Am Chem Soc* **2015**, *137*, 4976.
[215] D. Kagan, R. Laocharoensuk, M. Zimmerman, C. Clawson, S. Balasubramanian, D. Kang, D. Bishop, S. Sattayasamitsathit, L. Zhang, J. Wang, *Small* **2010**, *6*, 2741.
[216] Z. Wu, Y. Wu, W. He, X. Lin, J. Sun, Q. He, *Angew Chem Int Ed Engl* **2013**, *52*, 7000.
[217] C. Ni, M. Chevalier, J. G. C. Veinot, *Nanoscale Adv.* **2022**, *5*, 228.
[218] Y. Li, E. Boone, M. A. El-Sayed, *Langmuir* **2002**, *18*, 4921.
[219] Y. Niu, L. K. Yeung, R. M. Crooks, *J Am Chem Soc* **2001**, *123*, 6840.
[220] T. J. Held, F. L. Dryer, *Int. J. Chem. Kinet.* **1998**, *30*, 805.
[221] H. Okamoto, Y. Kumai, Y. Sugiyama, T. Mitsuoka, K. Nakanishi, T. Ohta, H. Nozaki, S. Yamaguchi, S. Shirai, H. Nakano, *J Am Chem Soc* **2010**, *132*, 2710.

[222] M. Hiller, K. Köhler, *Chemie Ingenieur Technik* **2022**, *94*, 1720.
[223] F. Liang, K. Shen, X. Qu, C. Zhang, Q. Wang, J. Li, J. Liu, Z. Yang, *Angew. Chem.* **2011**, *123*, 2427.
[224] M. A. Creighton, Y. Ohata, J. Miyawaki, A. Bose, R. H. Hurt, *Langmuir* **2014**, *30*, 3687.
[225] T. Zhou, B. Wang, B. Dong, C. Y. Li, *Macromolecules* **2012**, *45*, 8780.
[226] D. Gonzalez Ortiz, C. Pochat-Bohatier, J. Cambedouzou, M. Bechelany, P. Miele, *Engineering* **2020**, *6*, 468.
[227] M. Tang, X. Wang, F. Wu, Y. Liu, S. Zhang, X. Pang, X. Li, H. Qiu, *Carbon* **2014**, *71*, 238.
[228] S. Nagarajan, D. Abessolo Ondo, S. Gassara, M. Bechelany, S. Balme, P. Miele, N. Kalkura, C. Pochat-Bohatier, *Langmuir* **2018**, *34*, 1542.
[229] S. Jiang, M. J. Schultz, Q. Chen, J. S. Moore, S. Granick, *Langmuir* **2008**, *24*, 10073.
[230] K. Leopold, M. Maier, M. Schuster, *Sci Total Environ* **2008**, *394*, 177.
[231] E. Groß, *Functionalized Silicon Nanocrystals as Luminescent Layer of Light Emitting Diodes*, Technische Universität München, **2019**.
[232] J. Mock, E. Groß, M. J. Kloberg, B. Rieger, M. Becherer, *Adv Photo Res* **2021**, *2*, 2100083.
[233] I. T. Cheong, J. Mock, M. Kallergi, E. Groß, A. Meldrum, B. Rieger, M. Becherer, J. G. C. Veinot, *Adv. Optical Mater.* **2023**, *11*, 2201834.
[234] J. Mock, M. Kallergi, E. Groß, M. Golibrzuch, B. Rieger, M. Becherer, *IEEE Photonics J.* **2022**, *14*, 1.
[235] A. Köhler, H. Bässler, *Electronic processes in organic semiconductors*. *An introduction*, Wiley, Weinheim, **2015**.
[236] M. Nagai, *J. Electrochem. Soc.* **2007**, *154*, J387.
[237] X. Liu, Y. Zhang, T. Yu, X. Qiao, R. Gresback, X. Pi, D. Yang, *Part. Part. Syst. Charact.* **2016**, *33*, 44.
[238] S. Pfaehler, A. Angı, D. Chryssikos, A. Cattani-Scholz, B. Rieger, M. Tornow, *Nanotechnology* **2019**, *30*, 395201.
[239] H. Yamada, N. Saitoh, B. Ghosh, Y. Masuda, N. Yoshizawa, N. Shirahata, *J. Phys. Chem. C* **2020**, *124*, 23333.
[240] B. Ghosh, Y. Masuda, Y. Wakayama, Y. Imanaka, J. Inoue, K. Hashi, K. Deguchi, H. Yamada, Y. Sakka, S. Ohki et al., *Adv. Funct. Mater.* **2014**, n/a-n/a.
[241] B. Ghosh, T. Hamaoka, Y. Nemoto, M. Takeguchi, N. Shirahata, *J. Phys. Chem. C* **2018**, *122*, 6422.

[242] M. L. Mastronardi, E. J. Henderson, D. P. Puzzo, Y. Chang, Z. B. Wang, M. G. Helander, J. Jeong, N. P. Kherani, Z. Lu, G. A. Ozin, *Small* **2012**, *8*, 3647.
[243] G. Krikun, K. Zojer, *J. Appl. Phys.* **2019**, *125*, 85501.
[244] J. Chen, Z. Wang, Z. Chen, S. Cong, Z. Zhao, *Nano Lett.* **2020**, *20*, 1915.
[245] E. Ihara, V. G. Young, R. F. Jordan, *J Am Chem Soc* **1998**, *120*, 8277.
[246] C. Marschner, *Eur. J. Inorg. Chem.* **1998**, *1998*, 221.
[247] P. V. Avramov, D. G. Fedorov, P. B. Sorokin, L. A. Chernozatonskii, M. S. Gordon, *J. Phys. Chem. C* **2007**, *111*, 18824.